Development of verified FE simulation method on crimp joint with gasket

A combined experimental and numerical study

Erik Andraéy

Faculty of Mechanical Engineering, Blekinge Institute of Technology, 371 79 Karlskrona, Sweden

This thesis is submitted to the Faculty of Mechanical Engineering at Blekinge Institute of Technology in partial fulfilment of the requirements for the degree of Master of Science in Mechanical Engineering. The thesis is equivalent to 20 weeks of full time studies.

The authors declare that they are the sole authors of this thesis and that they have not used any sources other than those listed in the bibliography and identified as references. They further declare that they have not submitted this thesis at any other institution to obtain a degree.

Contact Information:
Author(s):
Erik Andraéy
E-mail: eraa16@student.bth.se

University advisor:
Mats Sigvant
Department of Mechanical Engineering

Faculty of Mechanical Engineering	Internet : www.bth.se
Blekinge Institute of Technology	Phone : +46 455 38 50 00
SE-371 79 Karlskrona, Sweden	Fax : +46 455 38 50 57

ABSTRACT

When developing drivetrain cooling modules for commercial vehicles, the top priority is the strength of the products. The reason lays within the structural change that companies are undergoing where the warehouses are minimized and the companies are relying on the transportation of commercial vehicles. If a drivetrain cooling module would fail to maintain a targeted temperature range of the drivetrain, there is not long until the vehicle is forced to a stop. At worst, the downtime of commercial vehicles can cause companies to come to a halt as well. Therefore, developing verified FE simulation methods together with strength verification tests, are some of the core activities to ensure the strength of the cooling modules before implementation in vehicles.

One of the methods that have not been sufficiently verified regards how to perform structural FEA on a crimp joint with a gasket. A crimp joint is established through a hemming process, where the aluminium header tabs are crimped over the polyamide tank, creating a watertight seal together with a gasket. The objective of this master's thesis is to verify the existing simulation methods of the crimp joint and determine the margin of error with respect to strains. The objective of this thesis is also to develop a verified FE simulation method with a lower margin of error compared to the existing methods. The verification of the methods has been conducted through a comparison between numerical results and an experimental stress analysis, where the strain located on the header is measured with strain gauges in a pressure pulsation rig.

The average margin of error found on the three existing methods of simulating the crimp joint was 39,7%, 13,4%, and 11,5% located on the outer bottom dimensioning radius of the crimp joint at a pressure of 100 kPa. However, the method used to determine the margin of error was found to be invalid, but the margin of error is only slightly affected by the verification method where the existing methods still are insufficiently representing the crimp joint. The method of determining the margin of error was then corrected for the development of the new method to represent the crimp joint in the FE model. The developed method in this thesis has an average margin of error of 6,9% at 100, 160, 220, and 260 kPa.

Keywords: Method development, Radiator, Experimental Stress Analysis, Structural Analysis

SAMMANFATTNING

Vid utveckling av kylarmoduler för drivlinor som appliceras i kommersiella fordon, är högsta prioritet att säkerhetsställa hållfastheten hos produkterna. Anledningen ligger kring den strukturomvandling som företag genomgår där storleken på lagerlokaler minskar och företagen väljer att förlita sig på transporterna som utförs av kommersiella fordon istället. Ifall en kylarmodul inte skulle klara av att bibehålla ett bestämt temperaturintervall hos drivlinan så dröjer det inte länge förens fordonet tvingas att stanna. I värsta fall kan fordonets stillestånd påverka ett företag att tvingas stanna i väntan. Därför är utveckling av FE simuleringsmetoder tillsammans med utmattningstest, några av de kärnaktiviteter som utförs för att säkerhetsställa hållfastheten av kylarmodulerna innan de implementeras i fordon.

En av de metoder som ännu inte blivit tillräckligt verifierat gäller hur man utför FEA på ett falsförband med packning. Falsförbandet skapas genom en falsningsprocess där ändplåten av aluminium falsas över polyamidtanken, vilket skapar ett vattentätt förband med hjälp av packningen. Omfattningen av detta examensarbete gäller att verifiera de existerande simuleringsmetoderna av falsförbandet och bestämma felmarginalen med avseende på töjningar. Omfattningen av examensarbetet innefattar även ett utvecklingsarbete av en ny FE simuleringsmetod med en lägre felmarginal jämfört med de existerande metoderna. Verifieringen av metoderna sker genom en jämförelse mellan de numeriska resultaten och en experimentell spänningsanalys där töjningen på ändplåten är uppmätt med hjälp av trådtöjningsgivare i en tryckpulsationsrigg.

Den genomsnittliga felmarginalen av de tre existerande metoderna för att simulera falsförbandet var 37,9%, 13,4%, och 11,5% vid den nedre dimensionerande yttre radien på falsförbandet vid ett tryck på 100 kPa. Den använda metoden för att bestämma felmarginalen upptäcktes senare vara felaktig, men det resulterar endast i små förändringar av den bestämda felmarginalen, de existerande simuleringsmetoderna är fortfarande sedda som otillräckliga. Metoden för att bestämma felmarginalen korrigerades sedan inför utvecklandet av den nya FE simuleringsmetoden av falsförbandet. Den utvecklade metoden i detta examensarbete har en genomsnittlig felmarginal på 6,9% vid 100, 160, 220 och 260 kPa.

Nyckelord: Falsförband, Metodutveckling, Radiator, Experimentell Spänningsanalys, Strukturanalys

ACKNOWLEDGEMENT

NOMENCLATURE

FE	Finite Element
FEA	Finite Element Analysis
EPDM	Ethylene Propylene Diene Monomer
E	Young's Modulus
ε	Strain
σ	Stress
L	Length
V	Voltage
k	Gauge Factor
$p\text{-}p$	Peak to peak
P	Pressure
δ	Displacement
DAM	Dry As Moulded
DOF	Degrees Of Freedom

CONTENTS

LIST OF FIGURES

LIST OF TABLES

1   INTRODUCTION

With the development of philosophies such as lean production, light has been shed on the many wasteful activities of businesses. Sitting on large warehouses is one of these activities, where the cost of running a warehouse can be minimized greatly. The only problem is that the costs are minimized by eliminating the storing space to the furthest extinct possible, leading to businesses relying on logistics. The transportations to, and from the business are then crucial to be on point as if there would be any delays, the business comes to a halt. The robustness of the transportation vehicles is therefore of great interest to keep the businesses running. As robustness is key when it comes to designing and developing the next generation transport vehicles, developing verified methods that can ensure the strength of the components is one of the core activities to ensure robustness.

1.1   Background

One of the systems that can bring transportation vehicles to a halt is the powertrain cooling system. If the cooling system would fail to cool down the powertrain sufficiently, there is not long until the vehicle is forced to stop. The powertrain cooling is a system built out of several different heat exchangers connected to the powertrain. One of these heat exchangers is the radiator, a product that cools down the coolant running through some of the drivetrain systems such as the engine to maintain the temperature within a targeted range. The radiator itself is built out of several components consisting of mostly aluminium, steel and polyamide. Most of the connections of the radiator are bolted or brazed, however, one of these connections are established by mechanical crimping. The connection between the fibreglass-reinforced polyamide tank and the aluminium header is the connection at hand, referred to as a crimp joint. As the joint is supposed to keep a pressurized coolant inside the components, there is an EPDM gasket in the connection to prevent the liquid from leaking. The crimp joint is a connection that several manufacturers use on their drivetrain cooling products, making it a well-used connection method. Unfortunately, there is no existent research contribution regarding how to conduct structural FEA on the crimp joint with gasket, leading to businesses developing their products relying on internal investigations only.

One of the businesses that use the crimp joint on its radiators is the corporate partner, TitanX. The methods they use to conduct structural FEA on the crimp joint is simplified and have not been sufficiently verified. This master's thesis has been part of the project to verify the existing simulation methods and develop a new verified simulation method with a targeted linear elastic model to conduct structural FEA on the crimp joint to continue the mission of ensuring the strength of the powertrain cooling modules.

1.1.1   Studies from corporate partner

During the development of one specific radiator, the corporate partner has carried out pressure pulsation tests to ensure the strength and determine the area of failure. The pressure pulsation test was conducted on three individual radiators, exposed to the same loading conditions in a rig with internally pressurized water. The results show that two of the radiators failed due to a crack in the bottom radius of the header, close to the outlet connection pipe of the radiator on the engine side. Whereas the third failed in the same area on the header, but on the grill side instead. The crack growth starts on the inside of the radius where the joint is subjected to tensile stress, which eventually leads to fatigue failure. The areas mentioned are thoroughly explained in chapter 1.1.2.

During the development of the radiator, a FE model was developed. This model will be used throughout the thesis for the verification of the existing simulation methods and during the development of the new FE simulation method. The developed FE model for the radiator shows that the maximum stress of the radiator is located in the inner bottom radius of the header, close to the outlet pipe of the radiator on the engine side, which is the same area as two of the radiators failed in the pressure pulsation rig. The minimum principal stress is located in the same area, but on the outer bottom radius instead, and is a result of the tensile stress on the inside of the radius. As the results from the FEA and pressure pulsation test are close to identical, it can be expected that the existing FE model is trustworthy. Therefore, the vector principal stresses can be studied in this area to lay the foundation for the controlled experiment. In Figure 1-1, the stress vectors can be seen where the blue vectors show the principal

direction of the minimum principal stress, and the red shows the principal direction of the maximum principal stress. Due to the maximum principal stresses being close to non-existent in comparison to the minimum principal stresses, the stress state is simplified to being uniaxial during the numerical and experimental stress analysis. The principal direction will therefore also be used during the instrumentation of the header in order to attach the strain gauges to measure the minimum principal strains.
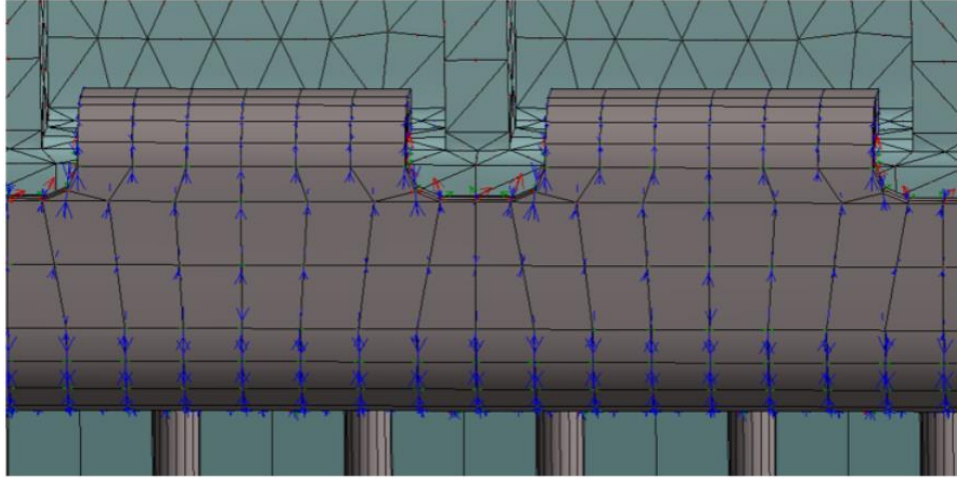
Figure 1-1: Vector principal stress on the header.

1.1.2   The anatomy of a radiator

The core of a radiator is the heat exchanger which is the part where the temperature exchange is taking place. The core is an assembly consisting of the components header, fin, tubes, and side plates, all of which are made out of aluminium and brazed together. Numerous tubes and fins are running parallel to each other and the headers are connected in the ends where the opening of the tubes are. In Figure 1-2 and Figure 1-3 the components are described, where the geometry of the fins is replaced by a simplification, called homogenisation, that has been developed by the corporate partner. The simplification consists of replacing actual, very complex, fin geometry by using block-shaped elements having orthotropic material properties that preserves the correct stiffness of the actual fin geometry. However, the simplification does not affect the displacements and stresses in the crimp joint, and for a better description of the fins see chapter 3.1.2. Attached to the core are also the components side member, tank, and gasket. The aluminium side plate is positioned under the steel side member, and both components are connected to both sides of the radiator running parallel with the tubes and fins. The fibreglass-reinforced polyamide tanks are then attached to the headers through a hemming process, where the header tabs are crimped over the tank, creating a waterproof seal with the help of an EPDM gasket positioned in between the headers and tanks.
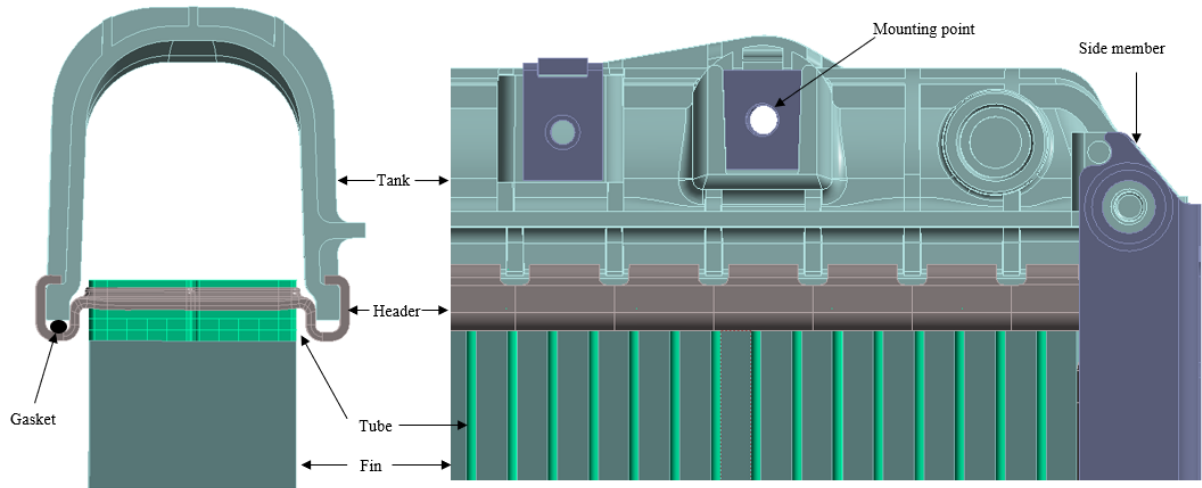
Figure 1-2: Component description.
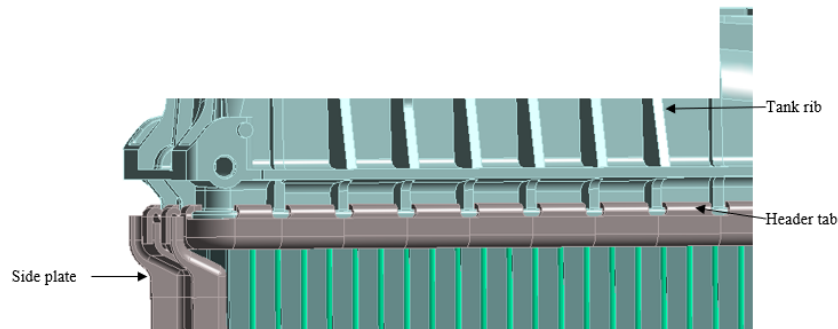
Figure 1-3: Component and part description, radiator viewed from the engine side.

In Figure 1-3 and Figure 1-4 are some of the parts of the components described, these will be used throughout the paper.
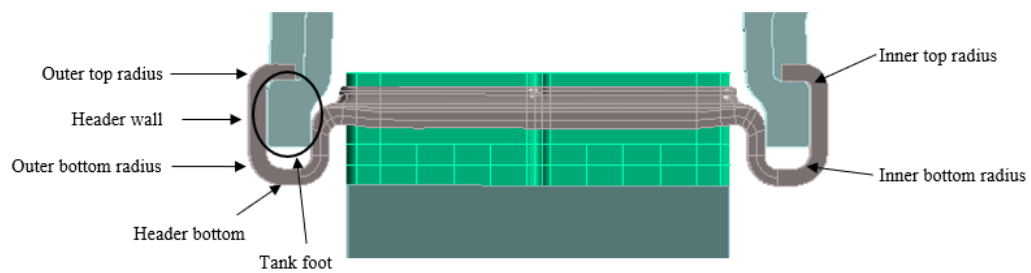
Figure 1-4: Part description of crimp joint.

1.2 Aim and scope

This master's thesis aims to verify how well the existing FE simulation methods on a crimp joint represents actual behaviour and how the method can be further developed. A method that better represents reality would facilitate product optimization, e.g decrease development time and ensure the strength of the product to avoid quality-related issues. Premature failure in validation testing can cause delays in projects, and quality issues on delivered products can cause delays for the logistic transports that other companies are relying on. The damage to the radiator can also cause leakage of toxic fluids.

The developed method intends to replace the existing ones and increase the precision of the FEA to help plant engineers with their simulations of the radiators.

This thesis will include a controlled experiment where an experimental stress analysis is conducted on a radiator subjected to internal pressure in a pressure pulsation rig. The radiator will be instrumented with strain gauges, thermocouples, and dial indicators to measure the data that the FE simulation methods will be verified against. A combined experimental and numerical investigation will be conducted to confirm the stiffness properties of the anisotropic PA66GF30 tank. Lastly, the verification of the existing simulation methods is conducted together with the development of the new linear elastic FE simulation method, which is conducted through a case study.

1.3   Thesis questions
- What margin of error does the current FE simulation methods have on the crimp joint with respect to strain?
- How can the FE simulation method be optimized according to the margin of error with respect to strain while still maintaining a linear-elastic FE model?

1.4   Limitations of thesis
- The experimental stress analysis is conducted in a dry environment, where air is used as media instead of coolant water.
- ANSYS Mechanical is the only software used to perform FEA.
- A linear elastic model is assumed.

1.5   Outline
The first chapter of the paper introduces the objective and aim of the thesis together with the background information and theory related to the presented problem.

The second chapter presents related research contribution on radiators, the complications of mounting strain gauges on the fibreglass-reinforced polymers, as well as studies of the anisotropic and hygroscopic material properties of fibreglass-reinforced polymers.

The investigations and studies of the thesis are presented in the three chapters Method, Results and Analysis, and Discussion. Each of the chapters are divided into four parts containing the controlled experiment, elasticity of PA66GF30, verification of existing simulation methods, and the development of the new simulation method.

In the final chapter, the conclusions together with the future work are presented.

1.6   Theory

1.6.1   Strain gauge
Strain (ε) is a dimensionless quantity that describes the deformation of a material caused by external or internal forces. Depending on what type of force the body is subjected to, it can experience different kinds of strain. If the body is subjected to an external load, such as a force, moment, or pressure, it is experiencing a mechanical strain. If the body is subjected to various temperatures, heat and cold can cause the body to elongate or contract, resulting in a thermal strain. The body can also experience strain from internal forces, often caused by plastic deformation and non-uniform temperature changes in different sections of the body. These are called residual strains and are often caused by manufacturing operations such as hemming, welding, forging, and heat treatment. The strain is measured according to:

$$\varepsilon = \frac{\Delta L}{L} \tag{1}$$

where L is the initial length of the body. The strain is also directly proportional to stress in the case of uniaxial stress states according to Hooke's Law:

$$\sigma = \varepsilon E \tag{2}$$

where E is the Young's modulus [1], [2].

When conducting an experimental stress analysis to determine the stress state on a material, the strain is measured using strain gauges. If a principal stress is sought, the strain gauges are mounted according to the principal direction of the stresses as the gauges only can measure in one direction. If the principal direction is unknown for the loading case, then 3-grid rosette strain gauges can be applied. If the principal direction is known, a single-grid gauge can be applied for uniaxial cases and 2-grid rosettes for biaxial cases. Conducting experimental stress analyses on triaxial stress states entails problems for strain measurements as they need to measure the strain in the depth direction of the material. There are methods to incorporate strain gauges during casting, but if the body is exposed to an external force, the maximum stresses are always at the surface [2], [3].

The strain gauges measure strain by using the resistive foil as an electrical conductor. If the strain gauge is exposed to compressive stress in its measuring direction, it will cause the cross-sectional area of the resistive foil to increase, which lowers the resistance. If the strain gauge is exposed to elongation, the cross-sectional area will decrease, which will, in the same way, increase the resistance of the strain gauge [4].

To be able to measure the varying resistance, a Wheatstone bridge is used. A Wheatstone bridge is compiled of four resistors according to Figure 1-5. The Wheatstone bridge has an applied source of voltage V_S, and the output voltage V_O is measured simultaneously. The output voltage can be calculated according to:

$$V_0 = V_S \left(\frac{R_1}{R_1 + R_2} - \frac{R_4}{R_3 + R_4} \right)$$
(3)

and if the bridge is balanced out i.e.

$$R_1 = R_2 = R_3 = R_4, \text{ and } \frac{R_1}{R_2} = \frac{R_4}{R_3}$$
(4), (5)

then the output voltage $V_0 = 0$. If one of the resistors is substituted for a strain gauge, the resistance on the gauge will differ from its initial value when the strain gauge is exposed to a loading condition, resulting in an output voltage $V_0 \neq 0$. There are several variations of Wheatstone bridges involving everything from one strain gauge (quarter bridge) up to four strain gauges (full bridge). If a quarter bridge is used, the strain can be calculated according to:

$$\varepsilon = \frac{4V_0}{kV_s}$$
(6)

where k is the gauge factor [5].
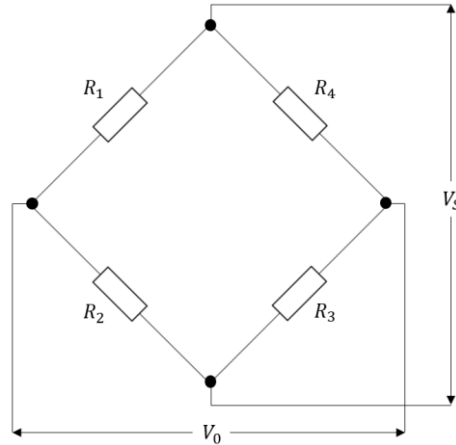
Figure 1-5: Wheatstone bridge.

1.6.2   Load cell

Load cells are used to measure force and acts as a transducer. Load cells commonly use strain gauges in a full Wheatstone bridge configuration to measure the applied load and outputs an electrical signal from which the force can be determined. There are both tensile and compressive load cells depending on the loading case, and if a compressive load cell is used, it is usually located beneath the specimen. The materials used for constructing a compressive load cell are usually resistant to scratches and corrosion, and the plate in the load cell should also be free from any deformations to be able to conduct precise measurements. Therefore, the plate has often a treated surface to cope with the requirements [6].

1.6.3 Thermocouple

A thermocouple is a sensor for measuring temperatures. The sensor is composed of two wires made from different metals which are joined in the end where it is measuring the temperature. When both metal wires are exposed to heat, they will be heated at an uneven pace. Then, when there is a difference in heat between the ends of the wires, a small voltage potential is created between the two free ends. This effect is called the Seebeck Voltage and can be used to backtrack the temperature at the connection of the two wires. There is a wide range of metal wires that can be combined for specific temperature cases ranging from the absolute zero up over 2000°C [7].

1.6.4 Pressure pulsation

Pressure pulsation is a commonly used test method to determine the fatigue life of products operating under various loading conditions. When a specimen is exposed to a varying load, it can eventually cause the material to fail due to fatigue failure, often because of cracks in the specimen. With a test rig can different environments be represented where the specimens can be exposed to varying pressure, temperature, and different types of media. The test can determine products endurance and the area of failure can be reinforced if needed. The test results can also be used to minimize the amount of material needed for products, leading to lower costs and less use of natural resources [8].

1.6.5 Hygroscopy

Some materials have the ability to attract and hold water molecules, these materials are called hygroscopic. One hygroscopic material is polyamide which attracts water molecules due to its polar molecular structure. When the water is attracted, the hydrogen atoms in the water molecule starts to bond to oxygen atoms in the polyamide polymer chain. Simultaneously is the oxygen atom in the water bonding to a hydrogen molecule in the polyamide polymer chain. When the water molecule has bonded to the polyamide polymer chain, it will cause the polymer chains to separate from each other due to the water located in between the chains. This separation will cause a change in the polyamide's material properties. As the bond between the polymer chains has loosened, the materials strength and stiffness decreases, but the impact strength and fracture toughness increases. How much the material properties change all depends on the amount of water bonded to the polymer chains, which depends on the time the material has been subjected to the conditioned environment [9].

1.6.6 Finite element analysis

FEA is a computerized simulation tool using the numerical finite element method to calculate how a body reacts to structural forces, fluid dynamics, vibration, and other natural and physical phenomena. The method consists of splitting the body into a finite number of elements that together constitute the structure of the body. The elements themselves can be constructed as different geometries, each with individual advantages and disadvantages. The calculations are then performed on the nodes of each individual element, where the results of the nodes are interpolated and extrapolated over the element. The combined result of all elements forms the behaviour of the body. The nodes are points that are usually located at the corners and borders of the elements, and the number of nodes is thus affected by the geometry of the element. The more nodes the body consists of, the more calculations are conducted on the body, increasing the precision of the method. To increase the accuracy of the element, different orders of the element can be set to increase the accuracy of the interpolation over the element. If the element has a cubic shape (hexahedral) and is defined as linear (first-order), the cubic element will consist of one node in each corner, counting to 8 nodes in total. If the cubic element would be defined as parabolic (second-order), an extra node is inserted between each of the corners, counting up to 22 nodes in total. The increased number of nodes also allows the cubic shape of the element to deform differently compared to the first-order element, improving the elements ability to approximate the geometry of the body [10].

ANSYS Mechanical is a software with a range of FEA solvers for different applications with structural, thermal, acoustics, and nonlinear capabilities [11]. One of these solvers is the static structural

solver, which is commonly used for solving structural scenarios of a body subjected to external forces where parameters such as strains, displacement, and stress are sought. The static solver means that the software only supports simulations, where there is a static body, for cases with a dynamic body, other dynamic solvers are used. The static structural solver can use both an implicit and explicit finite element method depending on the type of simulation and load case. The implicit method is a direct solver that simulates the body subjected to an external force at a given time, whereas the explicit method is an iterative solver that simulates the body subjected to the external force in several time steps. Therefore, the explicit method is often referred to as a time-dependant method which is used during nonlinear simulations and when there is a non-static load case [12].

2 RELATED WORK

According to a probabilistic FEA conducted by Rob Roy et al. the maximum von Mises stress found on a heavy-duty radiator is located in the header tube joint [13]. Depending on the model of the radiator, the location of the maximum stresses can differ, but they are often located in, or in contact with the header. The model used by Roy et al. is constructed by components of the same material as is used in the radiator in this project, but the design differs. Although the model used by Roy et al. do not have a crimp joint connecting the header and tank, their work strengthens the problem presented as the maximum stress is located at the area around the header. Whether or not the maximum stresses are in the crimp joint, all stresses of the header will be affected by how the crimp joint acts under load. By determining how the crimp joint acts, the entailed risk of using the unverified method to simulate the crimp joint can be eliminated.

In an investigation conducted by Mao et al. a combination of Computational Fluid Dynamic (CFD) and FEA simulations were used for a thermal and structural study of a heavy-duty radiator [14]. The investigation was conducted to predict the deformations, stress, and strains caused by the heat exchange taking place in the tubes of the radiator. The result shows that the maximum thermal stress is located in the tube close to the joint between the header and tube. In the study is the uneven temperature from the analysis plotted. The uneven temperature will cause the radiator to have an uneven elongation, which causes the thermal strains. The water mass flow rate of each tube is also plotted, showing how the coolant is transported through the tubes unevenly, which causes an uneven temperature and internal pressure of the radiator tubes. The radiator studied have some differences in its design, but the effects from the heat exchange and the studied uneven temperature distribution will affect this thesis similarly.

Schouwenaars et al. analysed the occurrence of cracks in the radiator tank that was discovered during pressure testing [15]. The crack was discovered to originate from the assembling when the tank is attached to the header through the mechanical crimping process. Their analysis was conducted to create a tangible method for plant engineers to take part of when facing design or process problems related to the fibreglass-reinforced polyamide tank. The motivation for the study is similar to this thesis, where the result of the study is supposed to help plant engineers in the drivetrain cooling industry to create methods that can support the development of new products. The material of the analysed plastic tank differ from the tank analysed in this thesis, but fibreglass-reinforced polymers in general, are expected to have similar behaviour. These studies combined gives a better understanding of how the radiator's components can be analysed.

In a study conducted by Zike and Mikkelsen [16], the correction of gauge factor is investigated for polymer-based composite materials. The results from the study prove that many factors can cause the gauge factor to differ from the factor provided by the strain gauge manufacturer. To support their results, the strain gauge manufacturer HBM describes the problems of conducting strain gauge measurements on fibre-reinforced plastics [17]. The problems explained are connected to the geometries of both strain gauges and the specimen, heat conductivity of fibre-reinforced plastics, installation, and orientation of fibre reinforcement. Because of the severity of installing and analysing the measured strains on polymer-based composites, performing strain gauge measurements on the fibreglass-reinforced polyamide tank have been neglected, instead, the experimental stress analysis will only analyse the strains of the aluminium header.

In a study conducted by De Monte et al. [18], the influence of temperature and thickness on 35% fibreglass-reinforced polyamide 66 is investigated. The material studied is similar to the material of the radiator tank in this thesis. In the study, the Young's modulus was found to be dependent on the thickness of the specimen. When the thickness of the specimen increased from 1 mm to 3 mm at room temperature, the Young's modulus was found to decrease by 5%. The Young's modulus was also found to be dependent on the fibre orientation of the reinforcement. It was found to have a decrease of 15-20% when the specimen was tested 45-90° to the fibre direction compared to the measuring parallel. The Young's modulus for the radiator tank in this thesis is unknown, and the current modulus used in the existing FE model is considering the influence of hygroscopy. This study was used during the initiation of the verification of the existing simulation methods to adjust the Young's modulus provided by the material supplier. However, as the material is anisotropic, the Young's modulus could not be sufficiently determined in detail for the whole tank with the study, but the study gave reasons to believe that the stiffness properties of the tank were worth investigating further.

As can be seen from the related work, there is no verified research contribution regarding how to perform structural FEA on a crimp joint, nor on a crimp joint with a gasket. There exists contribution regarding structural analyses on the radiator, all of which together with this thesis, will increase the understanding of the loading case in the radiators and help the plant engineers develop the next generation radiators.

3 METHOD

In this thesis, two research methodologies are used. Controlled experiments are used to extract data, and case studies are used during the development of the new FE simulation method. The effectiveness of the controlled experiment lays within how well a relationship between a dependant variable and an independent variable can be determined. If there are two independent variables that both cause a change of the dependant variable, a set of conditions must be sought to find the causality of the two independent variables. In a complex system, such as a powertrain cooling system, a numerous number of independent variables emerge that have a relationship to the dependant variable, making it problematic to determine a relationship with each independent variable. Here is where the control of the experiment is the key to find the relationship. By controlling all variables in a system, the sought relationship can be isolated and tested independently to all other variables. The setup of the experiment is therefore dedicated to minimizing the amount of influence other independent variables can have on the variables of the sought relationship.

When determining the stress in a material, there are only two generally accepted and commercially available methods, numerical and experimental stress analysis. As the numerical method entails an uncertainty of simplifying the environment of a body, experimental stress analysis is generally used to verify the numerical method, leading to no other choices than a controlled experiment to extract data. Even though several variables can be controlled during the experiment, some parameters that have a relation to the measured strain and displacements are not known. Some of these are the gaskets influence on the system, the material properties of the polyamide tank, and the residual strain from manufacturing.

When the results from the experiments are extracted, the numerical method can be developed through a case study. How well the experimental and numerical results align are therefore the result of how well the sought relationships between the variables have been determined.

3.1 Controlled experiment

As the radiator has undergone tests in the pressure pulsation rig where the area of failure was located on the outlet side of the radiator, the outlet side became the focus of the controlled experiment. The stress and displacements in, and around the crimp joint are the dependant variables of interest that are to be determined through the controlled experiment. Stress is a variable that cannot be measured directly through an experiment, instead, the strain is measured which is directly proportional to the stress in the case of linear elastic materials. Strain gauges are a conventional instrument to be used for measuring strain in materials, and strain gauges are also an instrument that the corporate partner has experience of using. In combination with strain gauges will also thermocouples be used to determine the temperature of the material that the strain gauges are subjected to. Depending on the temperature of the header where the gauges will be attached, the foil in the gauges will elongate, leading to incorrect strain readings. If the temperature is known, the effect of the temperature on the strain measurements can be analysed and corrected for if desired. However, the strain gauges can only measure strain and give no exact description of how the system moves and displaces. Dial indicators will therefore also be used to complement the strain gauges to give a better understanding.

3.1.1 Positioning of sensors

The maximum stress in the existing FEA is located along the crack on the header from the pressure pulsation fatigue testing, meaning that the existing method already is a generally good description when it comes to the position of the maximum stresses of the system. The problem is that the maximum strain in the inside radius, that is causing the crack growth, cannot be measured with strain gauges as it is not accessible. The only parts of the headers that are accessible to use strain gauges on are the outside radii and the walls where the minimum principal stresses are located. The minimum principal stresses are proportional to the maximum principal stresses as they both are a result of the internal pressure located in the same area. The outside surfaces of the tanks are also accessible to measure strain on, but because of the complexity of measuring strain on fibreglass-reinforced polymers [16], [17], and because the measuring system of the corporate partner does not support the recommended 1000 Ω strain gauges [17], measuring strain on the tanks is neglected. The strain gauges are instead placed on the header in two different cross-sections of the crimp joint. The first section regards the middle part of the header

and tank. The middle section was chosen as it is the least affected section from the outlet connection pipe, side plate, and side member, the section is also rather uniform, only the top of the tank is slightly inclined. This section will be used to start developing the method that represents the crimp joint in FEA, as in this position the crimp joint is least affected by geometries and other components that complicates that matter. The other section is the area around the outlet connection pipe of the radiator. This section has the highest stresses in the radiator but is also influenced by the inlet port, adding other factors to the analysis. Both sections can be seen in Figure 3-1.
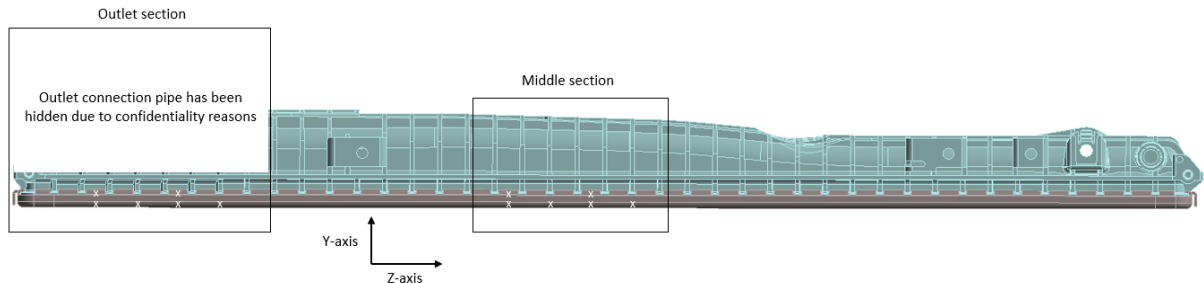
Figure 3-1: Placement of strain gauges and definition of outlet and middle section.

The strain gauges are placed six on each side of each section, counting to 24 strain gauges in total. One of the mounted strain gauges is a 5-grid strain gauge, consisting of five individual strain gauges connected at an equal length to analyse the whole radius of the crimp joint. All strain gauges attached measures uniaxial strain as described in chapter 1.1.1. The grid length of all strain gauges is mounted in parallel with the minimum principal stress vectors, which also is perpendicular to the geometry of the crack. The strain gauges are placed on the outer top and bottom radius of the header as can be seen in Figure 3-2. The strain gauges on the outer bottom radius of the header are placed underneath and in between the tabs of the header. There are two strain gauges mounted at the outer top radius and four at the outer bottom radius of each side of each section, so that any doubtful results can be neglected due to the double measurements. A summary of the instrumentation can be seen in Appendix A. At each group of strain gauges is also a thermocouple attached to the header wall, so the measurements of the strain gauges can be analysed with the temperature known. There are also thermocouples attached to the tank and tank ribs to see if there is a temperature difference. If there is a temperature difference where the heat has not spread to the tank ribs, the tank ribs will be stiffer than the rest of the tank, thus it may have to be considered when evaluating the strains.
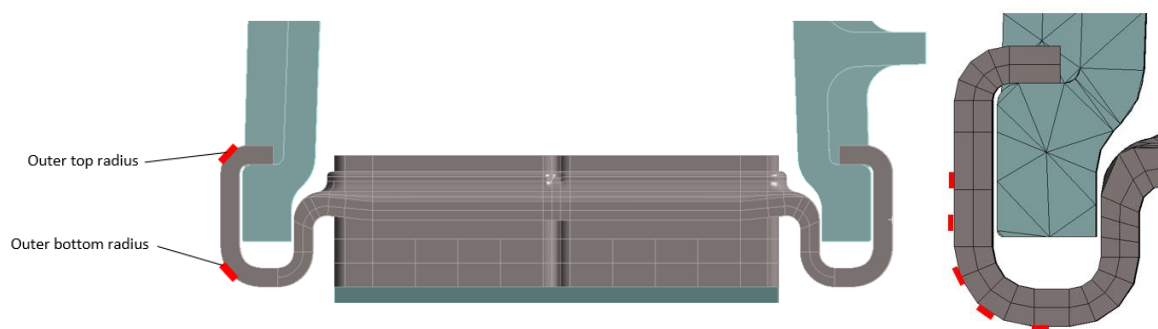
Figure 3-2: Placement of 1-grid (left) and 5-grid (right) strain gauges.

3.1.2   Instrumenting the radiator
To be able to apply the strain gauges to the radiator's header, the surface of the header needs firstly to be prepared. The surface is covered with remains of non-corrosive flux from the manufacturing process which results in a coarse surface. For the strain gauges to be able to correctly analyse the strains, the surface needs to be smooth, irregularities can affect the bonding contact negatively and cause the strain gauges to stretch unevenly depending on the contact it has with the surface. The first step in preparing the header is therefore to firstly wet sand off the flux remains with 220-grit sandpaper together with an

etchant liquid. The surface is then wet sanded with 500-grit sandpaper together with a cleaning/ neutralizing liquid used to prepare the surface and neutralize chemical reactions to create a surface free from contaminants. The surface is then thoroughly cleaned by wiping off the remains with the cleaning/ neutralizing liquid. Then a piece of glass is cleaned using a cleaning spray for electric applications so that the strain gauges are not contaminated as they are placed on the glass. The strain gauges are then covered with an electric insulation tape by attaching the tape edge to edge with the strain gauge according to Figure 3-3. As the strain gauges only are 1 mm long, applying the tape is done using tweezers.

The placement of the gauges is then measured out and marked with tape so that the edge of the gauges can be placed edge to edge with the newly attached tape. Before the strain gauges are applied to the newly cleaned header, the surfaces are cleaned with the cleaning spray, so that any contaminants that might have got stuck on the surface are removed before the gauges are placed in their positions. The strain gauges are then applied to the surface using tweezers, but the gauges are not pressed down against the surface, only the part of the tape that is not covering the gauge is. The part of the tape attached to the header is then covered with two pieces of tape, to prevent it from moving. This leaves the strain gauges to rest in the air according to Figure 3-3. The area under the gauge is then covered with cold curing adhesive for strain gauge application. The strain gauges are then pressed down against the surface using a pressure pad to evenly distribute the pressure to not damage the strain gauge. To prevent the pressure pad from getting stuck to the glue by mistake, a piece of Teflon plastic is used in between the pressure pad and the tape covering the strain gauge. The strain gauge is then pressed against the surface for 3−4 minutes so that the glue starts to cure before the pressure is relieved. The glue is then set to fully cure before the Teflon plastic and tape is removed from the gauges using tweezers. During instrumentation, the adhesive expired, resulting in some of the gauges letting go from the contact with the header. These strain gauges had to be removed and the full process had to be iterated. The strain gauges were replaced by new ones using another type of cold curing adhesive for strain gauge application.
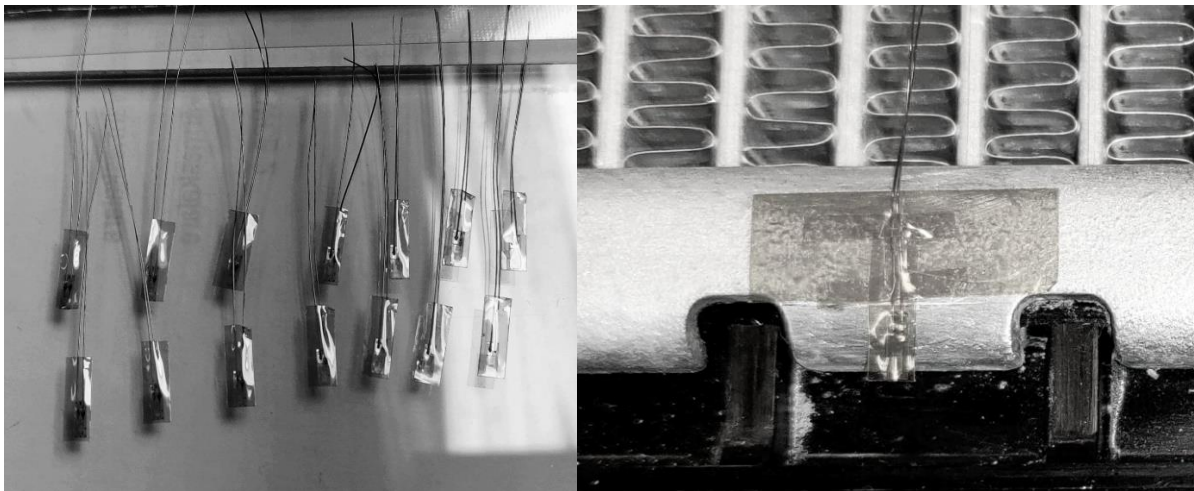
Figure 3-3: Strain gauges with tape applied (left) and strain gauge resting in the air before the adhesive is applied (right).

Next to each strain gauge is a soldering terminal attached using the adhesive on the backside of the terminal. The strain gauges' wires are then cut to length, and the alloy on the wires is grinded off using a fibreglass pen without pulling in the strain gauges. The wires are then soldered to the terminal as in Figure 3-4. The next step is to solder a 3-core cable to the terminal by soldering two of the ends to the same soldering plate. When the cables are soldered into place, the resistance over the terminal can be measured and noted. On the other end of the cables are then a modular plug attached. The resistance at the plug is then measured and noted again. The resistance is measured to see if any strain gauges are defective or if there have been other errors during the instrumentation. The exact placement of the strain gauges and the measured resistance can be viewed in Appendix A.
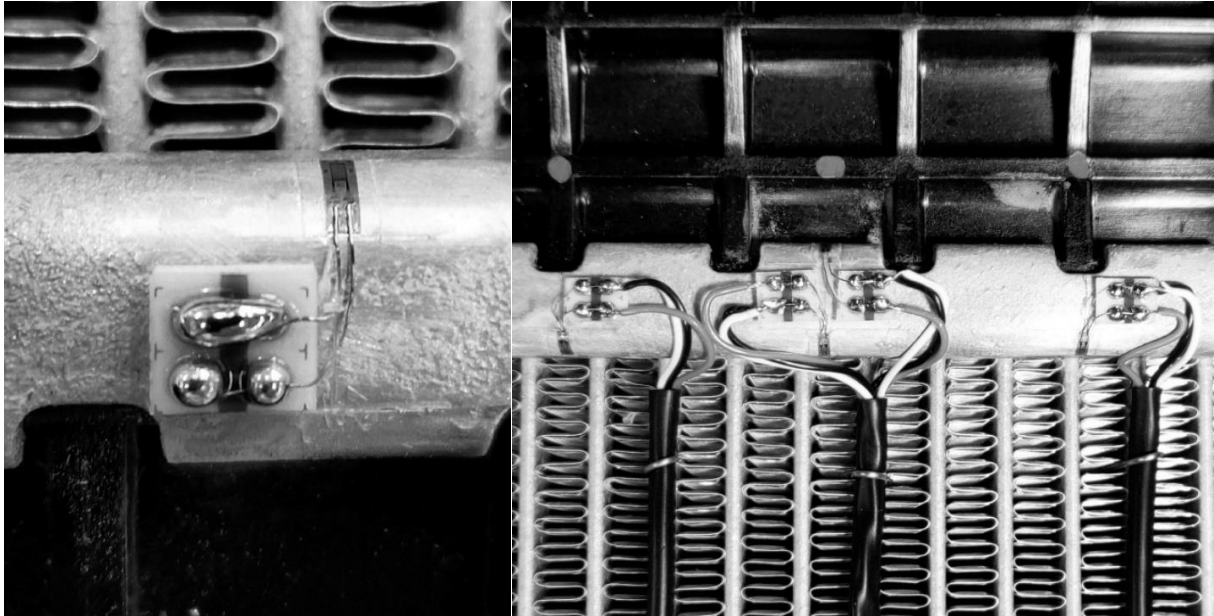
Figure 3-4: Strain gauge soldered to a terminal (left) and strain gauges together with cables attached to terminals (right).

To protect the strain gauges and the terminals, a protective nitrile rubber covering material is applied carefully over the instruments. After the strain gauges have been attached, the areas where the thermocouples shall be attached are prepared. The areas on the polyamide tank are grinded with a fine file, as the surface is too smooth for the adhesive to bond. The areas on the tank are then cleaned with electronic cleaning spray together with the areas on the header that do not need any filing. The thermocouples are then mounted to the radiator so that the ends are resting against the surface, if the thermocouple does not rest against the surface, the temperature will not spread to it. The thermocouples are then covered with a two-component adhesive, the adhesive used for the thermocouples differs from the strain gauges as the thermocouples can be reused. Therefore, it is desirable to be able to remove the thermocouples without damaging or having remains of the adhesive covering them. When the two-component adhesive, together with the rubber covering material has cured, all attached instruments can be covered with another protective covering material out of silicone. The silicone is first set to start curing for 1-2h, the radiator is then turned upside down so the silicone will run down and stay over the instruments. This creates a thicker layer of silicone that else would spread out more over the header, the radiator is then left in this position until the silicone has fully cured. It is recommended by the manufacturers to use several layers of protective covering material to increase the protection of the strain gauges. The protective silicone, together with all other products used for the instrumentation can be seen in Table 3-1. Some of the fully instrumented strain gauges and thermocouples can be seen in Figure 3-5.
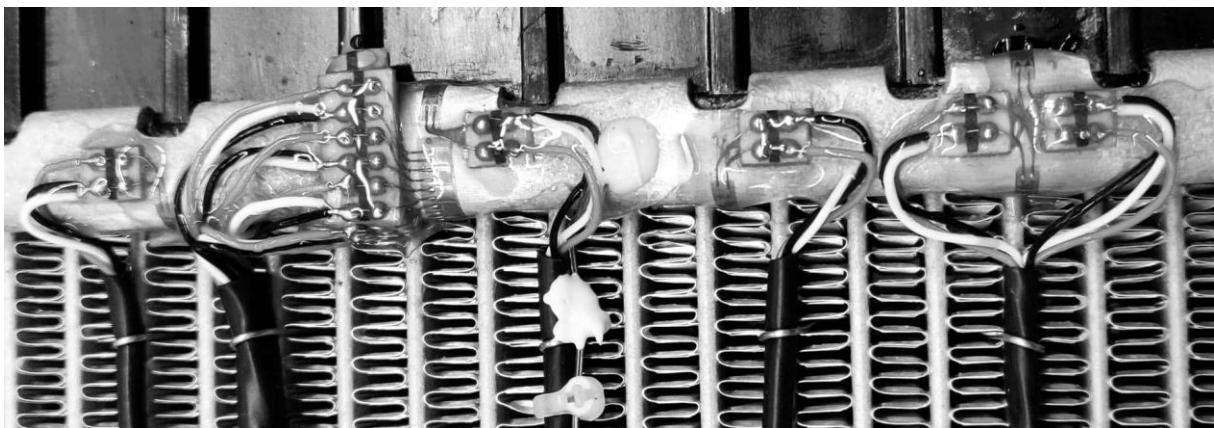
Figure 3-5: Fully instrumented header where the strain gauges are covered with transparent adhesive and protective covering material, and the thermocouple is covered with white two-component adhesive.

Table 3-1: Products used for installation.

Product No.	Product type	Product name	Manufacturer
1.	Etchant liquid	M-prep Conditioner A	Micro-Measurements
2.	Cleaning/ neutralizing liquid	M-prep Neutralizer 5A	Micro-Measurements
3.	Electronic cleaning spray	Electronic contact cleaner blue	Master
4.	Electric insulator tape	P-221	Nitto
5.	Adhesive	Z70	HBM
6.	Replacement for the HBM Z70 adhesive	CC-33a	Kyowa
7.	Soldering terminal	SFG-7T	Showa
8.	Protective nitrile rubber covering material	NG150	HBM
9.	Two-component adhesive	X60	HBM
10.	Protective silicone covering material	SG150	HBM

3.1.3   Setting up the radiator in the pressure pulsation rig

When the radiators are set up in the pressure pulsation rig during ordinary strength verification tests, they are set to rest against the interior of the rig with water as media. As this controlled experiment is set to measure displacements, vibrations and movements of the radiator are not desired, thus a new fixture was built. The radiator is fixtured in its ordinary mounting configuration where the tanks are mounted vertically, and the outlet is located at the bottom. However, instead of mounting it in its mounting positions, it rests on the side member. The mounting position of the radiator will not affect the strain measurements as the strain gauges are calibrated before the experiment. The outlet of the radiator is connected to the pressure pulsation rig with air as media while the inlet of the radiator is blocked to close the system. Air is used as media instead of water to avoid the influence of hygroscopy on the radiator tank, to keep the environment of the tank as simple as possible. In Figure 3-6 can the setup of the radiator be seen.

The strain gauges are then connected to the LMS measuring system where all strain gauges are mounted in a quarter bridge configuration because of the simple measuring case and the expected low effect by temperature. The LMS measuring system is thermal, meaning that the measurements depend on if the system has had time to heat up. The system normally takes 3h to heat up, for this experiment it was left to heat up overnight. A pressure gauge was then calibrated and mounted in the test rig to increase the accuracy of the pressure measurement. The thermocouples were then connected to the Pentronic measuring system before all instruments were added to the Siemens Signature Testing – advanced software, where all measurements have been processed. Before the first run at 100 kPa the strain gauges are shunt calibrated. When the strain gauges are manufactured and instrumented, there will be a slight difference in the resistive foil between each individual strain gauge. Thus, the shunt calibration is conducted to correct for the deviating resistance between each strain gauge. Before each run at the four internal pressures of 100, 160, 220, and 260 kPa, the strain gauges are also reset to measure no strain at resting condition so that any residual strains that have emerged are neglected.
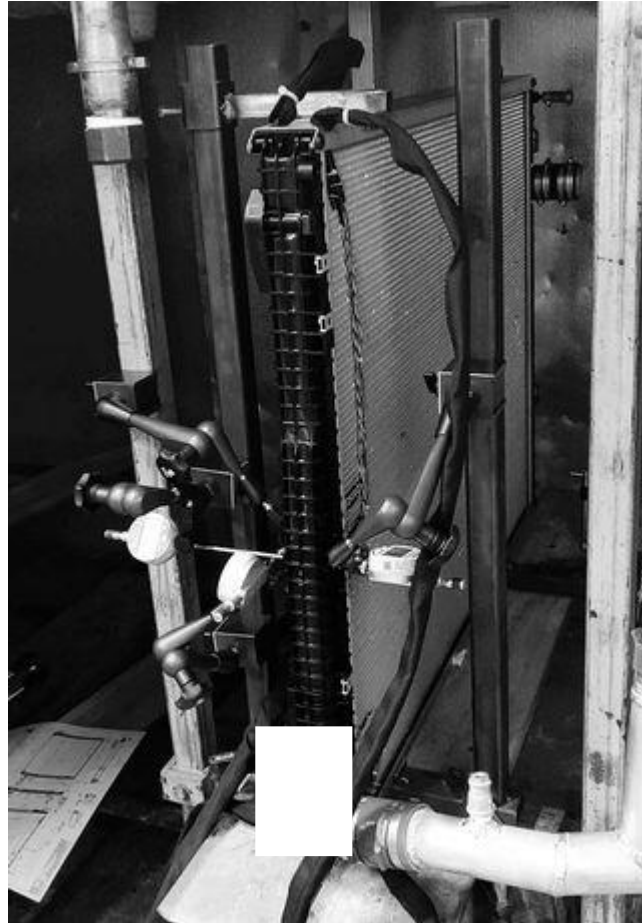
Figure 3-6: Radiator with dial indicators mounted in the pressure pulsation rig. Outlet connection pipe hidden due to confidentiality reasons.

The Sylvac dial indicators are then mounted to measure the relative displacement between them at the two sections of the radiator at header tab 7 and 20. If the fixture would move under load, a single dial indicator would not measure the displacements correctly. Having two dial indicators measuring as a pair eliminates the error, but it also means that the dial indicators must be placed opposite to each other. Measuring the displacement of the header tabs is done by mounting the indicators on the top of the header tabs and the bottom of the header. The displacement of the tank wall is measured on the engine and grill side. The displacement of the header wall is measured on the engine and grill side. The displacement of the tank top is measured by measuring at the top of the tank, as well as the bottom of the header. The method of measuring the displacements of the tank top is not desirable as the reference point at the header bottom is not optimal, it would be better to measure in a straight line, but that would lead to measuring on the inlet tank top which is a worse measuring condition. The placement of the dial indicators can be seen in Figure 3-7. The placement of the dial indicators is measured in order to compare the results against the FEA in the same position.
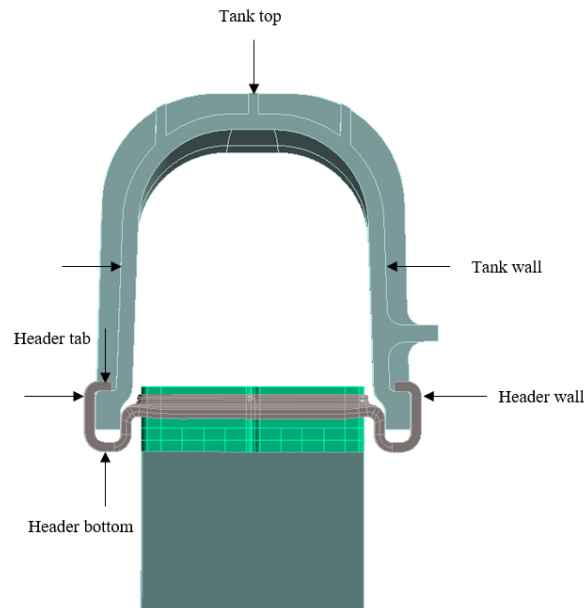
Figure 3-7: Placement of dial indicators.

The radiator is then subjected to pressure pulsation at the four different internal pressures. Between 160kPa and 260kPa is the range of the requirement specification set by the customer, and are therefore natural to analyse. The loading condition of 100kPa and 220kPa is used to see the expected linear behaviour of the strains and displacements. The linear behaviour of the strain measurements will be used as a reliability evaluation of the measurements. If the results behave linear, the reliability of the measurements will increase as the material is assumed to be operating under elastic conditions, and has therefore a linear behaviour when subjected to an external load. Thus, nonlinear results will decrease the reliability of many of the measurements. However, nonlinear behaviour can also be caused by the anisotropic material of the tank, the material operating in its nonlinear region, or the nonlinear behaviour of the EPDM gasket for instance. The calibration of the pressure gauge and the shunt calibration of the strain gauges are also conducted after the experiment is finished and compared to the initial calibration to ensure the reliability of the measurements.

3.2   Elasticity of PA66GF30 tank

The Young's modulus used for the fibreglass-reinforced polyamide tank in the original FE model is considering the effect of hygroscopy on the material. However, as the controlled experiment is set in a dry environment to simplify the environment and avoid the effect of hygroscopy, the material properties at dry as moulded (DAM) condition must be used instead. The Young's modulus provided by the manufacturer of the material is equal to 10 GPa measured according to the standard ISO 527 Type 1A. The specimen in the standard is 4mm, but the thickness of the radiator's tanks is 3 mm. The tanks' Young's modulus is expected to have an increase of 2-3% due to the difference in thickness, and a decrease of 15-20% because the fibre orientation is not parallel to the loading condition [18] as described in chapter 2. Leading to an expected Young's modulus of approximately 8,5 GPa. In the early stages of comparing the experimental and numerical results, the model was found to be unreasonably stiff. As fibreglass-reinforced polyamide is an anisotropic material, it was expected to be the parameter causing the stiffness in the model because of the varying thickness and the unknown fibre orientation. Thus, this experimental study was conducted to investigate the Young's modulus of the tank.

A section of the tank is cut out of the outlet side of the radiator tank. The section chosen is cut at header tab 14 and 17, so that it consists of three tank ribs as can be seen in Figure 3-8. This section is chosen as the tank is uniform and lacks mounting positions or other geometric irregularities. The tank feet of the section are then placed in between the blocks of a load cell, leaving the rest of the body outside of the loading cell as in Figure 3-8. The reference distance between the tank feet at rest is then measured with gauge blocks. The tank is then compressed 0,15; 0,3; 2,0; and 3,2 mm by measuring with

gauge blocks. The displacements were chosen to see how the required pressure would increase at both low displacements and higher, and determine if a linear simplification of the material can be used. To not accidentally compress the gauges blocks, the tank feet are compressed stepwise, and in between each step is the distance measured with the gauge blocks. Between each of the four compression cases, the load cell is set to the initial loading condition. The process is repeated three times for each compression case to see if the measurements are uniform.
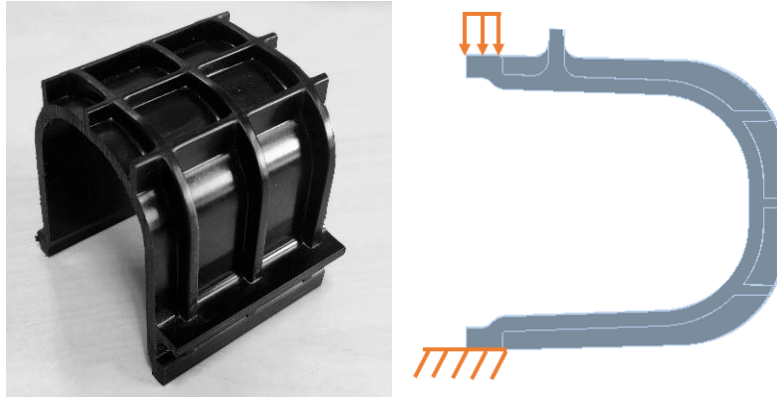
Figure 3-8: Cut out section of the radiator (left) and the loading case in the loading cell (right).

A similar cut is then conducted in the FE model to recreate the section tested in the load cell, where the model is meshed in 1 mm tetrahedron elements. The bottom tank foot surface in Figure 3-8 is made rigid, and the load of the load cell is applied as a pressure on the top tank foot surface. The applied pressure to the tank foot is the approximate force required in the load cell for the four different compression displacements. The results of the FEA and the average of the experiment in the load cell is then compared against each other. The Young's modulus is then iterated to match the experimental results.

The experiment was set in a load cell due to it being one of the few available rigs of the corporate partner where the applied load and displacements can be measured. A tensile testing machine was also available, but because of the geometry of the tank, extensometers could not be used to measure the displacement during tensile testing. Thus, the measuring of the displacements become more complex.

3.3   Verification of existing simulation methods

To be able to compare the numerical results to the experimental, the linear elastic FE model needs to be set up to emulate the experimental loading case. This chapter will describe how the FE model is set up, the current methods used to simulate the crimp joint, and how the experimental and numerical results are compared. A direct static structural solver is used for the simulations as the radiator is static and there is no interest in simulating the time dependency of the load case.

3.3.1   Meshing and connections

The meshing of the original FE model is coarse on the headers, using 4 mm linear hexahedron elements that are controlled to a smaller size in some areas around the inside radii and the complex geometries at the tubes. The fins, tubes, side plate, and side member are also meshed with 4 mm linear hexahedron elements, but at the connection to the headers, the mesh is refined, and in between the two headers are the mesh coarser. The tanks are meshed with 4 mm linear tetrahedron elements due to their complex geometry. The mesh at the header can be seen in Figure 1-1.

All connections that in practice are brazed together in the core of the radiator are in the FE model connected through node merge. Node merge is a connection type between one or several bodies that connects them to act as a single body. The bolted joints between the side members and the tanks are connected through a bonded contact at the adjacent surfaces. The bonded contact glues the surfaces together, allowing no separation or sliding between the nodes on the chosen surfaces.

3.3.2 Loads, boundary conditions and material properties of existing FE simulation method

The applied load when simulating the radiator is a simplification of the real loads in practice. In practice, the loads from the pressurized system do not spread evenly on the components [14]. Because of the heat exchange that occurs in the radiator, the components will expand unevenly depending on how far the different areas of the components are relative to the inlet of the radiator. The radiator will elongate more around the inlet as the coolant entering the system will be hotter as it is returning from cooling the powertrain. The inlet of the tubes will expand more as they are close to the inlet of the radiator, resulting in lower resistance of the coolant. At the outlet of the tubes, the tubes will elongate less as they are exposed to less heat than the inlet. There is also an uneven temperature exchange between the different tubes, as the coolant flow in each tube varies among the system [14]. Because of the uneven heat on the components, and loads due to the geometry, the radiator tubes will have an uneven elongation compared to each other as well.

Because of the complexity of the loading case in practice, it would lead to a complex loading case in the FEA as well. The system is therefore simplified to have an even pressure distributed normal to all internal faces of the system when analysing the work environment of the radiator. However, the loading case of the controlled experiment is simpler compared to a radiator connected to the powertrain. The loading case of the experiment is close to identical to the even loading distribution in the existing FEA. The internal pressure is set to 100 kPa during the verification of the existing FE simulation methods as the displacements measured during the experimental study was more reliable compared to the three other loading cases, as can be seen in chapter 4.1.2. To mimic the setup of the radiator in chapter 3.1.3, the surface of the side member that the radiator is resting on has been locked from translation in Z-axis, the sides of the upper side member have been locked from translation in X-axis, and the top surface of the side member has been locked from translation in Y-axis according to Figure 3-9.
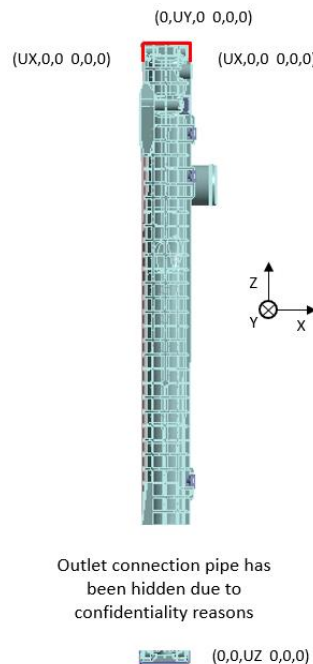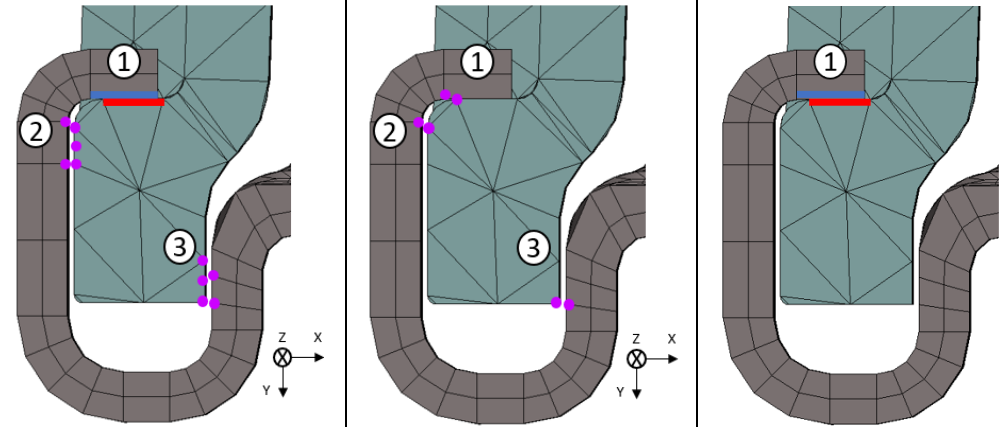
Figure 3-9: Schematic picture of how the radiator is constrained in the FE model.

The Young's modulus used for the fibreglass-reinforced polyamide tank in the original FE model was based on the effect of hygroscopy. However, as the controlled experiment is set in a dry environment, the material properties at DAM conditions have been used instead. From the investigation conducted on the elasticity of the PA66GF30 material in chapter 4.2, the Young's modulus was determined to E = 5,3 GPa. The Young's modulus for the aluminium is set to 69 GPa, and the steel is set to 200 GPa, provided by the material suppliers of the corporate partner.

3.3.3 Connection methods used for the crimp joint

The connection method of the crimp joint in the original FE model is a combination of using remote points and bonded contact as can be seen in contact A in Table 3-2. Remote points is a connection method where nodes are scoped and constrained in the six degrees of freedom (DOF) as desired. In the table (UX,0,0, 0,RY,0) reads as constrained from translation in X-axis and rotation around Y-axis. The scoped nodes can have different behaviour, the rigid behaviour used for contact A constrains the surfaces where the nodes have been scoped from deforming. This behaviour of the connection is similar to RBE2 elements that other FEA softwares utilizes. The XZ-plane on the FE model is rotated 6° around the Y-axis, due to the model being purposely built according to actual installation in the vehicle. This is the only connection processed in this report with a rotated coordinate system used to set the DOF settings. The contact can be implemented on a coordinate system with an axis parallel with the header, but then the contact would have to be constrained in both X and Z-axis, otherwise the model becomes underconstrained. Contact B and C are two other methods used by the corporate partner, where contact B only utilizes remote points, but with a different scoping technique and behaviour. The change in scoping technique prevents the connection from transferring an inner bending moment, in comparison to contact A. The coupled behaviour forces the underlying nodes to the remote points to share the same DOF settings. In contact C is only the bonded contact used to represent the crimp joint. As three methods are used by the corporate partner, all three methods have been implemented in the FE model to compare the results.

Table 3-2: Existing connection methods for the crimp joint.

Figure			
Contact name	Contact A	Contact B	Contact C
Contact pair 1	Bonded	Coupled (0,UY,0, 0,0,0)	Bonded
Contact pair 2	Rigid (UX,0,0, 0,0,0)	Coupled (UX,0,0, 0,0,0)	
Contact pair 3	Rigid (UX,0,0, 0,0,0)	Coupled (UX,0,0, 0,0,0)	

3.3.4 Verification of FE simulation methods

The attained result from the FE model is then compared to the experimental results. The stresses along the node lines of the outer bottom radii, where the strain gauges are mounted, are then compiled and sorted after position. The stresses on the outer top radii are studied on one node of each header tab, representing the positions of the strain gauges. The areas around the strain gauges are also studied to put the measurements into the perspective of how the crimp joint acts along the header in the FE model. The nodes where the stresses are evaluated can be seen in Figure 3-10. The numerical stresses are then compared against the experimental in diagrams. The displacements are also studied using a similar method as the stresses. The displacements of the components in the positions of the dial indicators are measured on the cross-section of the 7:th and 20:th header tabs. The displacements at the adjacent areas are also analysed to put the results of the experimental measurements into the perspective of how the whole crimp joint acts along the header in the FE model. The displacements are then paired in the same way as the measurements from the experiment, so that the displacements measured are relative to another part of the system and not the coordinate system. Lastly, the displacements are compared to the experimental results in diagrams.
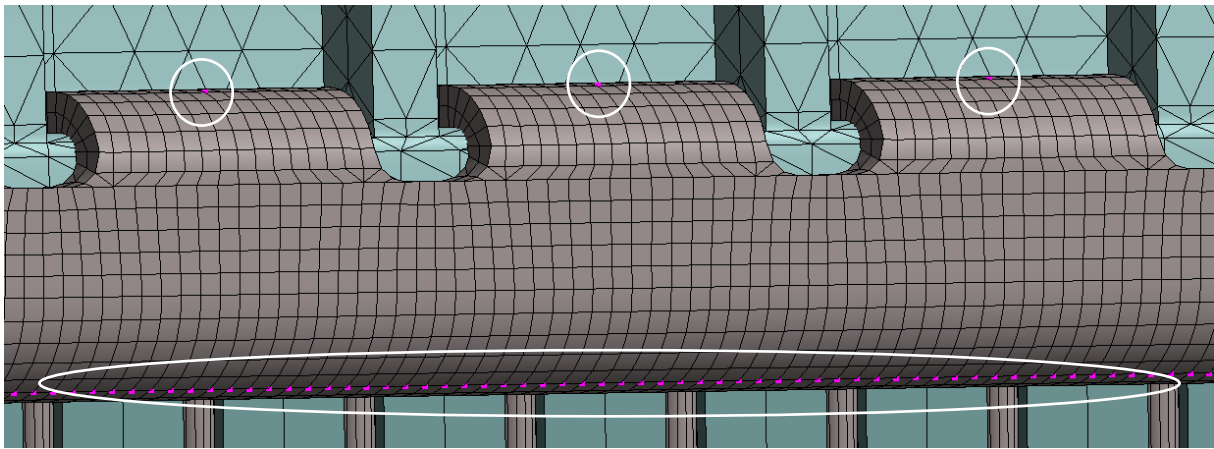
Figure 3-10: Scoped nodes (purple) where the stresses are analysed.

3.4 Development of FE simulation method

The optimization of the simulation method is supposed to result in a method that represents the structural mechanics of the crimp joint better than the existing methods. The goal of the new method is to better represent the actual behaviour of the crimp joint and minimize the margin of error to the furthest extinction possible, while still being a linear elastic model. In this chapter, the method of development is presented where the setup of the case study is included.

3.4.1 Setup of case study to represent the crimp joint with various connection methods

When setting up the boundary conditions of the crimp joint, several different methods and settings can be used and combined to represent the joint in the software, thus numerous simulations of the crimp joint are expected to be carried out to reach a satisfactory result of the developed method. To speed up the process of performing simulations on the crimp joint, the global model of the radiator is split up into a submodel. By splitting the global model, a section of the radiator can be isolated and tested separately. The submodel will then import the loads and displacements from the global model to the edges of the cut. Without importing the loads and displacements, the submodel will not give a correct representation of the cut-out section. The loads and boundary conditions of the submodel can then be set separately. As the loads and displacements are imported from an already existing analysis, the software does not have to solve the global model during every iteration of solving the submodel. Instead, the software only needs to solve the submodel, which minimizes the simulation time. The submodel represents the middle

section of the global model where the measuring took place in the experiment. The middle section is chosen as this part of the radiator is least affected by other components and change in geometry.

Before the case study can start, the submodel needs to be verified against the global model. If the submodel does not represent the global model correctly, the testing of methods on the submodel will not give a sufficient representation if the settings were to be transferred. Verifying the submodel completely against the global model is not necessary as the only area of interest regards the crimp joint. Therefore, the submodel is verified in the areas where the numerical results are compared against each other. As the stresses have similar behaviour on the engine and grill side in the global model, the study is set to only analyse the stresses on one side.

With the submodels can the different methods of representing the crimp joint in FEA be conducted faster, but the results on the crimp joint from the simulations in the submodel will not be exactly equal to the results from a simulation that would be conducted in the global model. Depending on the method used to represent the crimp joint in the global model, the imported displacements and loads will be affected. Therefore, the results from the simulations in the submodel will only give an estimation of what a result in the global model can look like. The disadvantage of having the imported loads from the global model affecting the results in the submodel can be used as an advantage if the results from chapter 4.3 are used. From the verification of the existing methods, contact B had the best correlation against the experimental results in the middle section of the radiator, and contact A had the worst. Contact A is therefore set in the global model, then Contact B is used to set the benchmark of the case study in the submodel. When the new methods of representing the crimp joint are tested in the submodel, they are only interesting to investigate further if they are reading similar stresses as the contact B.

The case study can then start by applying different methods of representing the crimp joint in the submodel. The designing of the new contacts are built on the presumed contacts in reality that occurs when the crimp joint is subjected to the internal pressure of the radiator. The top left corner together with the bottom right corner of the tank foot are presumed to have contact with the header as the crimp joint displaces. There might also be a contact with the bottom left corner of the tank foot. The new representations of the crimp joint can be seen in Table 3-3 together with the existing methods of representing the joint. The scoping of nodes is only conducted on the areas beneath the header tabs if nothing else is mentioned in the table. In Table 3-4 the contact definitions are explained in detail. Even though the scoping of the contacts are similar between the different contacts, the behaviour of the contact are influenced by the definition of the contact. Thus, testing different definitions of contacts is conducted until a satisfactory result is found.

The methods of representing the crimp joint that are seen as interesting in the submodel are then implemented in the global model. The results of the new methods are then compared against the experimental stress results as described in chapter 3.3.4, but to speed up the process, the methods are only compared on one side. If the models have a good correlation against the experimental results, they are compared against the experimental stresses of both engine and grill side, as well as against the experimental displacements.

Table 3-3: Contacts implemented in the submodel.
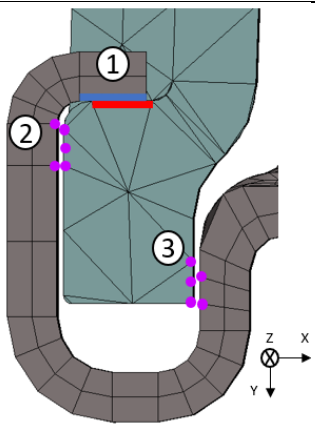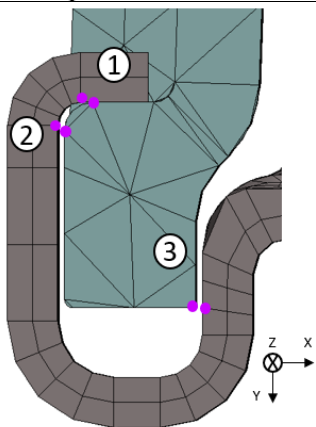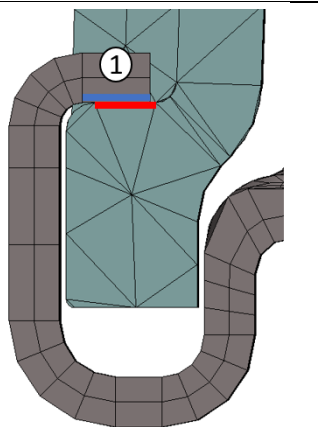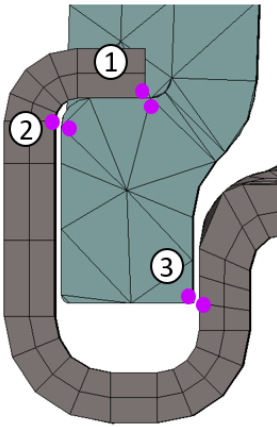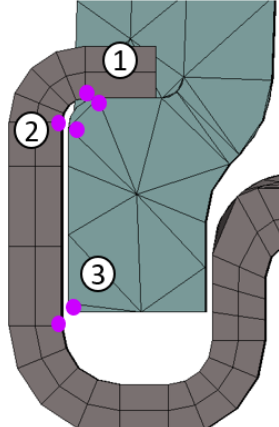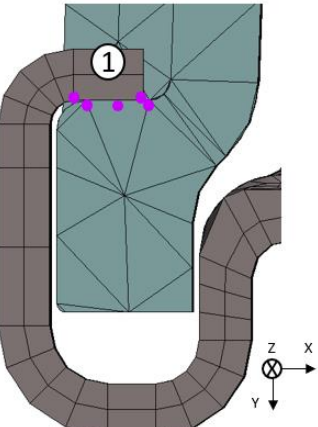
Figure			
Contact name	Contact A	Contact B	Contact C
Contact pair 1	Bonded	Coupled (0,UY,0, 0,0,0)	Bonded
Contact pair 2	Rigid (UX,0,0, 0,0,0)	Coupled (UX,0,0, 0,0,0)	
Contact pair 3	Rigid (UX,0,0, 0,0,0)	Coupled (UX,0,0, 0,0,0)	
Contact number	1	2	3
Contact pair 1	Coupled (0,UY,0, 0,0,0)	Coupled (0,UY,0, 0,0,0)	Coupled (0,UY,0, 0,0,0)
Contact pair 2	Coupled (UX,0,0, 0,0,0)	Coupled (UX,0,0, 0,0,0)	
Contact pair 3	Rigid (UX,0,0, 0,0,0)	Coupled (UX,0,0, 0,0,0)	

22
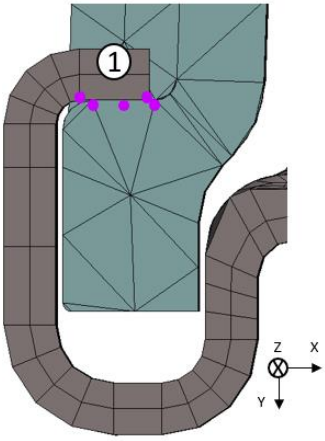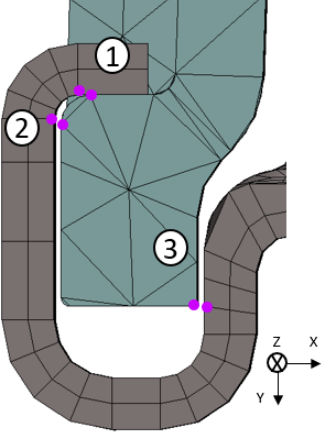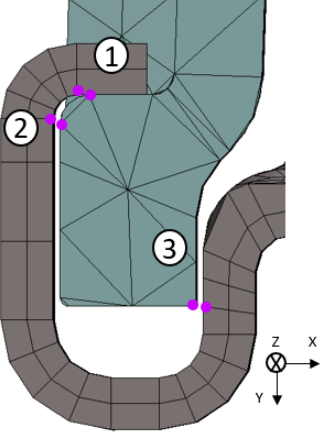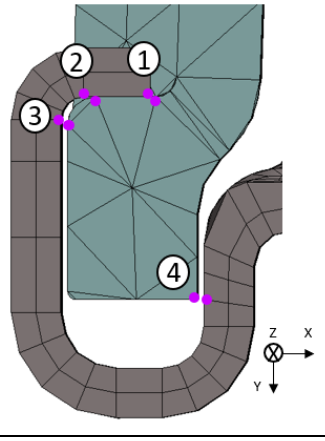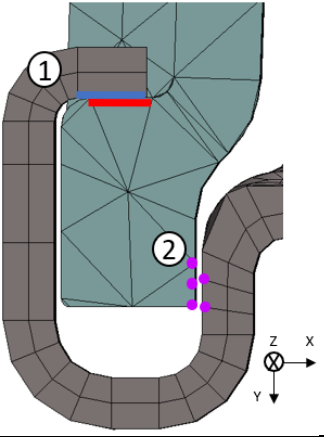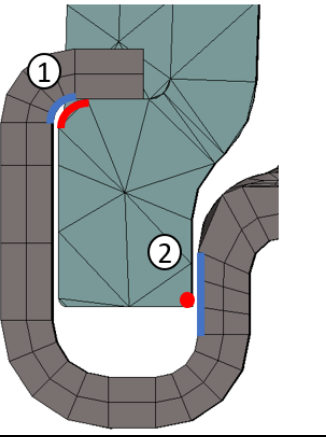
Figure			
Contact number	4	5	6
Contact pair 1	Deformable (0,UY,0, 0,0,0)	Rigid (0,UY,0, 0,0,0)	Coupled (0,UY,0, 0,0,0)
Contact pair 2		Rigid (UX,0,UZ, 0,0,0)	Coupled (UX,0,0, 0,0,0)
Contact pair 3		Rigid (UX,0,UZ, 0,0,0)	Coupled (UX,0,0, 0,0,0) Nodes scoped along the whole tank foot edge.
Figure			
Contact number	7	8	9
Contact pair 1	Coupled (0,UY,0, 0,0,0)	No separation	No separation
Contact pair 2	Coupled (0,UY,0, 0,0,0)	Rigid (UX,0,UZ, 0,0,0)	No separation
Contact pair 3	Coupled (UX,0,0, 0,0,0)		
Contact pair 4	Coupled (UX,0,0, 0,0,0) Nodes scoped along the whole tank foot edge.		
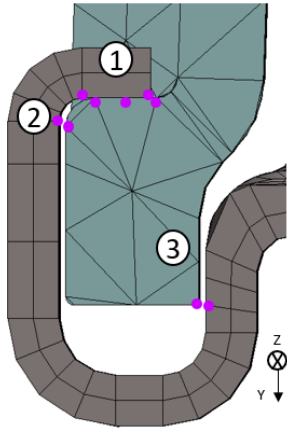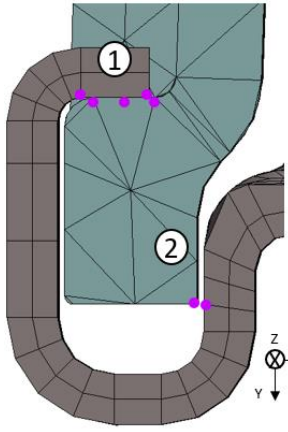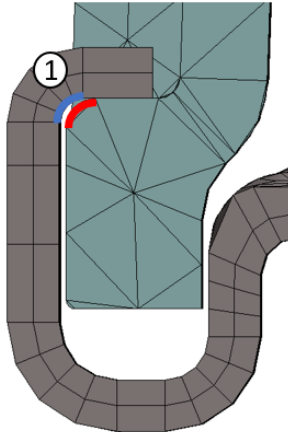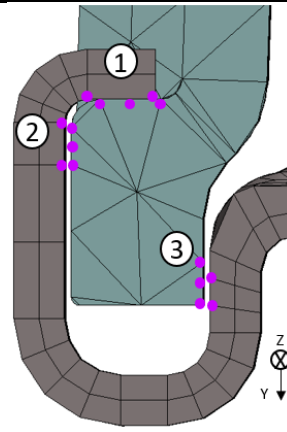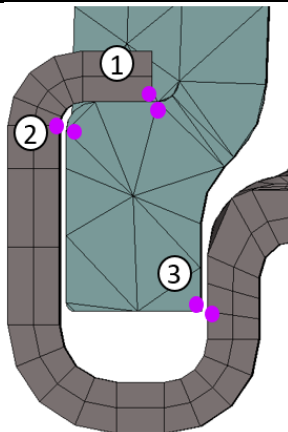
Figure			
Contact number	10	11	12
Contact pair 1	Rigid (UX,UY,UZ, 0,0,0)	Deformable (0,UY,0, 0,0,0)	No separation
Contact pair 2	Coupled (UX,0,0, 0,0,0)	Coupled (UX,0,0, 0,0,0)	
Contact pair 3	Coupled (UX,0,0, 0,0,0)		
Figure			
Contact number	13	14	
Contact pair 1	Rigid (UX,UY,UZ, RX,RY,RZ)	Rigid (0,UY,0, RX,RY,0)	
Contact pair 2	Rigid (UX,0,UZ, RX,RY,RZ)	Rigid (UX,0,UZ, RX,RY,0)	
Contact pair 3	Rigid (UX,0,UZ, RX,RY,RZ)	Rigid (UX,0,UZ, RX,RY,0)	

Table 3-4: Definitions of contacts.

Red and blue connection	These surfaces are connected using the faces of the geometry. The geometry of the face is therefore strongly affected by the geometry of the part. Several faces can be scoped as contact (red) or target (blue) bodies. This scoping method is used when default connection types such as bonded and no separation are implemented in the model.
Purple connection	These surfaces are connected using remote points. Remote points is a tool for controlling the degrees of freedom (UX, UY, UZ, RX, RY, RZ) of a body. The remote points can be used for defining a contact with more detailed control between points or nodes in the geometry. If remote points are used in the model, the solver will automatically use MPC equations to establish the connection, but MPC equations are only used for the remote points, not the rest of the model.
Bonded	The faces in the contact pair are bonded together, meaning that there is no sliding and no separation between the faces. If gaps occur in the contact, they will be closed, and any initial penetration will be ignored.
No separation	The faces in the contact pair are free to slide along each other without friction, but the contact will not be broken as no separation is allowed. Similarly to bonded contact, gaps will be closed and any initial penetration will be ignored.
Pure penalty formulation	Pure penalty is the default program-controlled formulation of contacts in ANSYS. During solving, the contact surfaces are separating and penetrating each other in iterations. The distance between the contacts is minimized by adding a force normal to the surface to resist separation and penetration. If the distance between the faces is short, the results are accurate.
MPC formulation	Multi-Point constraint formulation adds constraint equations internally so the displacements between the surfaces of the contact pair are tied together. MPC formulation can be used for both bonded and no separation contacts. If the formulation is combined with the bonded contact, the connection supports large deformation effects. If an MPC formulation is used, there will be no penetration between surfaces during calculations.
Rigid	This behaviour will cause the geometry of the remote points to not deform under load. However, the surface where the remote points have scoped can still displace and rotate. This behaviour acts similarly to what is commonly known as RBE2 elements.
Deformable	With this behaviour, the geometry of the remote points is free to deform under load. This behaviour acts similarly to what is commonly known as RBE3 elements.
Coupled	With the coupled behaviour, the underlying nodes of the remote point will be forced to share the same DOF constraint, leading to a connection where the surface of the remote points is constrained from displacing and rotating.

3.4.2 Verification of developed FE simulation method at increased pressure

During the experimental stress analysis in the pressure pulsation rig, the radiator was subjected to an internal pressure of 100, 160, 220 and 260 kPa. These experimental results will be used to correlate the newly developed method against. When the loads are increased, any existing errors at low loads will be amplified. Having a method that correlates against the top range of the work environment is crucial in order to determine the fatigue life of the radiator. The method used to compare the numerical and experimental results is explained in chapter 3.3.4.

4 RESULTS AND ANALYSIS

4.1 Controlled experiment

To determine the margin of error of the existing methods of representing the crimp joint in FEA, the numerical methods needs to be compared against measured data. In this chapter, the data which the numerical methods are to be compared against are presented and analysed.

4.1.1 Experimental stress analysis

The measured strain is pulsating together with the pressure applied to the system creating a strain graph of each gauge, oscillating at an elevated midline according to Figure 4-1. At the beginning of the run, the pressure is ramped up with caution, causing the irregular graph at the start. The time of each pressure pulsation was also made longer during the run, causing the abruption in the graph. Later was one adjustment of the maximum pressure made after it was discovered to be too high. After the pressure pulsation rig was configured, it can be seen that the measurements become more stable, but with a slight increase of both the maximum and minimum strain over time. The slight increase of strain is presumably caused by the increase in temperature which is the only variable that is not controlled during the run. The temperature at the same strain gauge can be seen in Figure 4-2. As each run is conducted over a long period of time, each pulsation cannot be viewed without looking at the run for a shorter period. In Figure 4-3 is the run shown under a time of 5,95 seconds after the rig had been configured. Here it can be seen that the pressure pulsates between approximately 13 and 102 kPa, resulting in a varying strain between 115 to 528 µε. The rig does not completely empty all the pressurised air between the pulses, resulting in a pressure of 13 kPa between each pulsation.
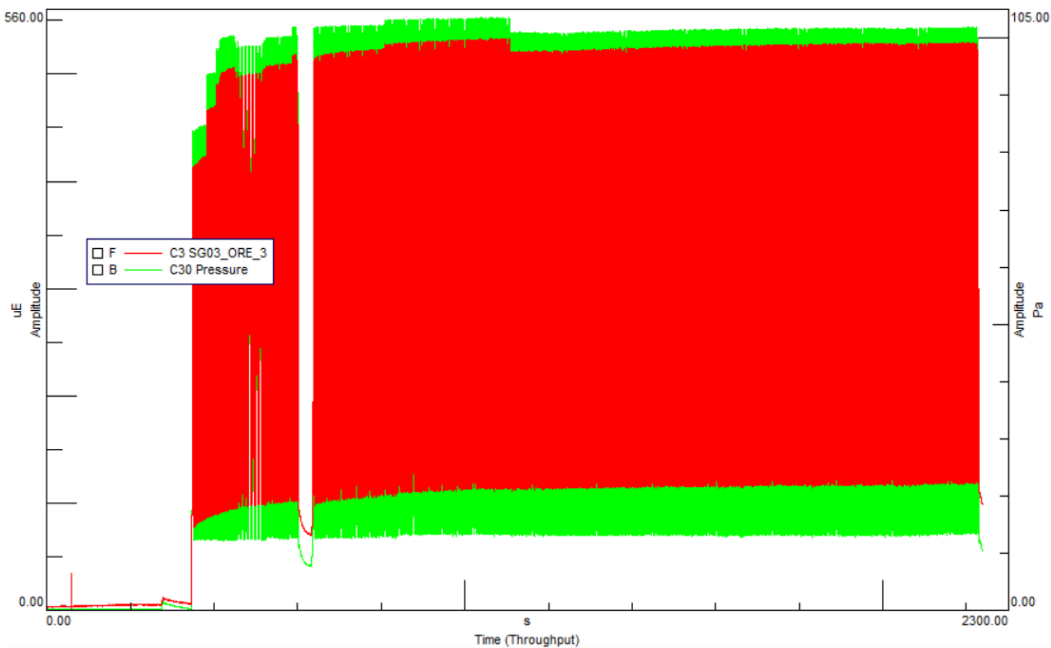
Figure 4-1: Strain measurement of strain gauge SG03_ORE_3 at 13-102 kPa pressure pulsation.
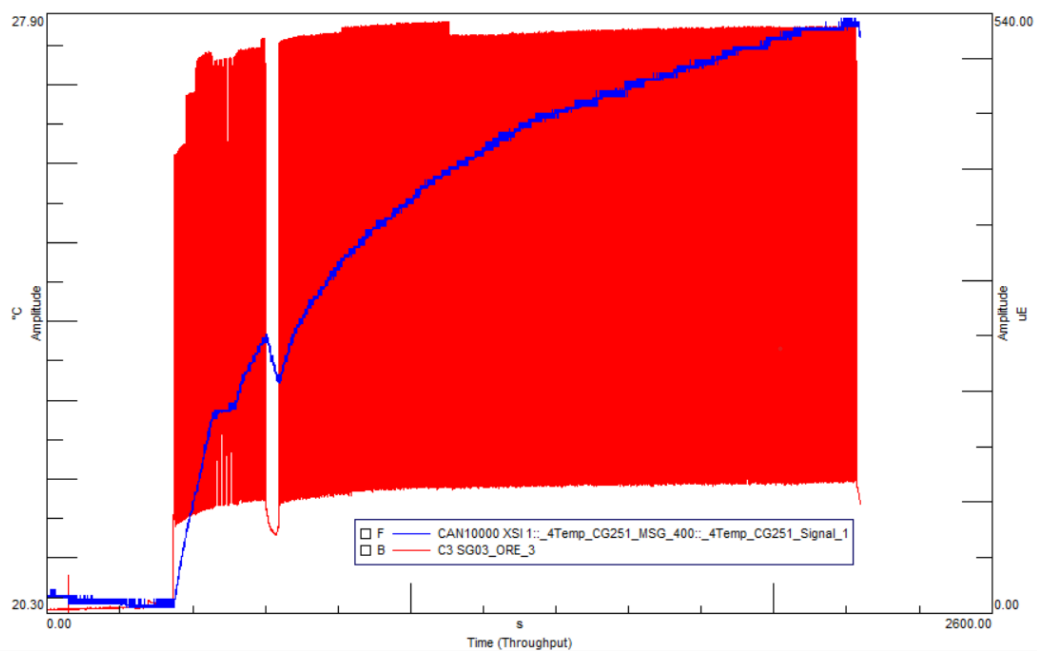
Figure 4-2: Strain measurement of strain gauge SG03_ORE_3 and temperature measurement at 13-102 kPa pressure pulsation.
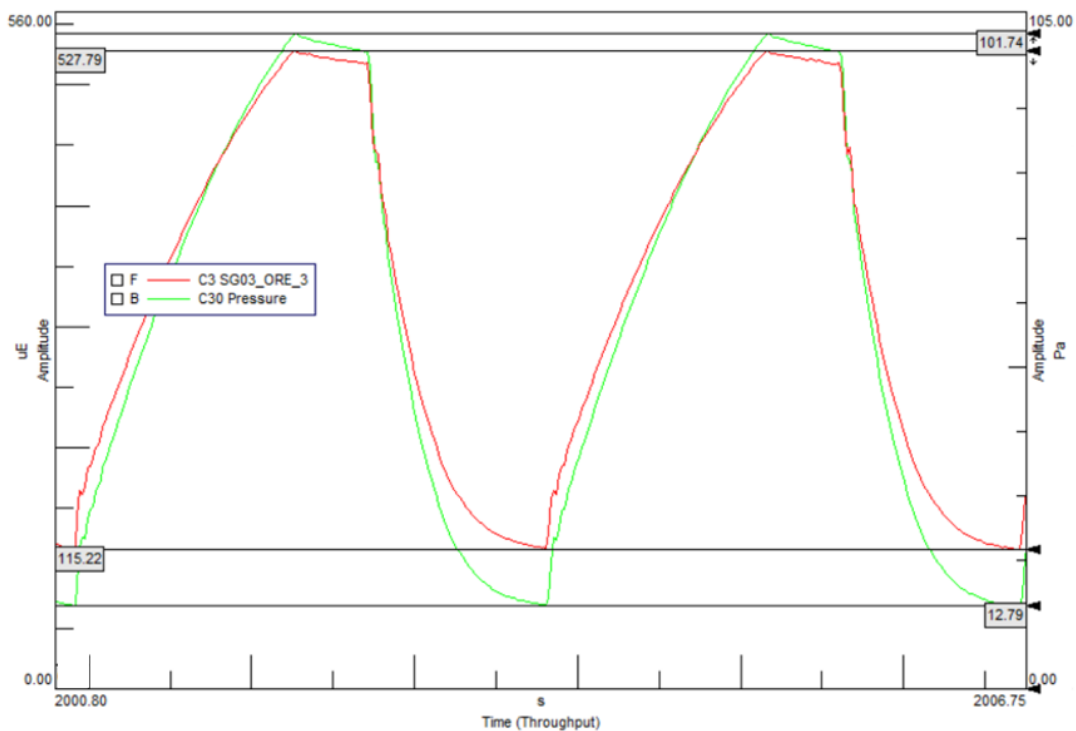
Figure 4-3: Section of the strain and pressure measurement.

The amplitude and peak to peak (p-p) amplitude of the measured strain is not the actual maximum strain of the material at the applied 102 kPa pressure as there is a residual pressure of 13 kPa inside the rig. The amplitude does not show the strain of each pulsation as the radiator is not at rest between the pulsations, meaning that it is not known if the material has been slightly yielding when it is run for the first time. The problem with the p-p amplitude is that it only shows the strain caused at the pressure difference ΔP of the system. As the strain could not be measured directly, the p-p amplitude of the strain measurements is used to extrapolate the strain at each given pressure run. This is a valid method when the p-p amplitude is constant and the system behaves linearly. If the p-p amplitude would not have been

27

constant, the strain caused by each pulsation would vary during the run, making the extraction of the p-p amplitude unreliable. The strain is therefore extrapolated according to:

$$\varepsilon = \frac{\Delta\varepsilon}{\Delta P}P,$$

where $\Delta\varepsilon$ is the p-p amplitude of the strain measurements, ΔP is the p-p amplitude of the measured pressure, and P is the maximum pressure of each run. Based on the measured strains, the stresses can be calculated according to Hooke's law for uniaxial stress states:

$$\sigma = \varepsilon E$$

The measurements of each strain gauge are then connected to its nodal position in the FE model where the attained data from the experiment can be compared to the data from the existing FEA. An example of the stresses calculated based on the strain at the outer radius of the middle section on the engine side, can be seen in Figure 4-4. All calculated stresses at the four runs can be seen in Table 4-1 and an overview of the instrumentation can be seen in Appendix A. As can be seen, the highest stresses are located around the first header tabs, close to the outlet as expected. However, the stresses located on the top radius is found to be close to non-existent, which differ from what was expected. It can also be seen that there is no linear development of the stresses located at the outer top radius, but this is presumably due to the low loads that the header tabs are subjected to.
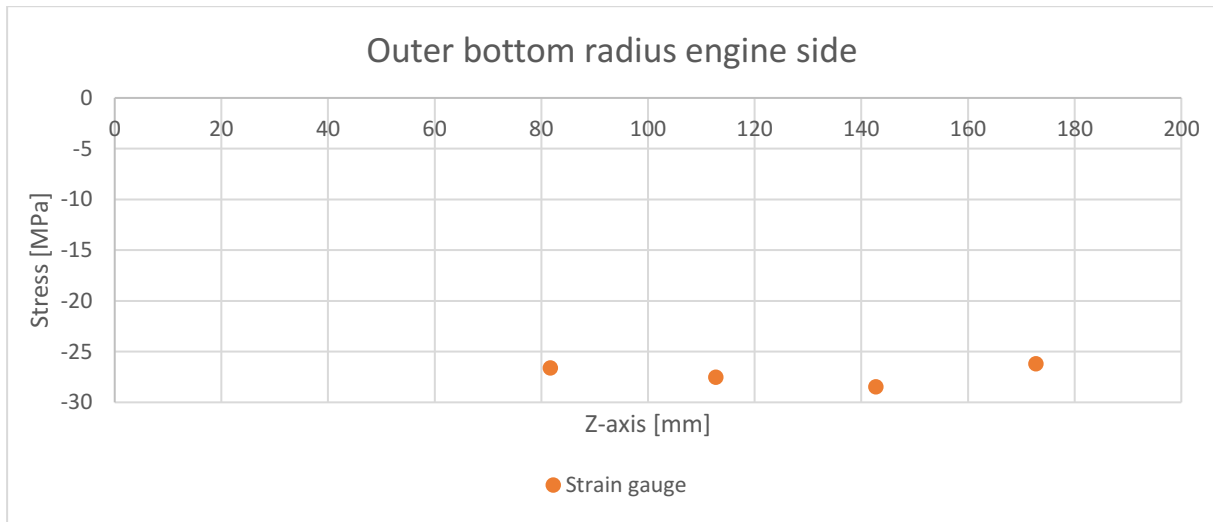
Figure 4-4: Strain gauge measurements connected to nodal positions in the FE model.

Table 4-1: Summary of stresses of each location for all pressure levels.

Name	100 kPa [MPa]	160 kPa [MPa]	220 kPa [MPa]	260 kPa [MPa]
SG01_TRE_3	-1,71	-2,39	-1,19	-1,53
SG02_TRE_6	-1,24	-1,42	-0,89	-1,02
SG03_ORE_3	-31,94	-51,62	-73,30	-87,22
SG04_ORE_4_5	-39,31	-63,93	-90,78	-107,49
SG05_ORE_6	-40,55	-66,69	-94,88	-113,33
SG06_ORE_7_5	-36,13	-59,90	-85,35	-102,46
SG07_TRG_3	-1,78	-3,95	-3,13	-4,01
SG08_TRG_6	-1,55	-2,09	-2,08	-1,24
SG09_ORG_3	-31,55	-52,14	-73,07	-87,73
SG10_ORG_4_5	-39,00	-64,67	-90,78	-109,75
SG11_ORG_6	-37,68	-62,21	-87,58	-104,87
SG12_ORG_7_5	-35,04	-58,26	-82,45	-99,11
SG13_TRE_18	-1,47	-2,98	-5,06	-8,82
SG14_TRE_21	-0,47	-1,04	-1,79	-3,14
SG15_ORE_18	-26,59	-47,59	-72,48	-90,87
SG16_ORE_19_5	-27,52	-48,19	-70,32	-86,56
SG17_ORE_21	-28,45	-48,78	-70,02	-85,98
SG18_ORE_22_5	-26,20	-44,53	-64,37	-80,95
SG19_TRG_18	-1,55	-2,54	-2,60	-1,39
SG20_TRG_21	-0,85	-1,72	-3,05	-4,45
SG21_ORG_18	-30,31	-50,50	-71,36	-86,27
SG22_ORG_19_5	-31,01	-50,58	-70,91	-85,40
SG23_ORG_21_1	-22,10	-37,82	-54,54	-67,24
SG24_ORG_21_2	-27,29	-46,17	-66,15	-80,88
SG25_ORG_21_3	-27,13	-44,61	-63,55	-77,52
SG26_ORG_21_4	-26,75	-44,83	-63,25	-76,35
SG27_ORG_21_5	-27,83	-46,10	-64,59	-77,30
SG28_ORG_22_5	-26,36	-43,56	-61,32	-74,17
SGXX_AAB_YY.Y SG = Strain gauge XX = strain gauge number AA = position of strain gauge: OR = outer bottom radius, TR = outer top radius B = side of radiator: E = engine side, G = grill side YY.Y = header tab number.				

The comparison of the shunt calibration before and after the experimental study can be seen in Table 4-2. The maximum deviation of the calibration is 1.5% in one of the strain gauges, meaning that the strain measurements of that specific strain gauge have an error of up to 1.5% due to calibration, but for the other strain gauges, the margin of error is smaller. The calibration of the pressure gauge proved to be 100% accurate to the initial, resulting in precise pressure measurement. The linearity of the measured stresses at the four loading conditions can be seen in Figure 4-5. It can here be seen that all measurements have a good linear convergence, indicating that the material is operating in its linear elastic region. The strain gauge SG15 placed at the outer bottom radius on the engine side at header tab 18, has the least linear convergence, but is still within an acceptable margin.

Table 4-2: Margin of error due to differences in shunt calibration before and after the experiment.

Strain gauge	Initial sensitivity	New sensitivity	Margin of error
SG01_TRE_3	0,000538557	0,000540592	-0,4%
SG02_TRE_6	0,000534112	0,00053578	-0,3%
SG03_ORE_3	0,000538724	0,00053957	-0,2%
SG04_ORE_4_5	0,000533793	0,000533434	0,1%
SG05_ORE_6	0,00053183	0,000531319	0,1%
SG06_ORE_7_5	0,000524441	0,000532268	-1,5%
SG07_TRG_3	0,000535987	0,000539059	-0,6%
SG08_TRG_6	0,000534232	0,000536099	-0,3%
SG09_ORG_3	0,000533848	0,000534718	-0,2%
SG10_ORG_4_5	0,000533473	0,000533098	0,1%
SG11_ORG_6	0,000535006	0,000534311	0,1%
SG12_ORG_7_5	0,000538126	0,000537527	0,1%
SG13_TRE_18	0,000537607	0,000539794	-0,4%
SG14_TRE_21	0,00053886	0,000540831	-0,4%
SG15_ORE_18	0,000537791	0,00053945	-0,3%
SG16_ORE_19_5	0,000537615	0,000539004	-0,3%
SG17_ORE_21	0,000538397	0,000539474	-0,2%
SG18_ORE_22_5	0,000538257	0,000539953	-0,3%
SG19_TRG_18	0,000538103	0,000539446	-0,2%
SG20_TRG_21	0,000543614	0,000545377	-0,3%
SG21_ORG_18	0,000538013	0,000538895	-0,2%
SG22_ORG_19_5	0,000537863	0,000538895	-0,2%
SG23_ORG_21_1	0,000539398	0,000539389	0,0%
SG24_ORG_21_2	0,000539756	0,000539706	0,0%
SG25_ORG_21_3	0,000562166	0,000562531	-0,1%
SG26_ORG_21_4	0,000561675	0,000562093	-0,1%
SG27_ORG_21_5	0,000566904	0,000567666	-0,1%
SG28_ORG_22_5	0,000568805	0,000569616	-0,1%

SGXX_AAB_YY.Y
SG = Strain gauge
XX = strain gauge number
AA = position of strain gauge: OR = outer bottom radius, TR = outer top radius
B = side of radiator: E = engine side, G = grill side
YY.Y = header tab number
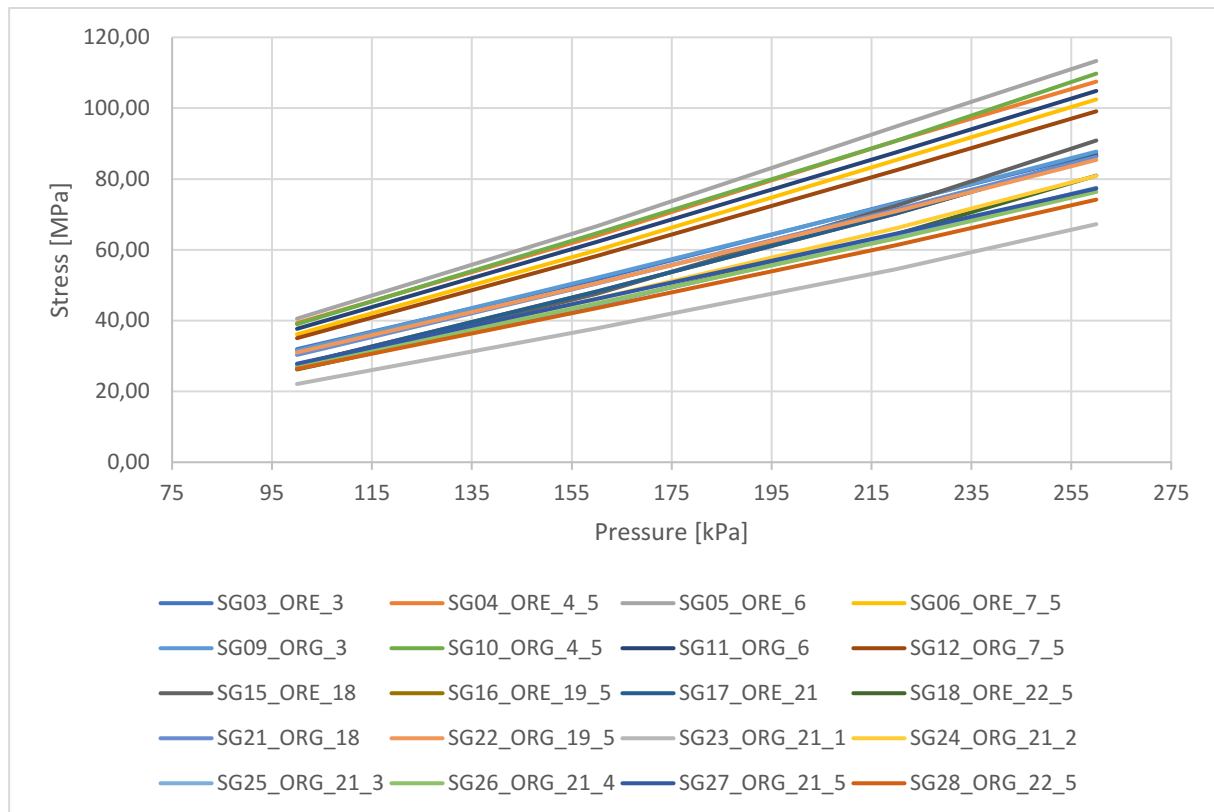
Figure 4-5: Linearity of stress at the outer bottom radius.

The measured temperatures on the header wall, tank and tank ribs at the loading case 100 kPa can be seen in Figure 4-6. Here it can be seen that Signal 6 and Signal 7 are measuring lower temperature than the other thermocouples. Signal 6 is positioned at the tank rib on the engine side of the outlet section, while Signal 7 is positioned at the tank on the engine side of the middle section. The results of the other runs are similar where Signal 6 is measuring the lowest temperature compared to the other thermocouples. Measuring the temperature at the tank rib was conducted to determine if the material properties of the ribs had to be made stiffer compared to the rest of the tank, due to the lower temperature. Even though Signal 6 is measuring a lower temperature at the tank rib, the tank ribs material properties cannot be made stiffer due to the temperatures measured by Signal 8. Signal 8 is also measuring the temperature on the tank rib, but the temperature measured is similar to the other thermocouples positioned on the header wall, meaning that the heat is evidently spreading to the tank ribs as well. Because of these results, the tank and tank ribs are set to have the same material properties when developing the FE simulation method.

Figure 4-6: Temperatures at the header and tank during the pressure pulsation at 100 kPa.

4.1.2   Experimental displacement analysis

The attained data from the displacement measurements pulsates with the applied pressure similar to the measured strain. However, unlike the strains, the measured displacements are not always as uniform throughout the run causing an uncertainty connected to some of the measurements. The attained displacements at 100 kPa are uniform and have 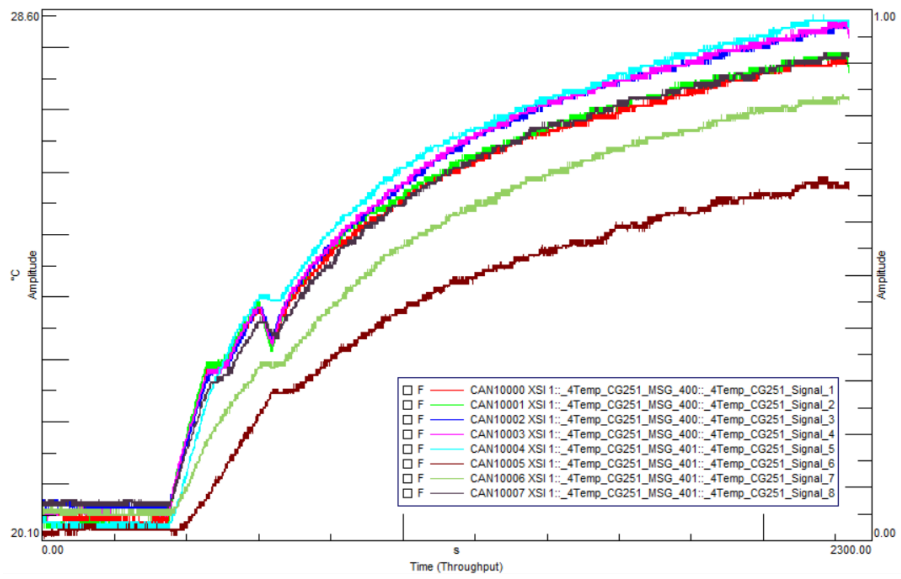a fairly consistent p-p amplitude. The results of the middle section can be seen in Figure 4-7 to Figure 4-11, the displacements at the outlet section and the displacements of the other pressures can be seen in Appendix B. In the figures, it can be seen how the radiator moves during the run by studying how the minimum and maximum displacement increases or decreases as a pair in some of the figures. Similar to the strain measuring, the amplitude and p-p amplitude, cannot be used directly to determine the displacements at each pressure. The displacements are instead extrapolated according to:

$$\delta = \frac{\Delta\delta}{\Delta P}P$$

where $\Delta\delta$ is the p-p amplitude of the displacements. When determining the p-p amplitude of the measured displacements, single peaks are neglected as they can be caused by vibrations and movement of the radiator. Instead, the p-p amplitude is extracted in sections where the displacements have a consistent p-p amplitude. Like the strain measurements, the linear extrapolation is valid if the material behaves linearly. The maximum displacements from the experiment are summarised in Table 4-3. The displacement measurements are then connected to its nodal position in the FE model where the attained data from the experiment can be compared to the data from the existing FEA. An example of the displacements measured on the header tab on the engine side of the middle section can be seen in Figure 4-12.

32
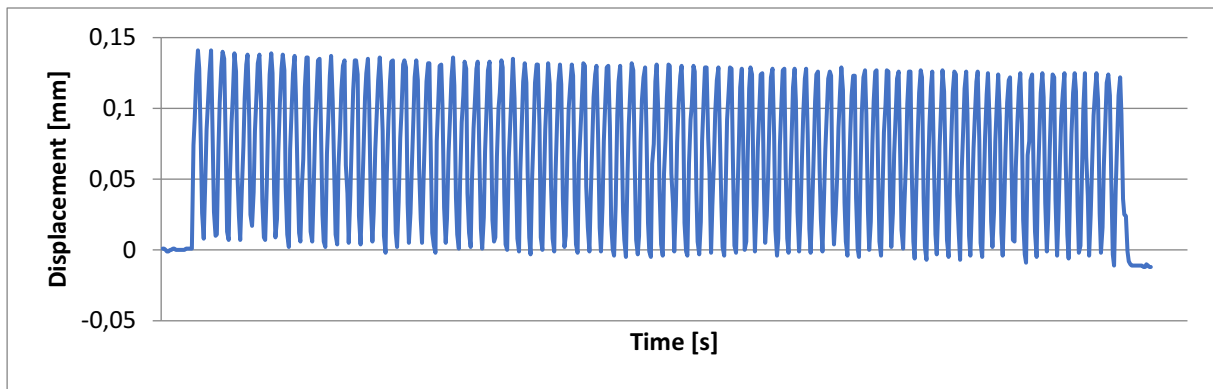
Figure 4-7: Displacements of the header wall positioned at the middle section, at the load of 100 kPa.
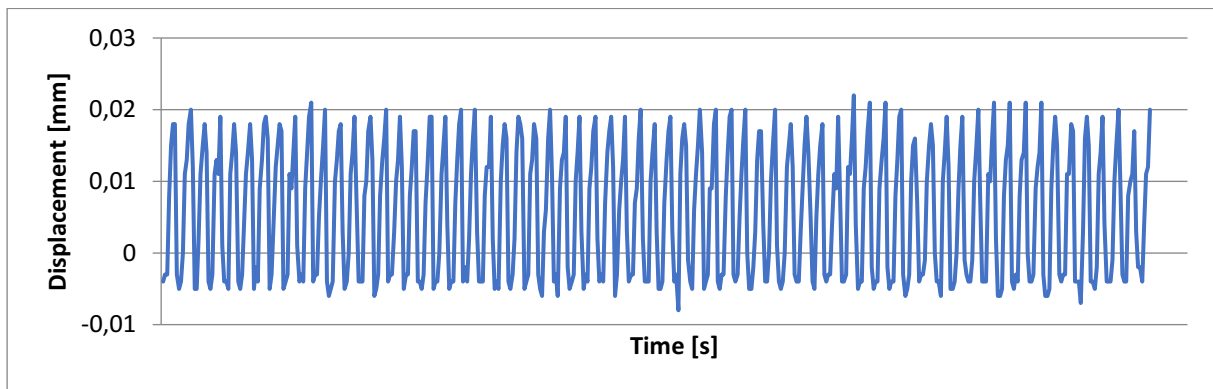
Figure 4-8: Displacements of the header tab positioned at the grill side of the middle section, at the load of 100 kPa.
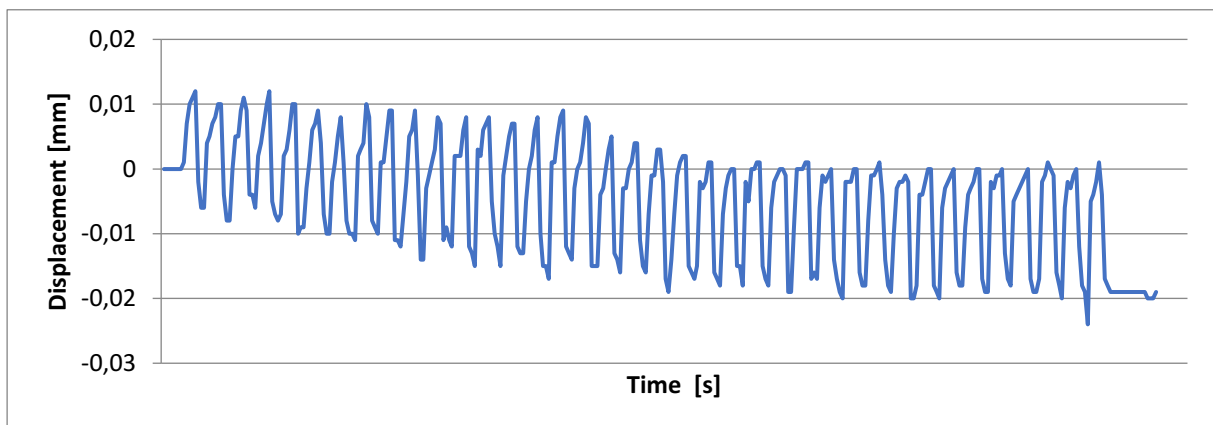
Figure 4-9: Displacements of the header tab positioned at the engine side of the middle section, at the load of 100 kPa.
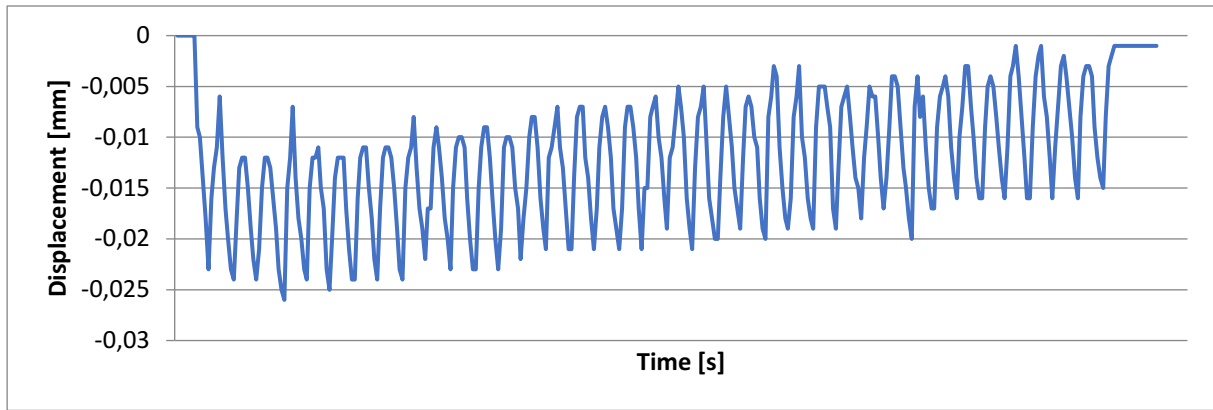
Figure 4-10: Displacements of the tank top positioned at the middle section, at the load of 100 kPa.
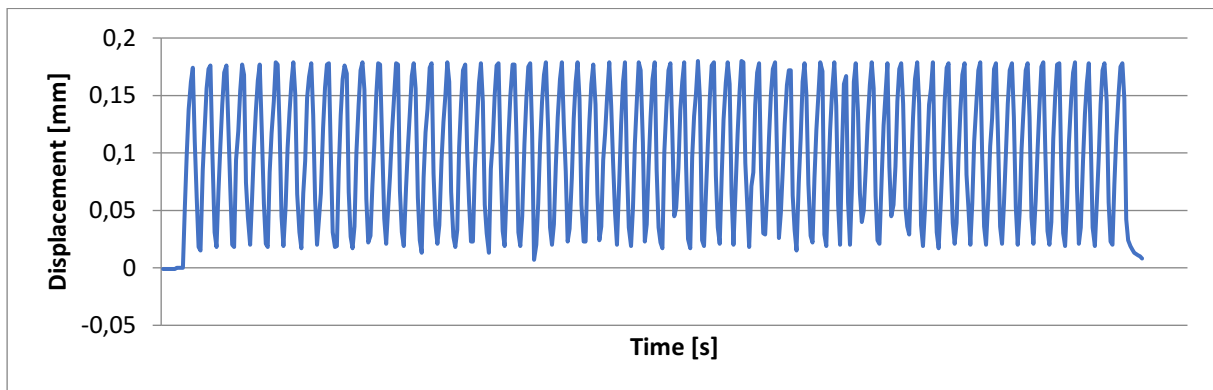
Figure 4-11: Displacements of the tank wall positioned at the middle section, at a load of 100 kPa.

Table 4-3: Summary of displacement measurements.

Section	Position	100 kPa [mm]	160 kPa [mm]	220 kPa [mm]	260 kPa [mm]
Outlet	Engine header tab	0,03	0,039	0,049	0,078
	Grill header tab	0,018	0,022	0,034	0,052
	Header wall	0,149	0,247	0,352	0,443
	Tank wall	0,288	0,463	0,663	0,704
	Tank top	-0,022	-0,056	-0,08	-0,092
Middle	Engine header tab	0,022	0,06	0,088	0,094
	Grill header tab	0,028	0,028	0,028	0,036
	Header wall	0,151	0,212	0,304	0,445
	Tank wall	0,18	0,34	0,46	0,571
	Tank top	-0,018	-0,045	-0,069	-0,076
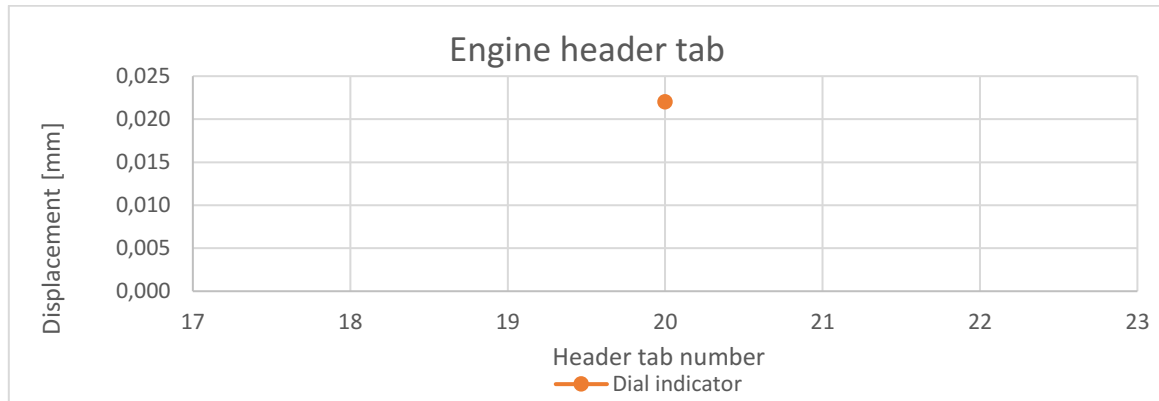
Figure 4-12: Dial indicator measurement connected to its nodal position in the FE model.

To verify the usage of linear extrapolation to calculate the total displacement during loading, the linearity of the displacements is studied, these can be seen in Figure 4-13 to Figure 4-17. In the figures, it can be seen that the tank walls, header walls and tank tops have the best linear convergence at the four loading conditions, whereas the behaviour of the header tabs and header wall is more irregular. Thus, the linear extrapolation is only valid for extrapolating the displacements at the header wall, tank wall and tank top. The overall reliability of the measurements of the header wall and tank wall, is judged to be more accurate as the data from the measuring is the most uniform, these measurements will therefore have the highest priority when developing the FE simulation method. The reliability of the tank tops is lower due to the irregular measurements, and will therefore not be considered in the development of the FE simulation method. The measurements of the header tabs have the lowest reliability out of the selection of measurements, due to the displacements being irregular with no linear convergence. The reason why the measurements of the header tabs and tank tops have no linear convergence can be due to the EPDM gasket, which has nonlinear material properties. As the reference of the tank top is the bottom of the header, the displacements of the tank top can be affected by the gasket as well, resulting in the irregular displacement measurements. However, the error that entails the usage of linear extrapolation is expected to be small. Thus, the displacements are used to compare against the numerical analysis when verifying the existing methods of representing the crimp joint, to check if the results are of the same order of magnitude.
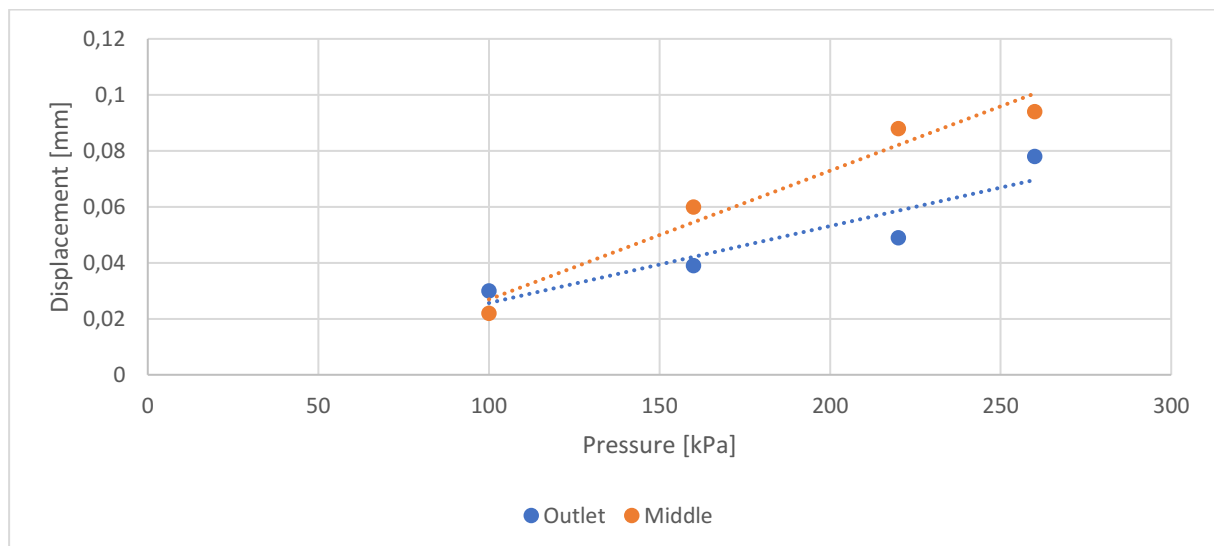

Figure 4-13: Linearity check of displacements at the engine header tabs.
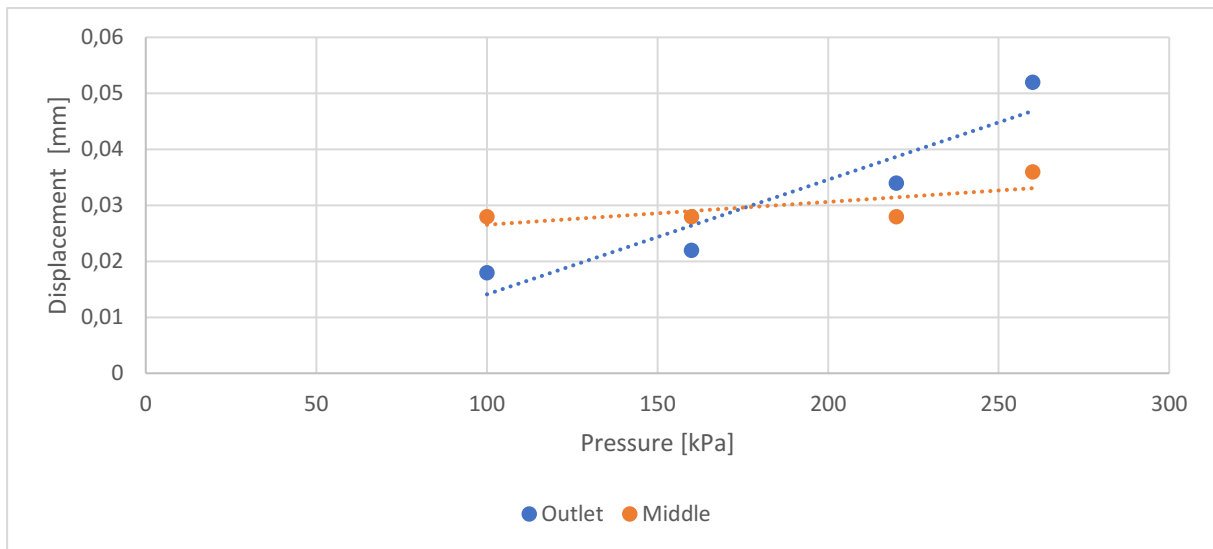
35

Figure 4-14: Linearity check of displacements at the grill header tabs.
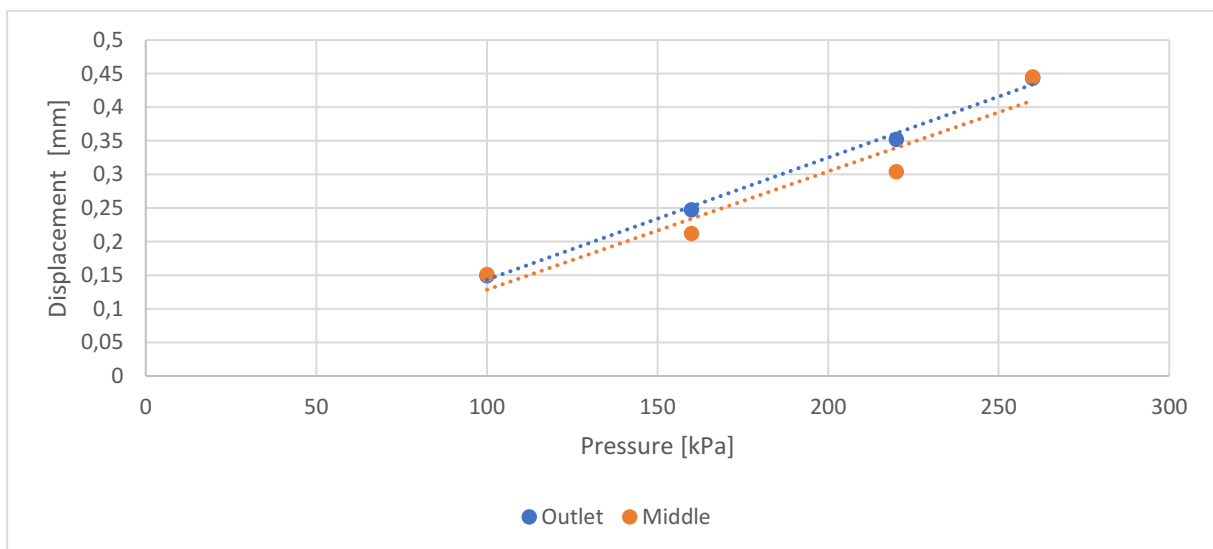
Figure 4-15: Linearity check of displacements at the header walls.
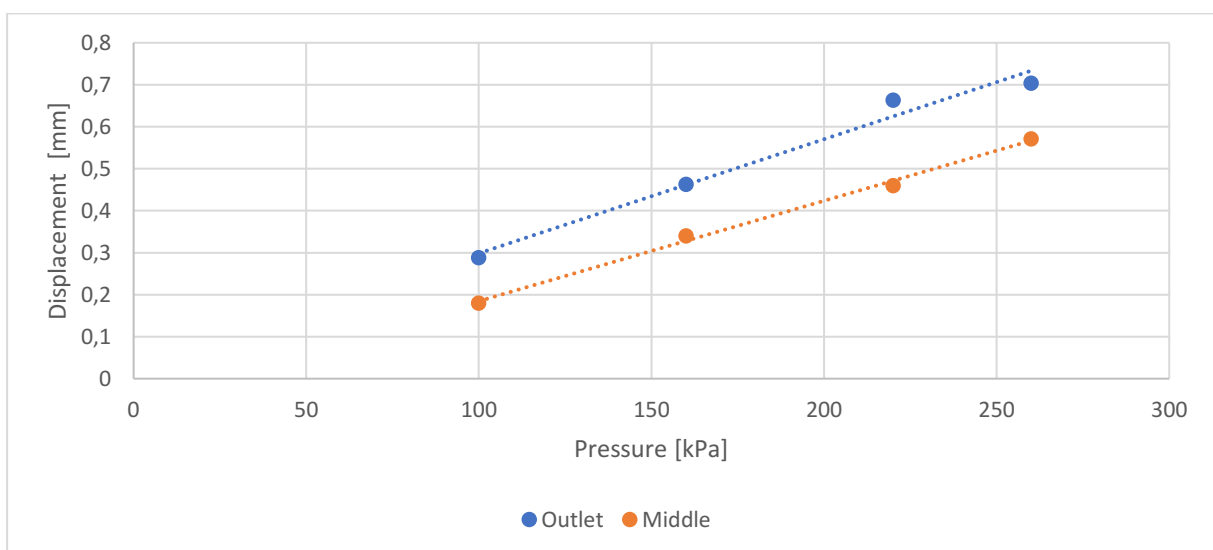
Figure 4-16: Linearity check of displacements at the tank walls.
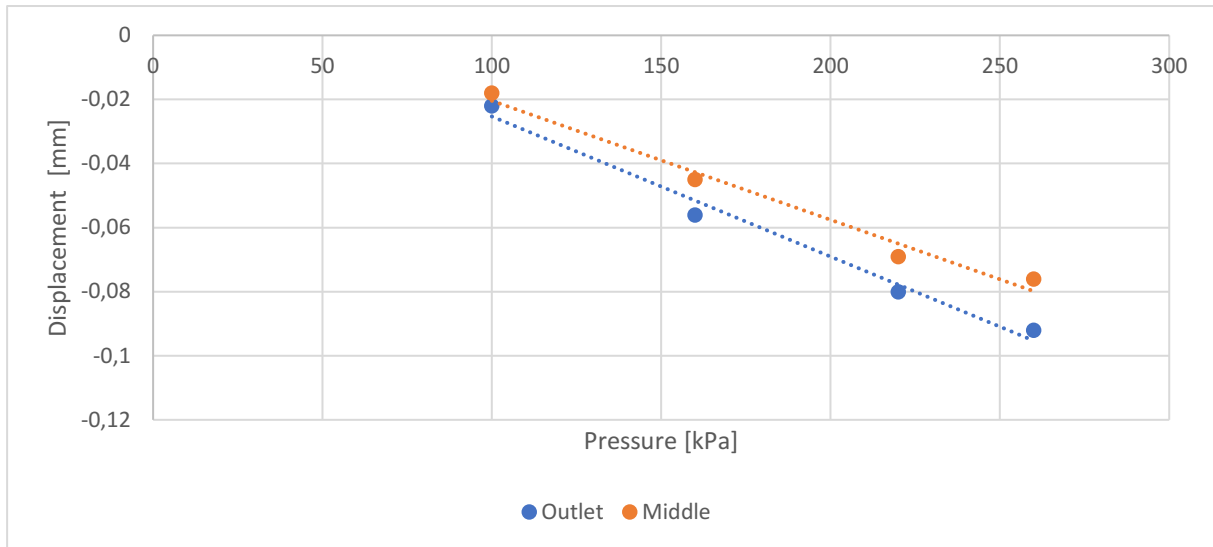
Figure 4-17: Linearity check of displacements at the tank top.

4.2   Elasticity of PA66GF30 tank

As the Young's modulus of the anisotropic fibreglass-reinforced polyamide tank could not be sufficiently determined through the material properties provided by the material supplier, together with existing research contribution, this study was conducted to determine the missing material property.

The measured forces in the load cell at the four different displacements can be seen in Table 4-4. The average results of the three experimental measurements are compared against the FEA results using a Young's modulus between 5-6,5 GPa, these results can be seen in Figure 4-18. The modulus was iterated in FEA starting at 6,5 GPa, going down to 5 GPa in 0,5 GPa steps. As can be seen in the figure, the modulus of 5 and 5,5 GPa are the best converging results to the experimental study. As the modulus of both 5 GPa and 5,5 GPa has the best convergence against the experimental results, a modulus of 5,3 GPa was also tested. The modulus of 5,3 GPa was found to have the best correlation against the experimental results. Thus, the Young's modulus of the PA66GF30 is set to 5,3 GPa in the verification of the existing FE simulation methods and during the development of the new method.

Table 4-4: Experimental results in load cell.

Displacement [mm]	Measurement 1: Force [N]	Measurement 2: Force [N]	Measurement 3: Force [N]	Average: Force [N]
0,15	3	3	3	3
0,3	6	5	6	6
2	28	32	29	30
3,2	49	52	50	50
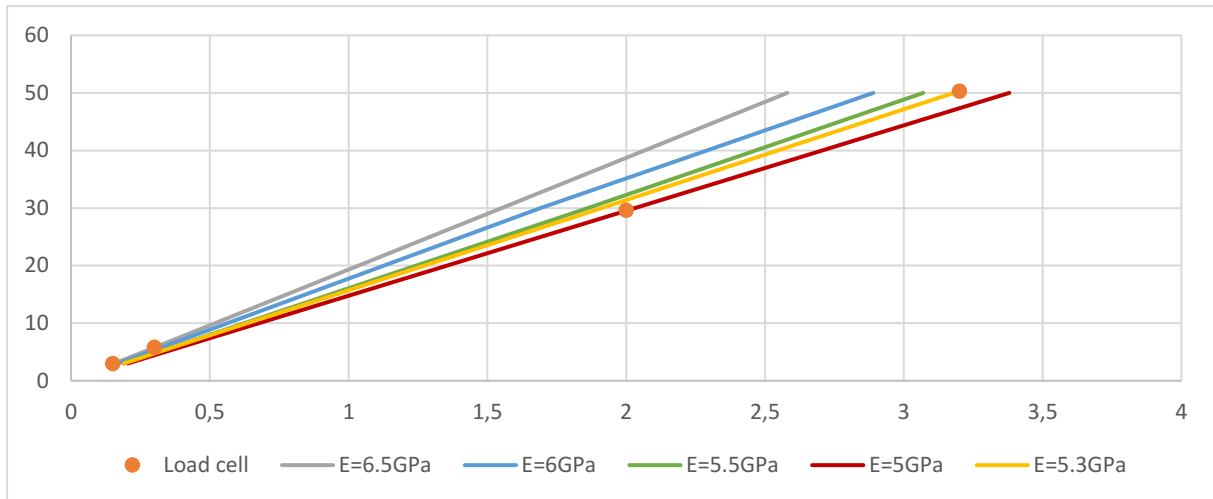
Figure 4-18: Comparison of Young's modulus against experimental results.

4.3 Verification of existing FE simulation methods

The comparison between the numerical and experimental results answers the first thesis question as the margin of error of the existing FE simulation methods can be answered in the areas where the strain measurements have taken place.

4.3.1 Verification of contact A

The comparison of the experimental and numerical stresses of contact A, at 100 kPa can be seen in Figure 4-19 to Figure 4-23. In the figures, it can be seen that the numerical results are only reading approximately 50% of experimentally attained stresses at the outer bottom radii. When the strain gauges were placed on the radiator, they were placed in the centre of the radius, as it was the position of the minimum principal stress in the FE model considering hygroscopy. When the position of the strain gauges was mapped in the FE model, they were connected to their exact position of where they were mounted in the experiment. However, the position in the FE model was not only beneath the area of the minimum principal stresses, but also beneath the centre of the radius where they were mounted in the controlled experiment. Further investigation showed that the geometry of the header in the FE model was slightly different from the actual. The difference in geometry of the header can be seen in Figure 4-24.

At the outer top radii, the numerical stresses are on the other hand multiple times higher than the experimental stresses, except for the stresses at the grill side on the middle section. The difference at this radius is presumably caused by the coarse mesh, which also is presumed to cause the irregular stresses patterns in the other figures.
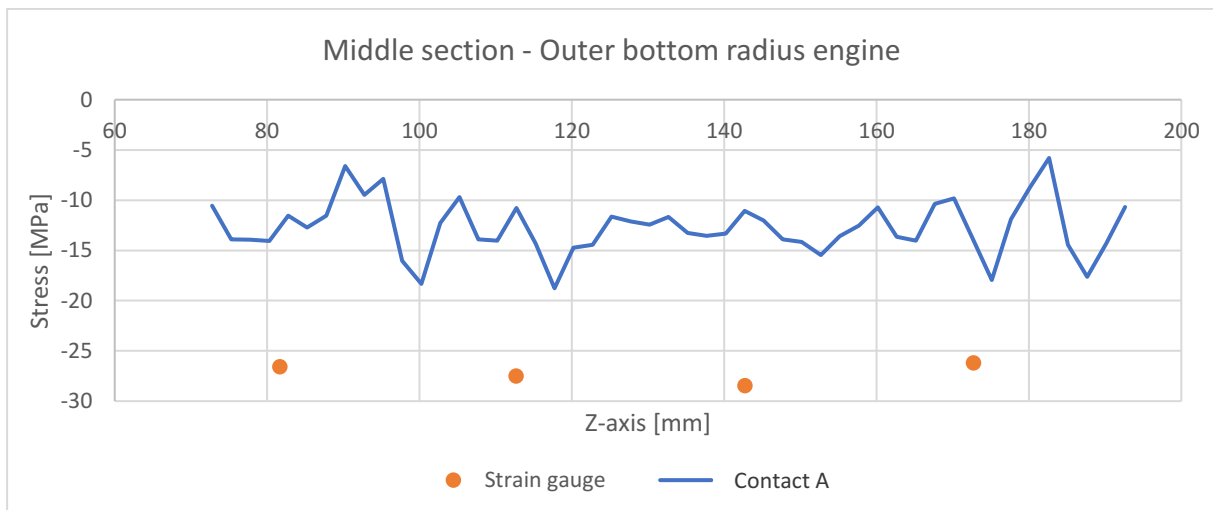
Figure 4-19: Stresses at the outer bottom radii on the middle section.

Figure 4-20: Stresses at the outer bottom radii on the outlet section.

Figure 4-21: Stresses at the outer top radii on the middle section.

Figure 4-22: Stresses at the outer top radii on the outlet section.
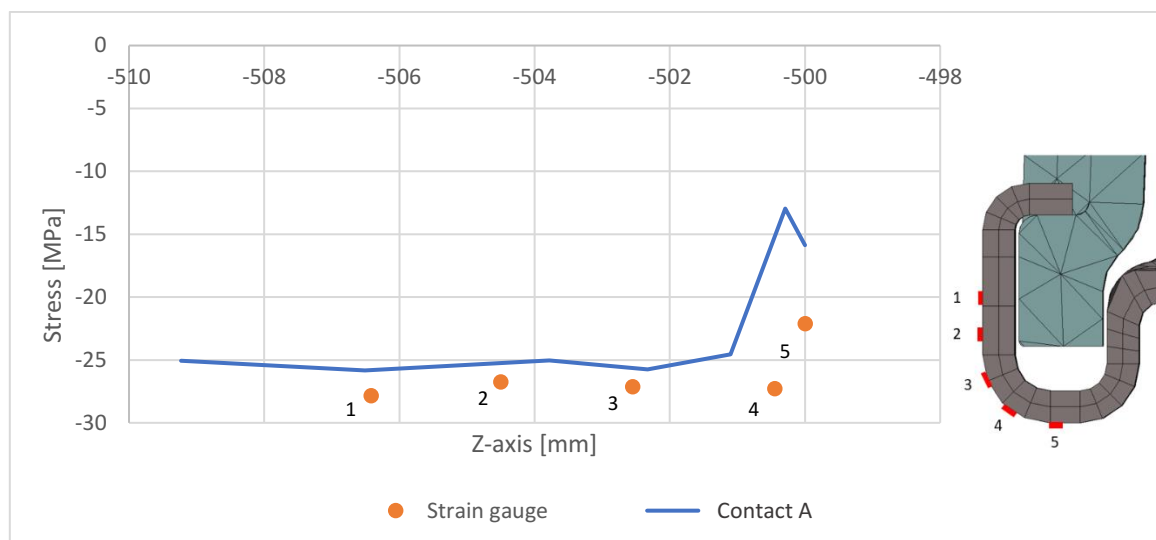
Figure 4-23: Stresses along the header wall and outer bottom radius.

41
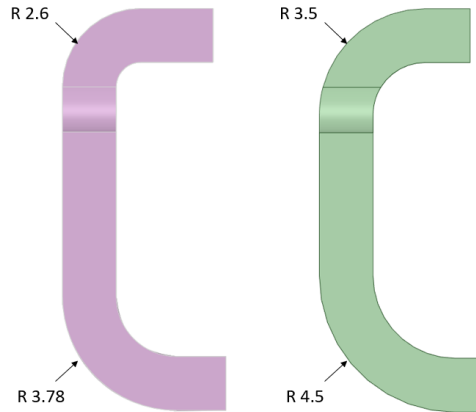
Figure 4-24: Difference in the geometry of FE model (left) and manufactured header (right).

As the geometry of the FE model had to be updated to better represent the actual geometry, the mesh was refined on the header to increase the precision of the FE model. The mesh was therefore set to be constructed of 1 mm hexahedron elements compared to the current 4 mm. To be able to see what difference only the geometry would have on the displacements and stresses, the mesh was updated on the model with the old geometry as well. The results of the refined mesh on the original FE model and the new FE model with the actual geometry can be seen in Figure 4-25 to Figure 4-29. When the mesh is refined, it can be seen that the minimum principal stress at the outer bottom radii has increased and has become more stable, meaning that the existing method of using 4 mm elements on the radiator is too large if the absolute stresses are sought. The change in geometry did not have any significant effect on the stresses in the middle section, but at the outlet section of the radiator, the minimum principal stresses were increased, meaning that the geometry of the model is essential to be correct due to it being the area of failure as described in chapter 1.1.1.
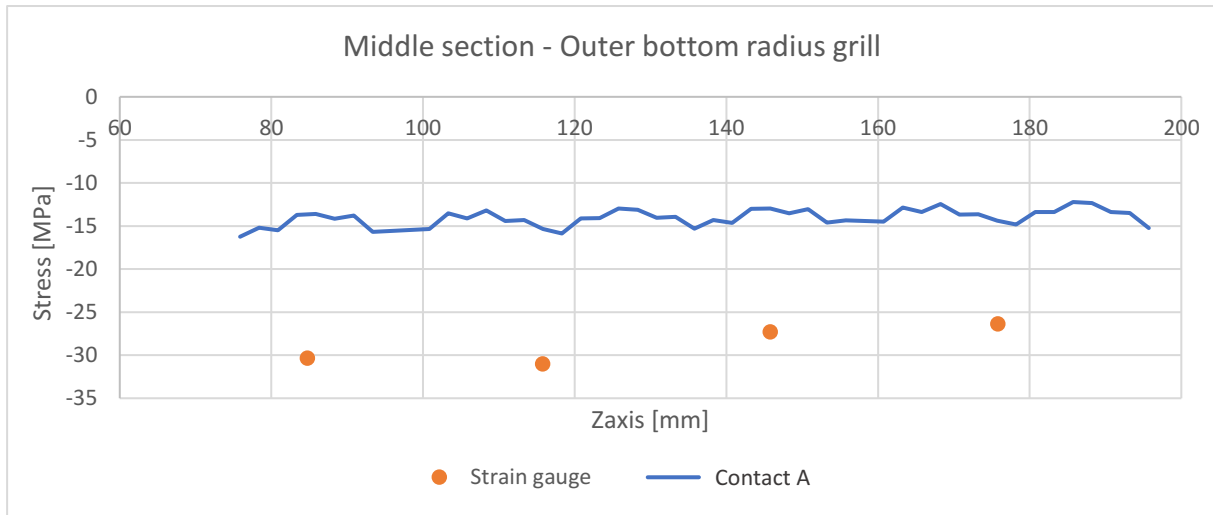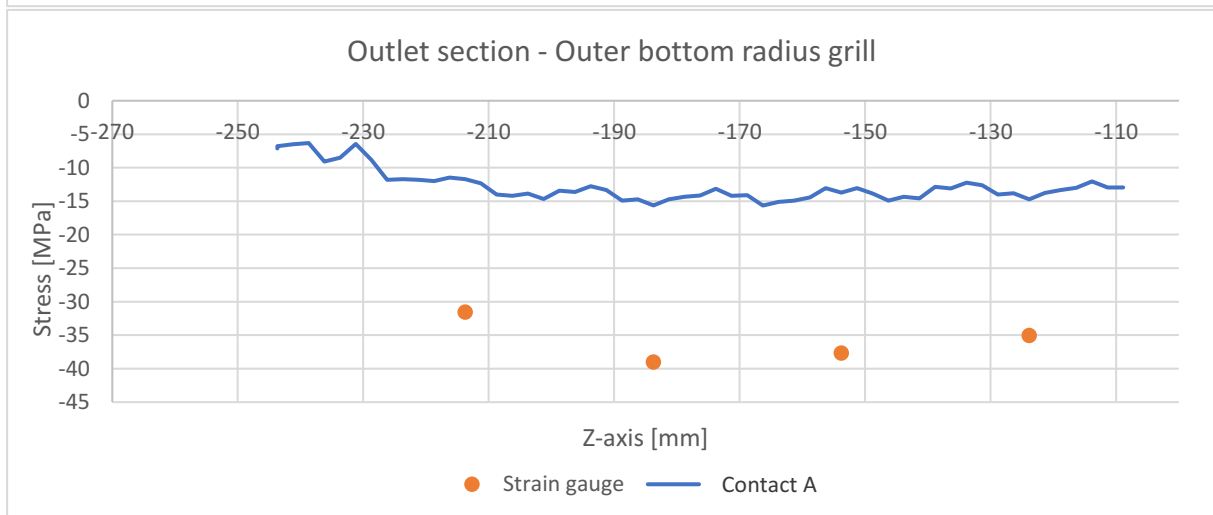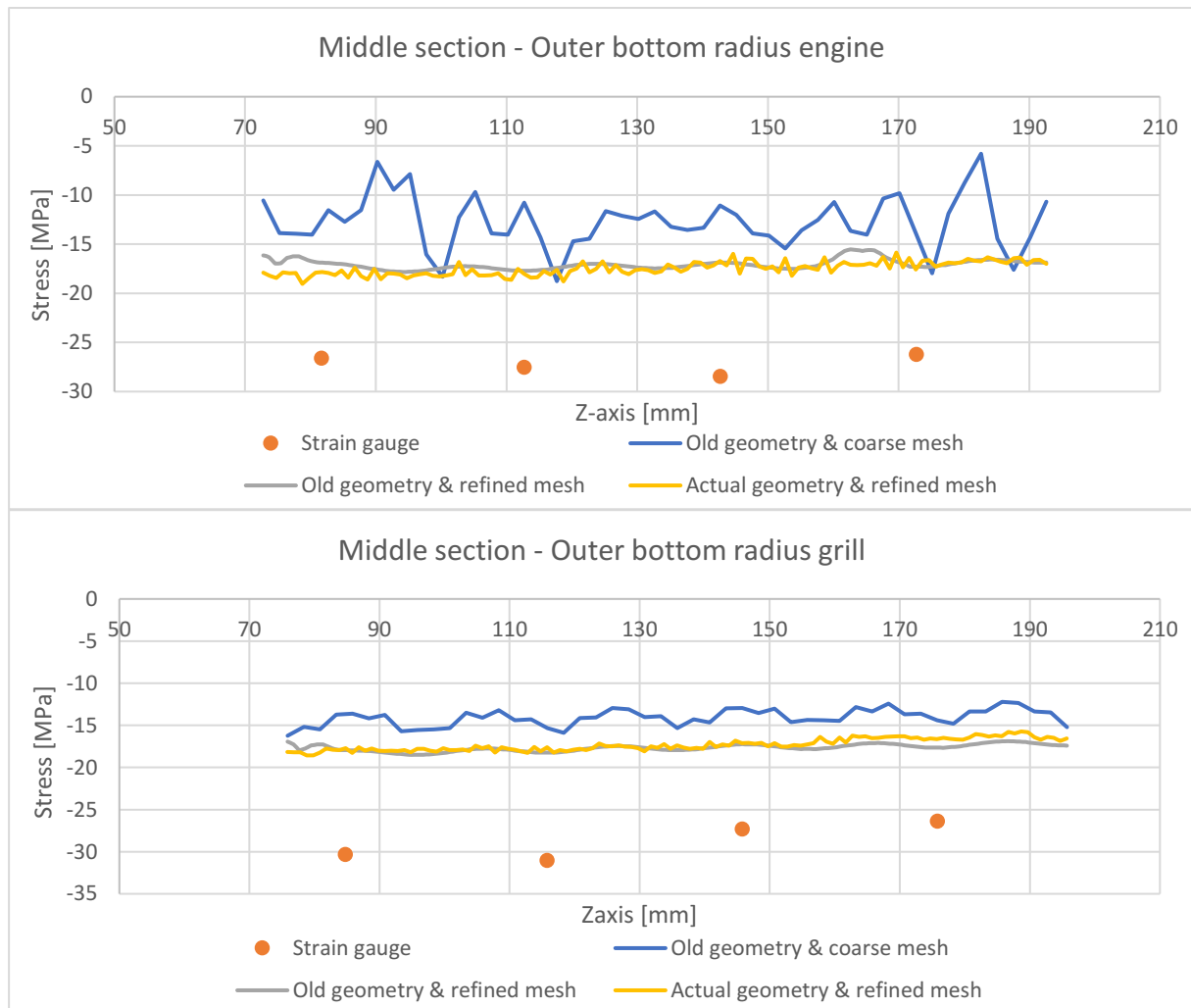
Figure 4-25: Stresses at the outer bottom radii on the middle section.

Figure 4-26: Stresses at the outer bottom radii on the outlet section.

The refined mesh also results in a drop of the stresses at the top radii, a position where the original FE model was reading increased stress improperly, as can be seen in Figure 4-27 and Figure 4-28. The lower stresses of the old geometry with the coarse mesh at the outer top radius on the grill side is found to increase when the mesh is refined. The deviation at this section was therefore caused by the coarse mesh. Even though the measured stresses are low and not interesting to analyse out of a fatigue perspective, having a simulation method that reads these stresses incorrectly is an indication that the method is not representing the structural mechanics of the crimp joint correctly. Even though the refined mesh solved the problem of analysing improper stresses to a certain extent, the updated geometry represents the stresses better. As the radius is larger on the header tab, the stresses are distributed better over the radius.
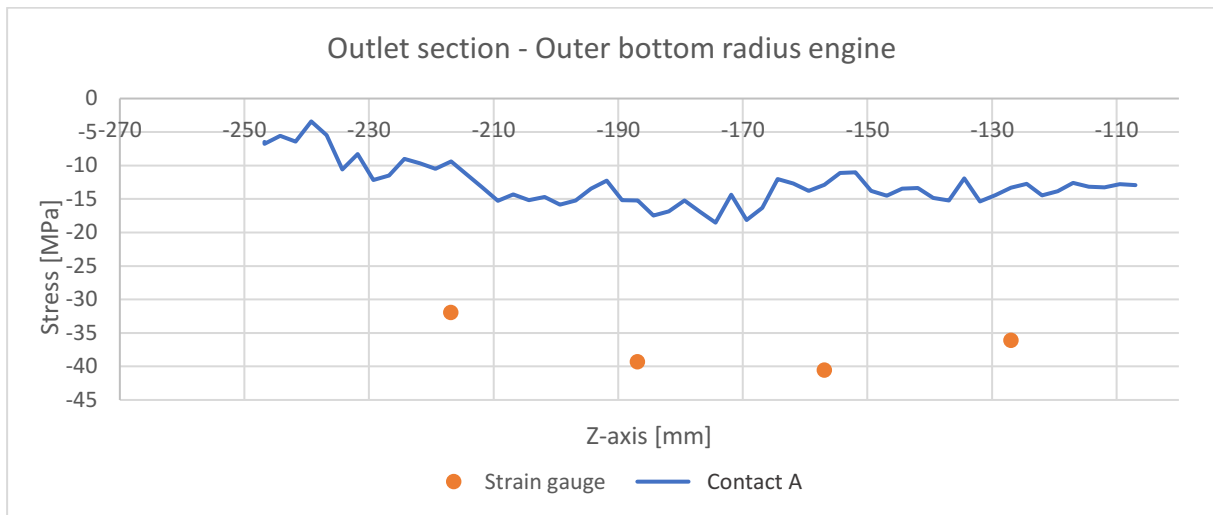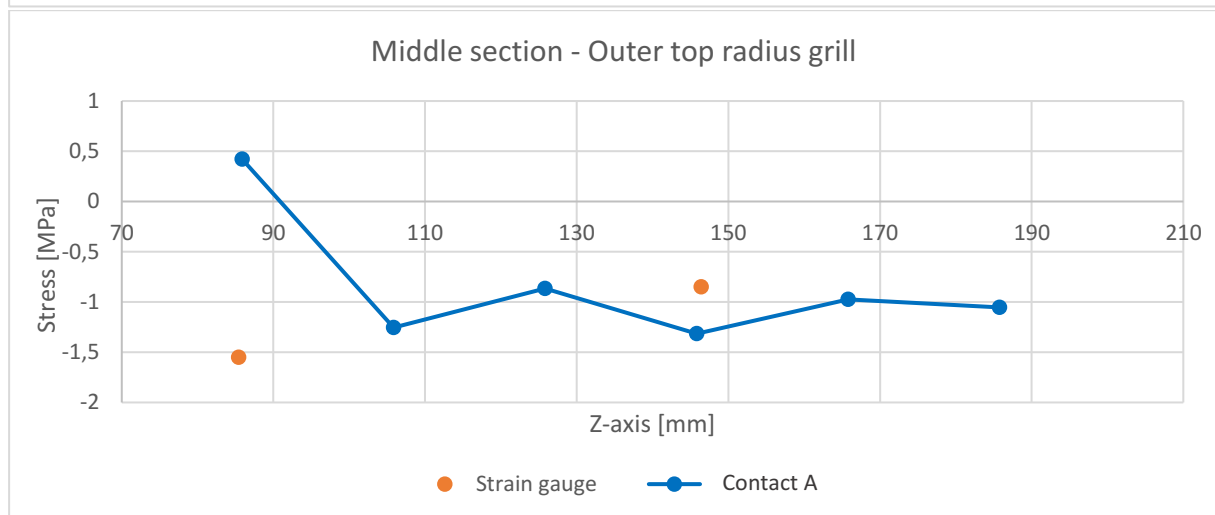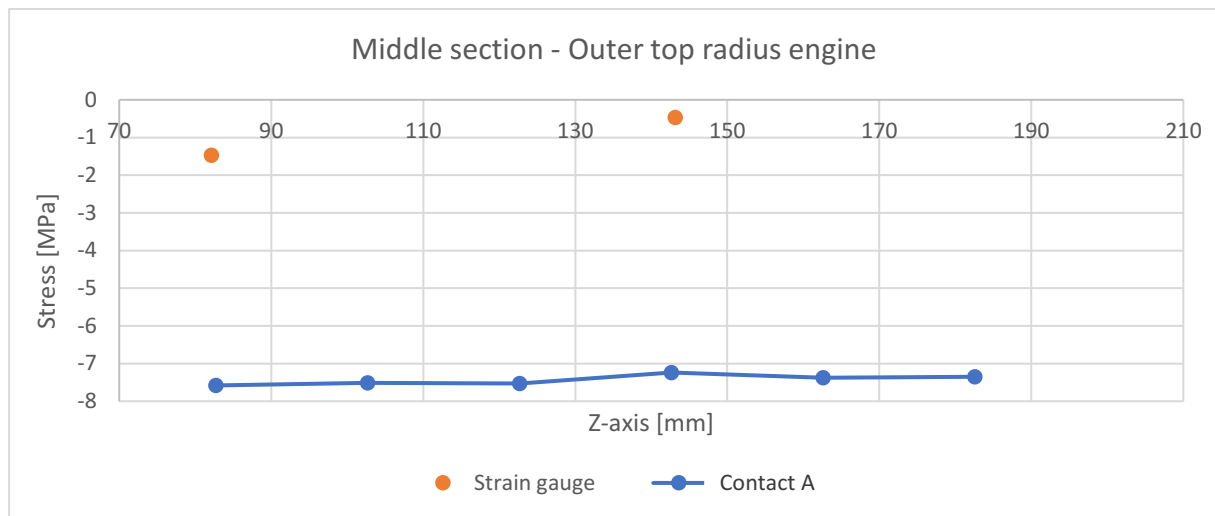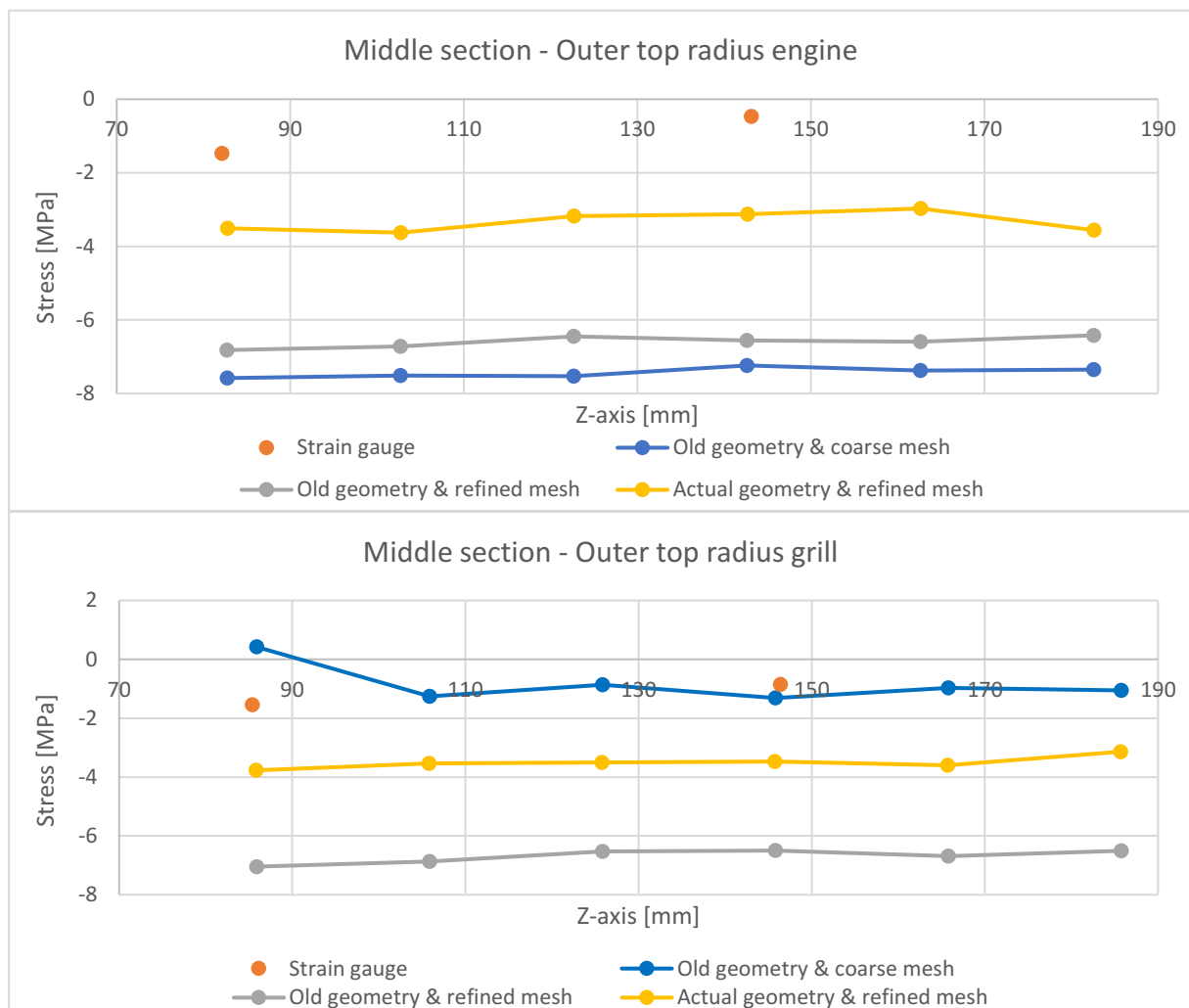
Figure 4-27: Stresses at the outer top radii on the middle section.
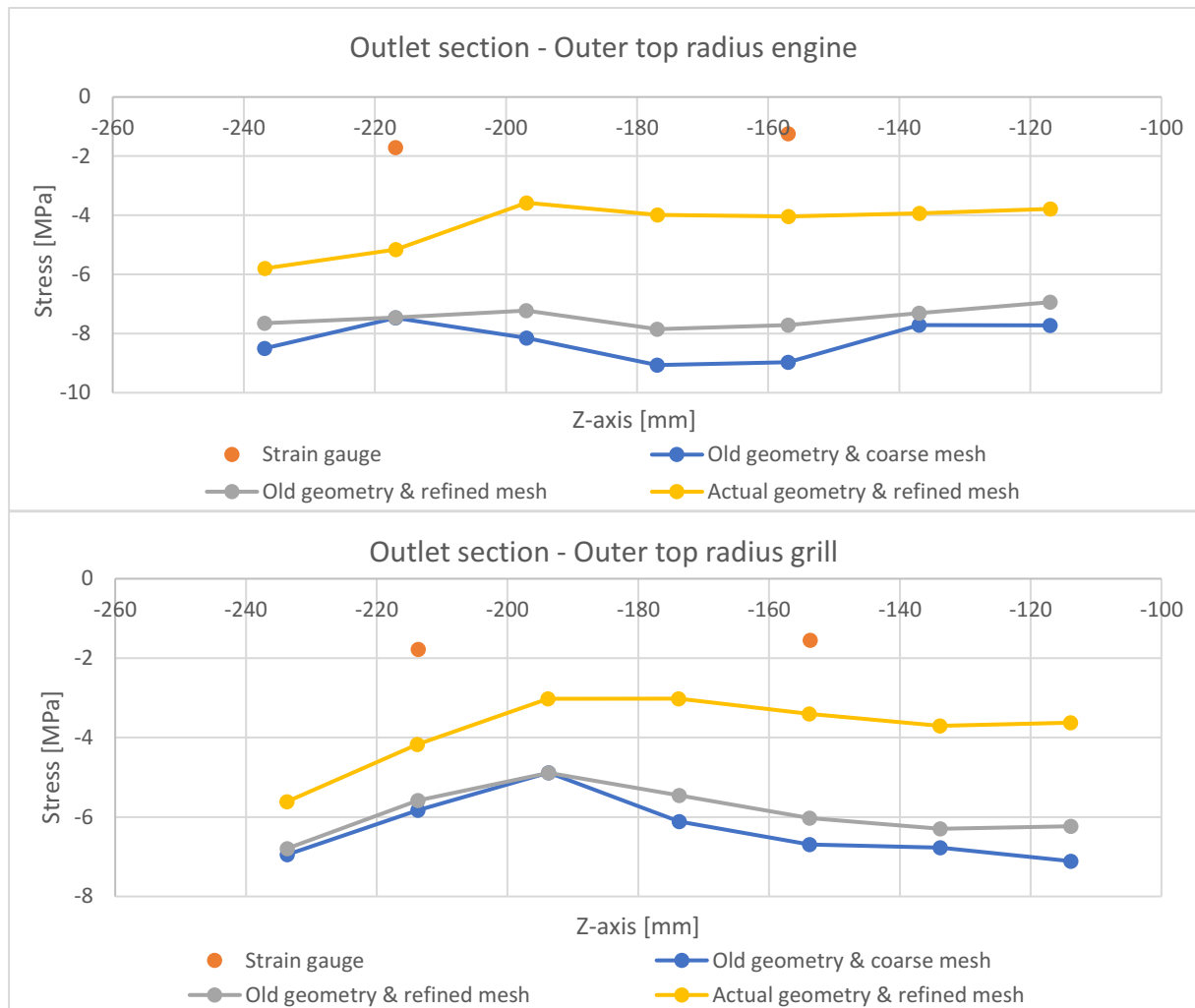
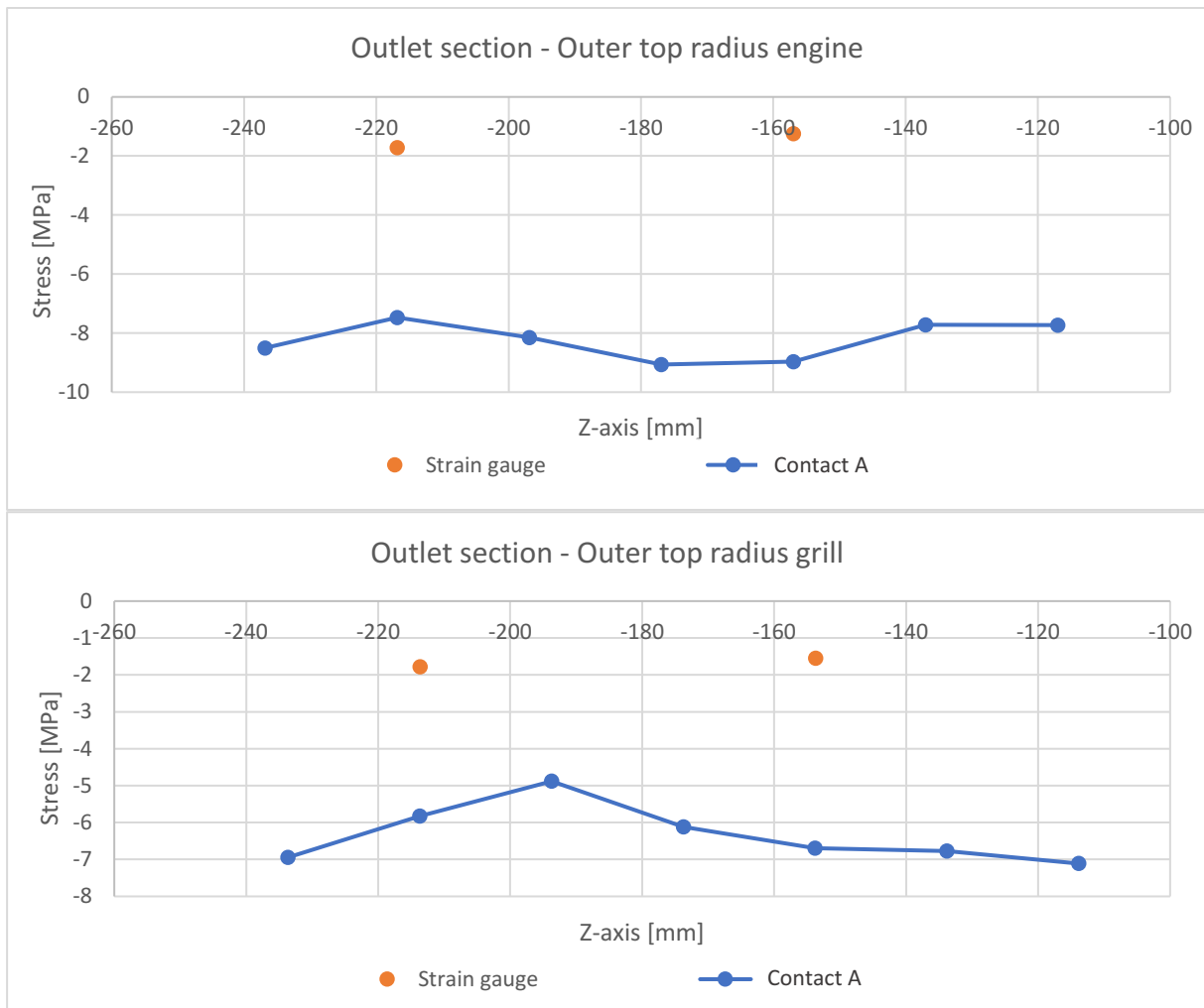Figure 4-28: Stresses at the outer top radii on the outlet section.

When the mesh was refined, the behaviour of the measured stresses at the 5-grid strain gauge changed. The stresses are now distributed over the outer bottom radius, lowering the stresses around the bottom of the header wall and radius. This distribution of the stress in the numerical results is not the same as the experimental, indicating that the current method is not representing the crimp joint sufficiently.
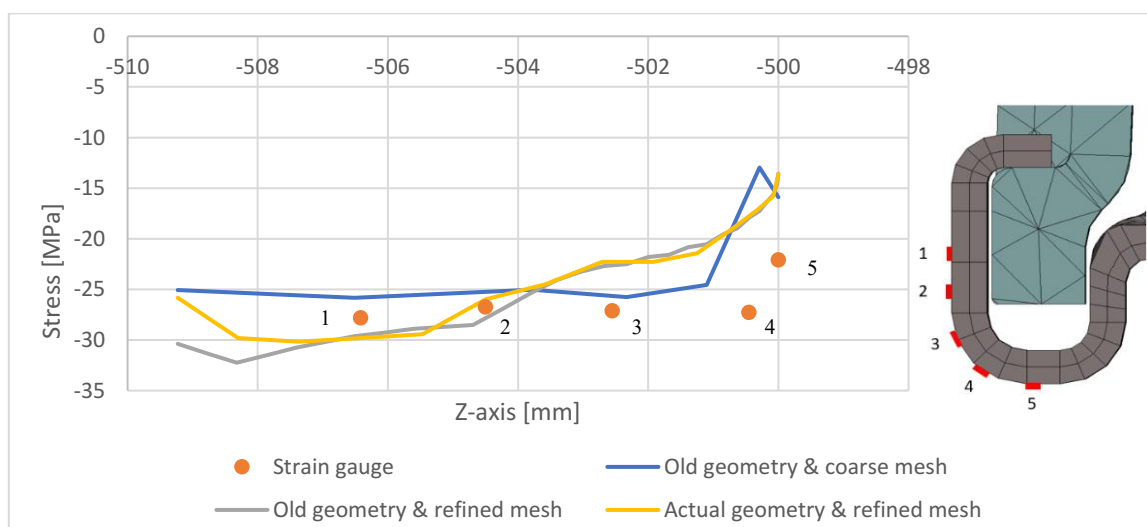
Figure 4-29: Stresses along the header wall and outer bottom radius.

To summarise the margin of error of the absolute stresses in the original FE model, the experimental stresses are compared between the strain gauges and the node in the position of the strain gauge, these are summarised in Table 4-5. The overview of the instrumentation can be seen in Appendix A. The original FE model is not sufficiently representing the crimp joint when the absolute stresses are sought, due to the margin of error reaching over 70% at the outer bottom radius. Even though there is a clear change when changing the sizing of the mesh and the geometry, the method of representing the crimp joint according to contact A is insufficient as the margin of error still reaches 55% at the outer bottom radius. The change of the refined mesh lowered the average margin of error of 7,1%, and the new geometry lowered it an additional 4,2%.

Table 4-5: Margin of error of contact A at the outer bottom radius and header wall.

Name	Old geometry & coarse mesh	Old geometry & refined mesh	Actual geometry & refined mesh
SG03_ORE_3	70,6%	62,9%	40,9%
SG04_ORE_4.5	61,3%	64,0%	43,1%
SG05_ORE_6	68,3%	58,7%	49,6%
SG06_ORE_7.5	63,2%	51,3%	47,5%
SG09_ORG_3	62,9%	61,3%	50,2%
SG10_ORG_4.5	60,0%	63,2%	53,5%
SG11_ORG_6	63,6%	62,6%	54,1%
SG12_ORG_7.5	57,9%	53,0%	51,7%
SG15_ORE_18	56,6%	36,5%	32,9%
SG16_ORE_19.5	60,8%	35,6%	34,5%
SG17_ORE_21	61,1%	40,7%	41,2%
SG18_ORE_22.5	47,1%	34,0%	32,9%
SG21_ORG_18	55,1%	40,8%	41,6%
SG22_ORG_19.5	50,5%	41,2%	43,2%
SG23_ORG_21.1	28,1%	38,6%	38,4%
SG24_ORG_21.2	52,5%	34,3%	37,2%
SG25_ORG_21.3	5,1%	16,4%	17,8%
SG26_ORG_21.4	6,4%	-6,6%	2,9%
SG27_ORG_21.5	7,2%	-6,4%	-7,1%
SG28_ORG_22.5	45,4%	33,1%	36,9%
Average	**49,2%**	**42,1%**	**37,9%**

SGXX_AAB_YY.Y
SG = Strain gauge
XX = strain gauge number
AA = position of strain gauge: OR = outer bottom radius, TR = outer top radius
B = side of radiator: E = engine side, G = grill side
YY.Y = header tab number

The comparison of the experimental and numerical displacements at 100 kPa can be seen in Figure 4-30, Figure 4-31, and Appendix C. The result from the numerical analysis shows that the current simulation method is in general too stiff compared to the experimentally attained results. However, the displacement at the tank wall on the middle section forms somewhat of an exception, where the displacements of the FE model is overlapping the experimental results. The change in sizing of mesh and geometry had only minor effects on the displacements. The displacements of the crimp joint are on the other hand heavily influenced by the method of representing the crimp joint in the FE model as well, meaning that the existing method is not representing the crimp joint sufficiently when studying the displacements either.
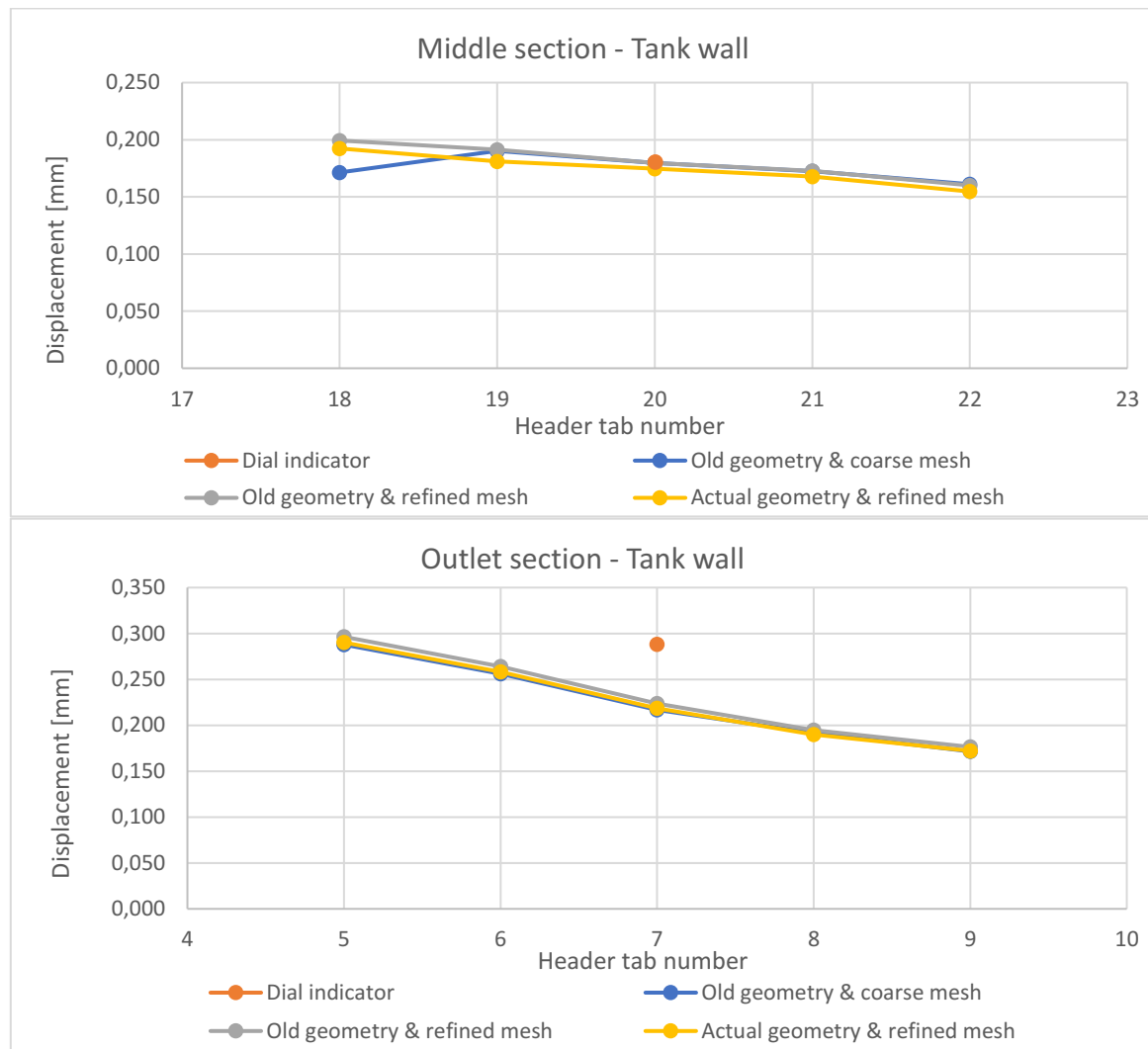
Figure 4-30: Displacement at the tank wall.
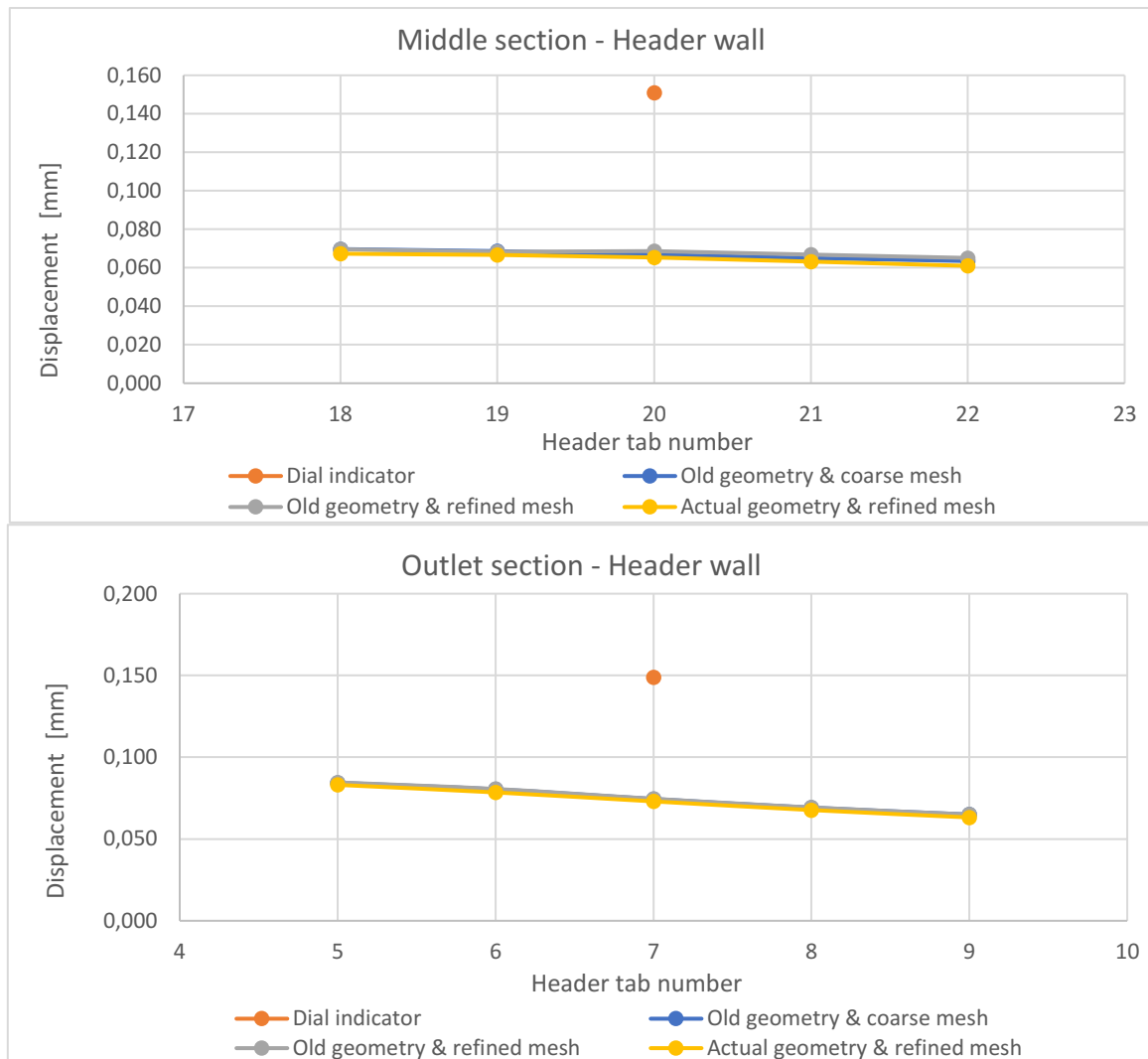
Figure 4-31: Displacement at the header wall.

4.3.2 Verification of contact B and C

The comparison of the three methods that are used by the corporate partner, with the updated geometry and refined mesh, can be seen in Figure 4-32 to Figure 4-36. When studying the stresses along the header wall and outer bottom radius, it can be seen that the increased minimum principal stresses are not only located at the header wall with contact B and C. The methods are instead reading a more evenly distributed stress at the outer bottom radius where the highest minimum principal stresses are located in the centre of the radius, similar to the experimental results. Thus, both contact B and C are representing the structural mechanics of the crimp joint better than contact A, but both methods are reading too high minimum principal stresses over the header wall and outer bottom radius. The same behaviour can be seen when studying the stresses at the outer bottom radius in the middle section of the radiator, where both methods are reading too high minimum principal stresses.
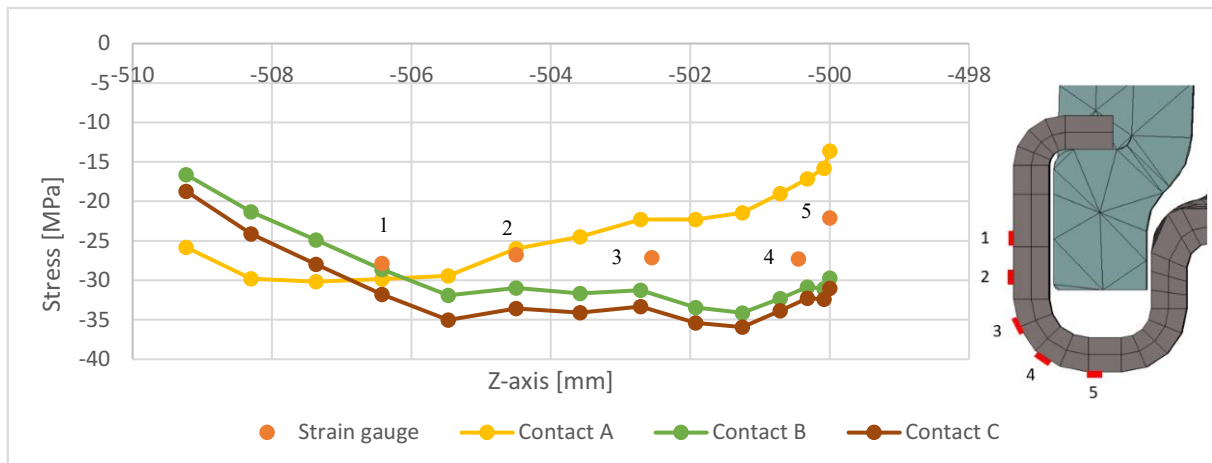
Figure 4-32: Stresses along the header wall and outer bottom radius.

Figure 4-33: Stresses located at the outer bottom radius on the middle section.

When studying the stresses located on the outer bottom radius at the outlet section in Figure 4-34, contact C has a good correlation against the experimental results. Contact B is on the other hand reading too low stresses.
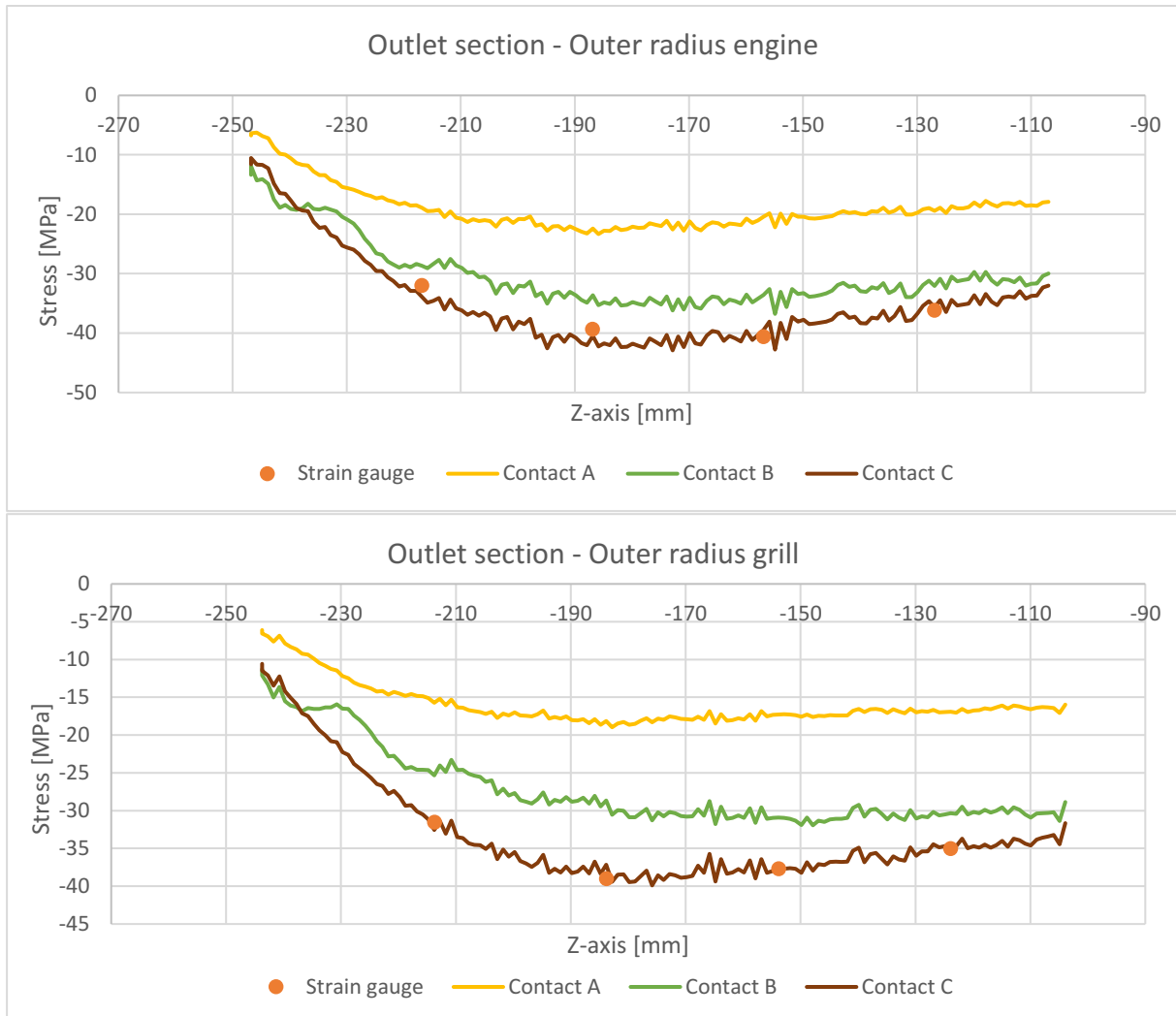
Figure 4-34: Stresses located at the outer bottom radius on the outlet section.

When studying the stresses at the outer top radius of the crimp joint, it can be seen that all three methods are representing the stresses fairly well. The experimental stresses are close to non-existent, meaning that the stresses from the numerical analysis should only be in somewhat the same order of magnitude.
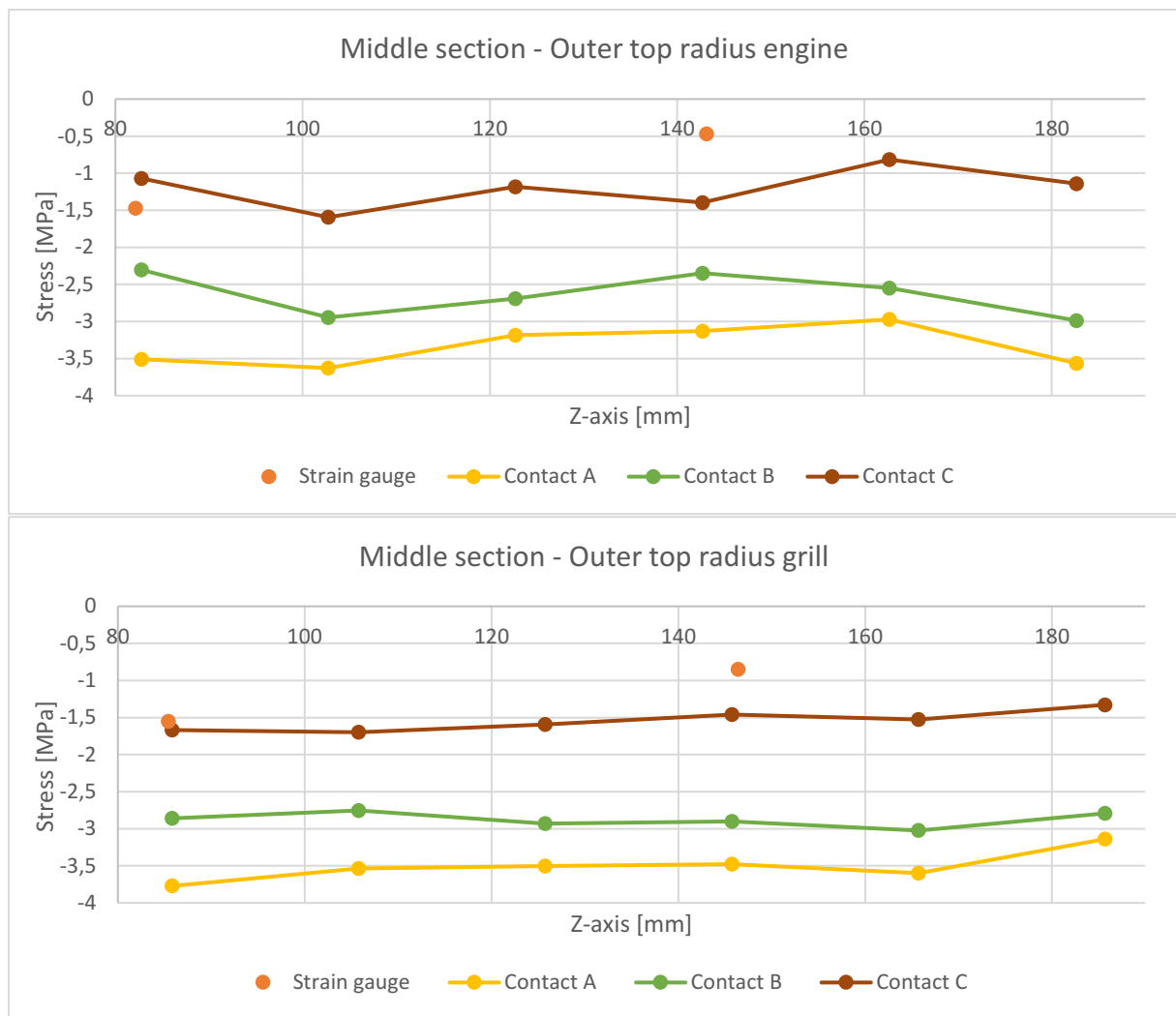
Figure 4-35: Stresses located at the outer top radius on the middle section.
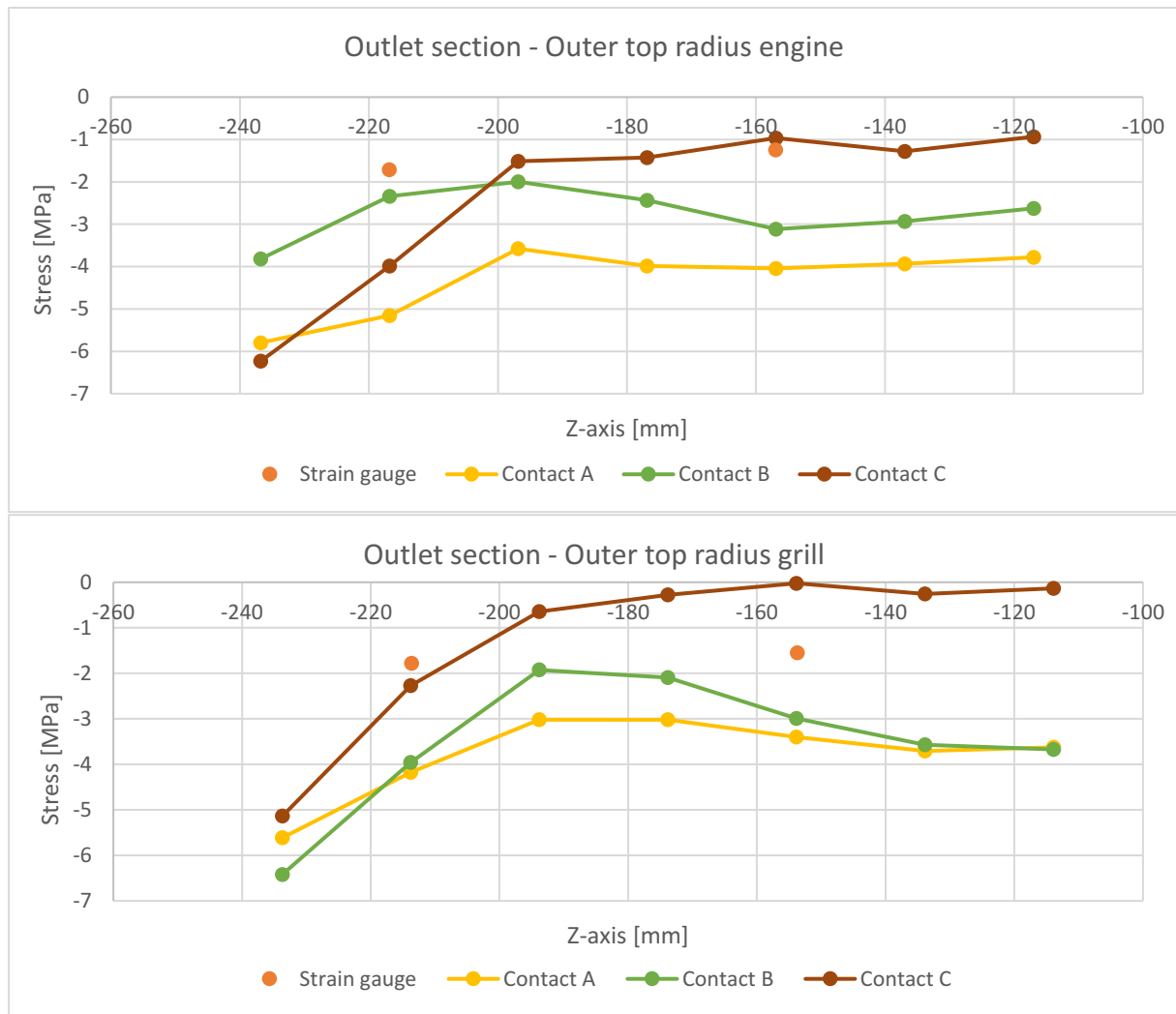
Figure 4-36: Stresses located at the outer top radius on the outlet section.

The margin of error of the existing simulation methods can be seen in Table 4-6 and the overview of the instrumentation can be seen in Appendix A. As can be seen in the table, contact B and C have a substantially lower margin of error compared to contact A. Contact C has a margin of error below 7% at the outer bottom radius of the outlet section and is seen as a sufficient simulation method for this section. However, the method reads too high stresses at the middle section, with an error of up to 25%, whereas the average margin of error is 11,5%. Contact B has the lowest margin of error on the outer bottom radius and along the header wall of the middle section, with an error under 16%. However, at the outlet section, the margin of error reaches over 25%, making it insufficient at the area of the highest minimum principal stresses of the radiator.

Table 4-6: Margin of error of existing simulation methods at the outer bottom radius and header wall.

Name	Contact A	Contact B	Contact C
SG03_ORE_3	40,9%	10,3%	-6,2%
SG04_ORE_4.5	43,1%	14,4%	-2,9%
SG05_ORE_6	49,6%	17,1%	2,6%
SG06_ORE_7.5	47,5%	13,7%	4,1%
SG09_ORG_3	50,2%	19,7%	-3,2%
SG10_ORG_4.5	53,5%	26,5%	4,7%
SG11_ORG_6	54,1%	17,9%	-0,4%
SG12_ORG_7.5	51,7%	13,4%	1,4%
SG15_ORE_18	32,9%	-15,0%	-23,4%
SG16_ORE_19.5	34,5%	-8,4%	-13,6%
SG17_ORE_21	41,2%	-0,7%	-7,7%
SG18_ORE_22.5	32,9%	-11,5%	-17,4%
SG21_ORG_18	41,6%	-7,4%	-11,4%
SG22_ORG_19.5	43,2%	1,3%	-0,9%
SG23_ORG_21.1	38,4%	-34,5%	-40,3%
SG24_ORG_21.2	37,2%	-13,1%	-18,2%
SG25_ORG_21.3	17,8%	-15,3%	-22,8%
SG26_ORG_21.4	2,9%	-15,8%	-25,5%
SG27_ORG_21.5	-7,1%	-2,8%	-14,2%
SG28_ORG_22.5	36,9%	-10,0%	-13,6%
Average	**37,9%**	**13,4%**	**11,5%**
SGXX_AAB_YY.Y SG = Strain gauge XX = strain gauge number AA = position of strain gauge: OR = outer bottom radius, TR = outer top radius B = side of radiator: E = engine side, G = grill side YY.Y = header tab number			

The comparison of the displacements at the header wall and tank wall can be seen in Figure 4-37 and Figure 4-38. The comparison of the displacements at the header tabs and tank tops can be seen in Appendix D. It can here be found that the two other methods are in general a better representation of the crimp joint compared to contact A. The only area where contact A is better, is at the tank wall on the middle section.
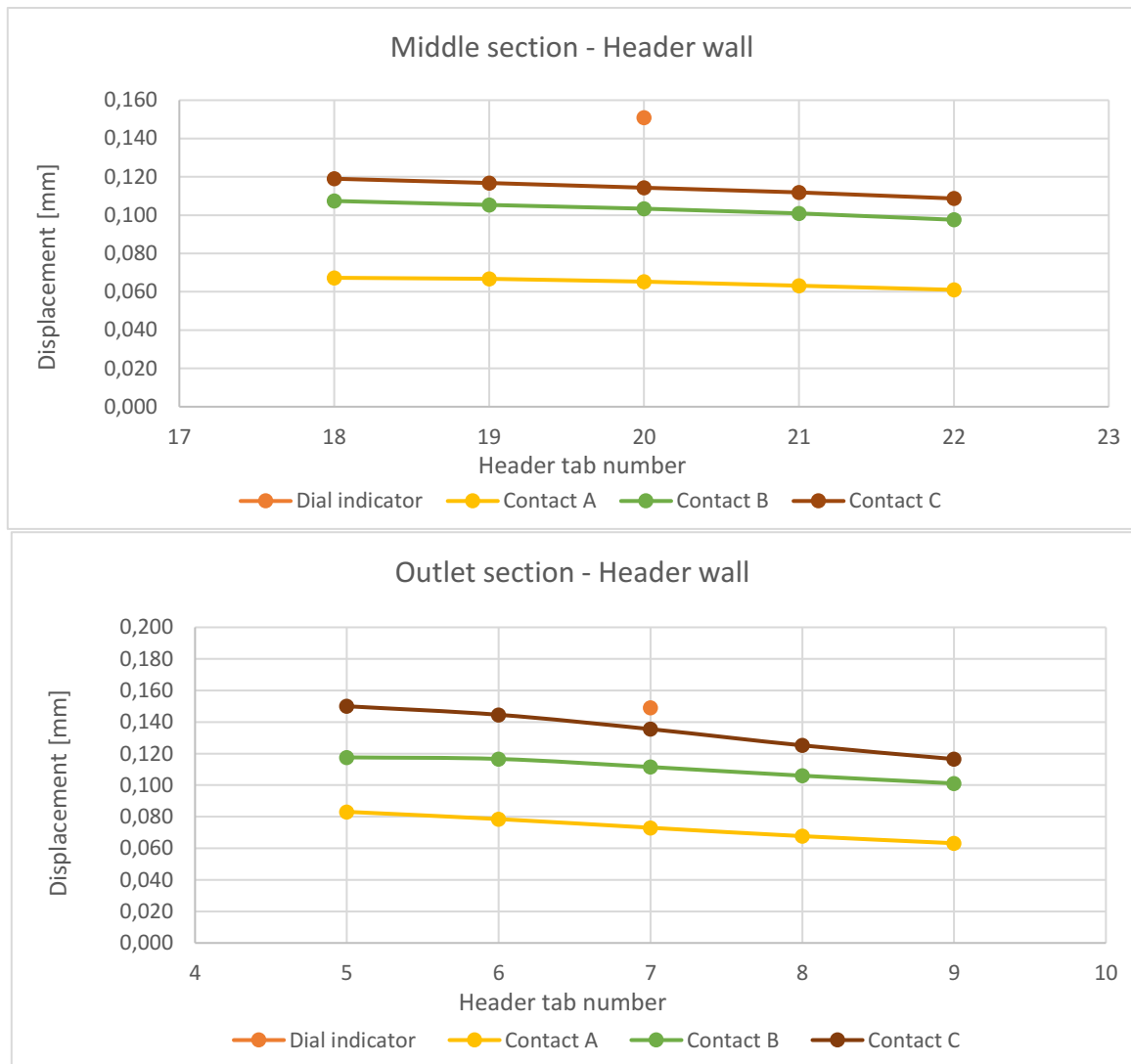
Figure 4-37: Displacements at the header wall.
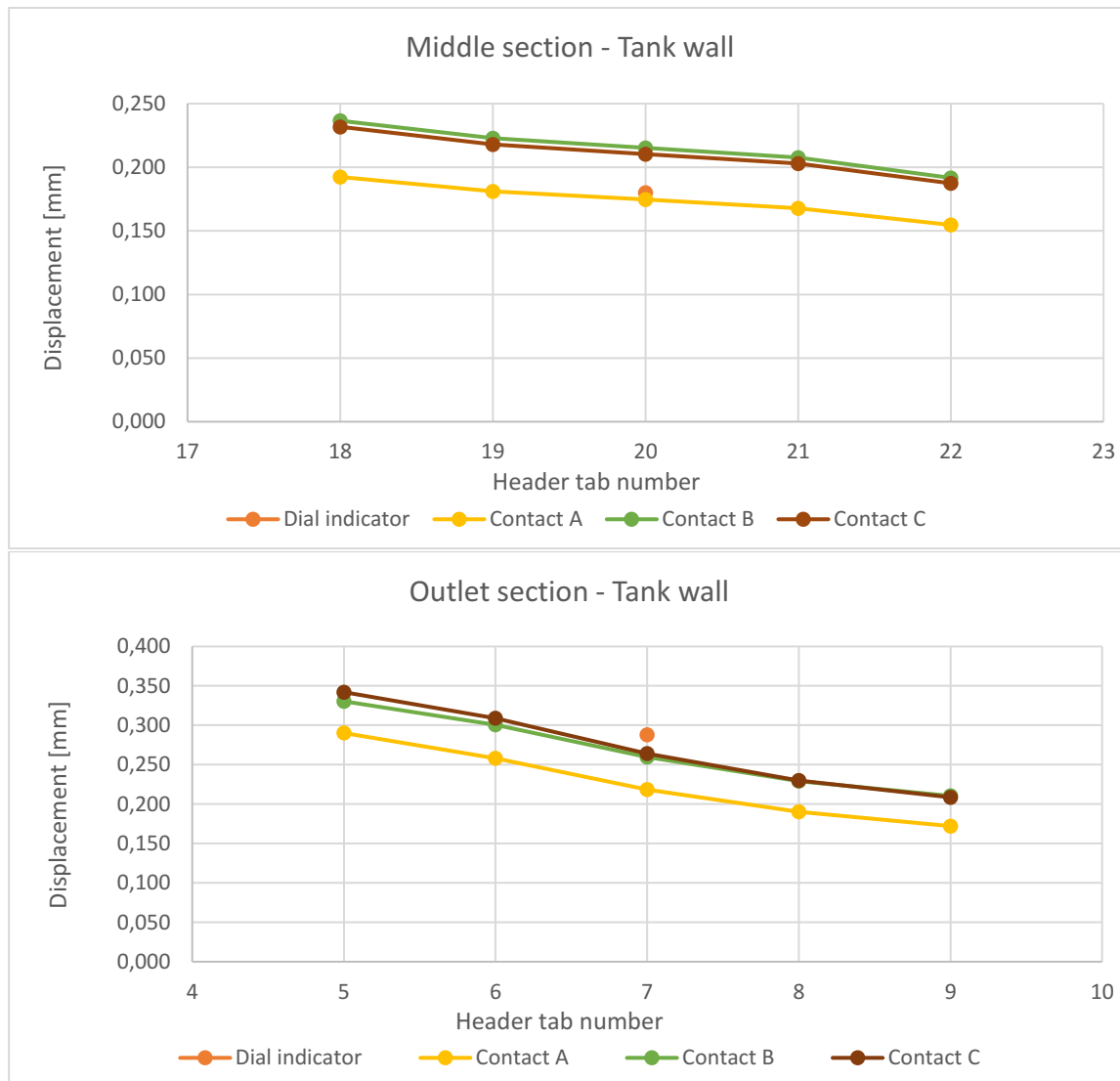
Figure 4-38: Displacement at tank wall

4.4   Development of FE simulation method

The comparison between the numerical results of the new method and the experimental results answer the second thesis question as the margin of error of the newly developed FE simulation method of the crimp joint can be determined.

4.4.1   Correlation of submodels

The results from the stress correlation between the global model and the submodel can be seen in Figure 4-39 to Figure 4-41. The stresses along the outer bottom radius of the crimp joint have a good correlation between the two models in the centre of the submodel. The edges of the submodel are subjected to some stress concentrations in the cut, thus the stresses in the edges of the submodel will be neglected during the development of the new simulation method. The stresses are slightly lower in the submodel at the outer bottom radius and at the position of the 5-grid strain gauge, but as contact B is used as a benchmark, the lower stresses will not affect the development in the submodel. The stresses at the outer top radius do not correlate between the FE models, thus the development in the submodel will not include a comparison in this radius.
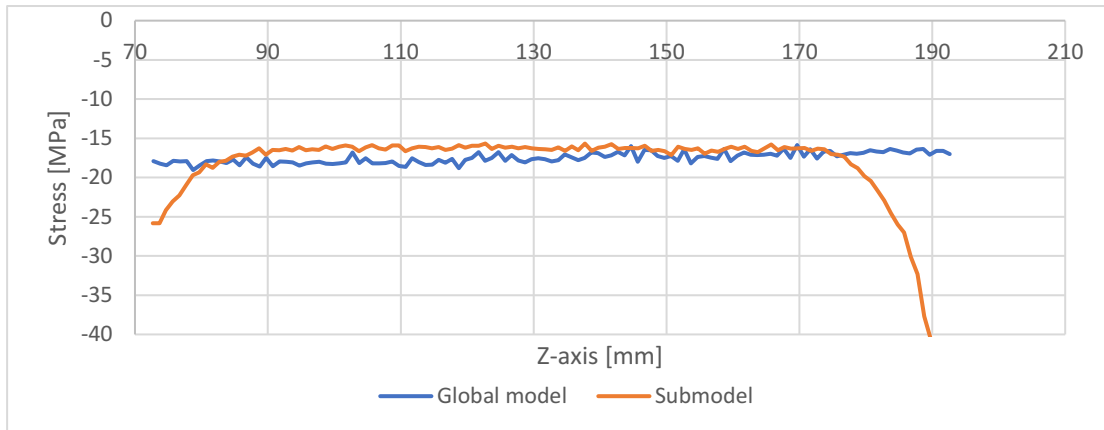
Figure 4-39: Stress correlation of submodel at the outer bottom radius on the engine side.
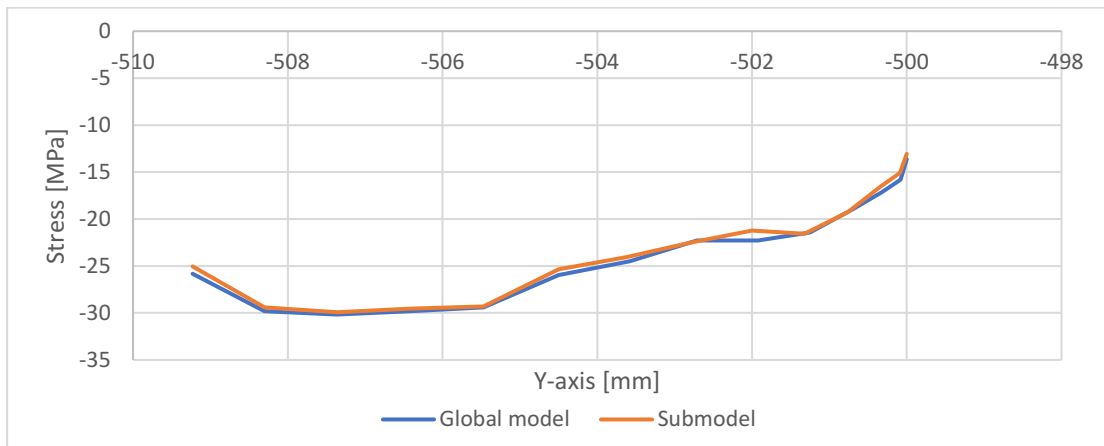
Figure 4-40: Stress correlation of submodel along the header wall and outer bottom radius.
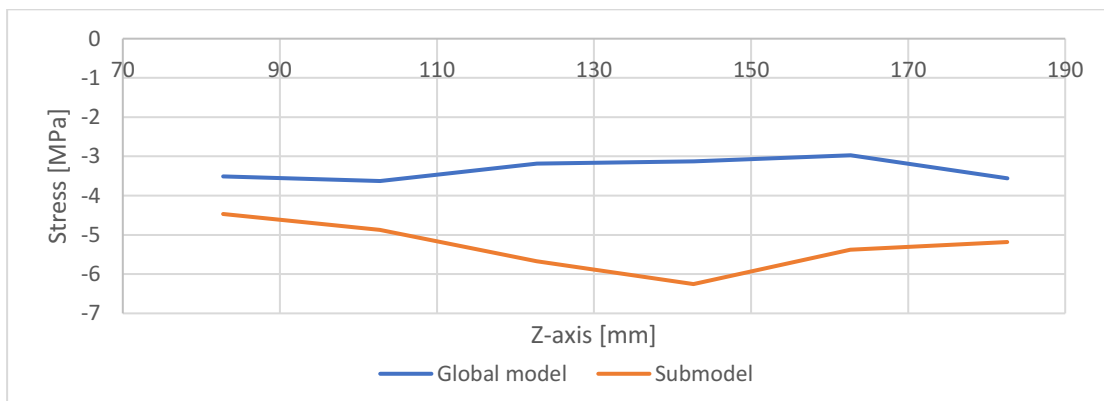
Figure 4-41: Stress correlation of submodel at the outer top radius on the engine side.

As the experimental results of the measured displacements are unreliable at the header tabs and tank tops, the case study will only analyse the displacements of the header wall and tank wall to speed up the process. The results from the displacement correlation between the global model and the submodel can be seen in Figure 4-42 and Figure 4-43. The displacements measured at each row of header tabs are found to have a good correlation between both models, even though the submodel reads slightly too high displacements. There is an increase of the displacements located at the 18:th header tab on the header wall in the submodel, thus the comparison at this header tab will be neglected.
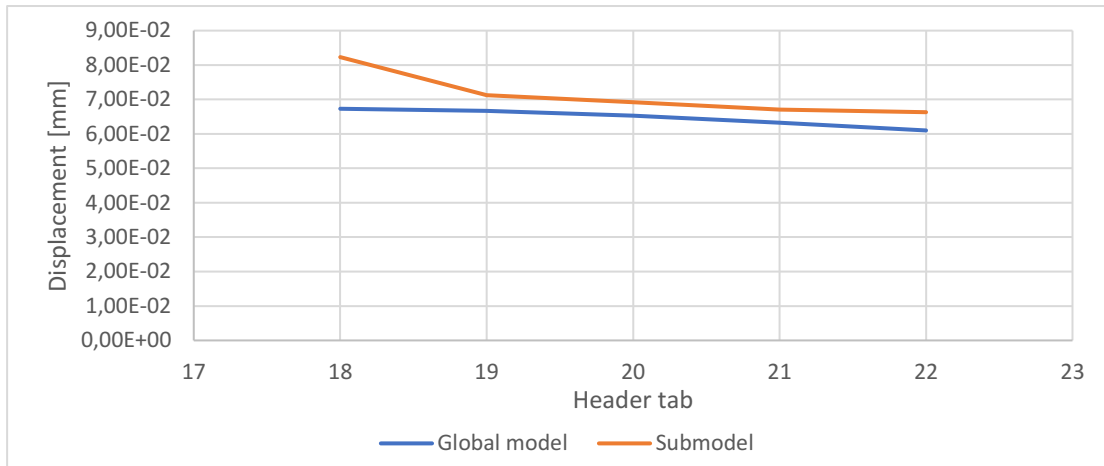
Figure 4-42: Correlation of displacement of submodel at the header wall.
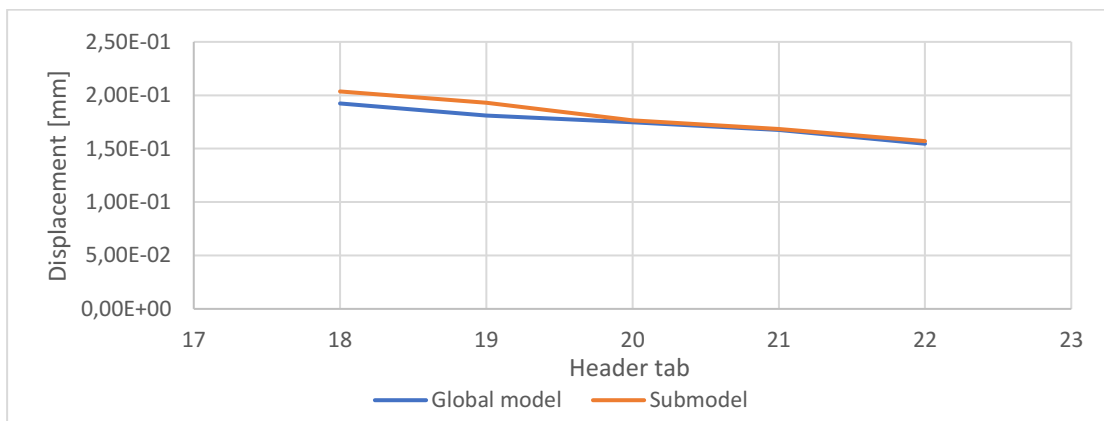
Figure 4-43: Correlation of displacement of submodel at tank wall.

4.4.2 Case study in submodel

The outcome of the case study can be found in Figure 4-44 to Figure 4-47. When studying the stresses at the outer bottom radius of the crimp joint, the contacts 1, 2, 5, 6, 7, 9, 10, 12 and 14 are found to have similar stresses as contact B. The other contacts are therefore sifted out of the collection when continuing to study the stresses located along the header wall and radius. From the experimental results in Figure 4-23, the stresses of the first, third and fourth strain gauge are found to be approximately equal. Thus, the contacts are evaluated after their behaviour in Figure 4-45, here is contact 2 found to have an incorrect behaviour compared to the experimental results and is therefore sifted out as well.

Figure 4-44: Case study of stresses located at the outer bottom radius of the engine side.
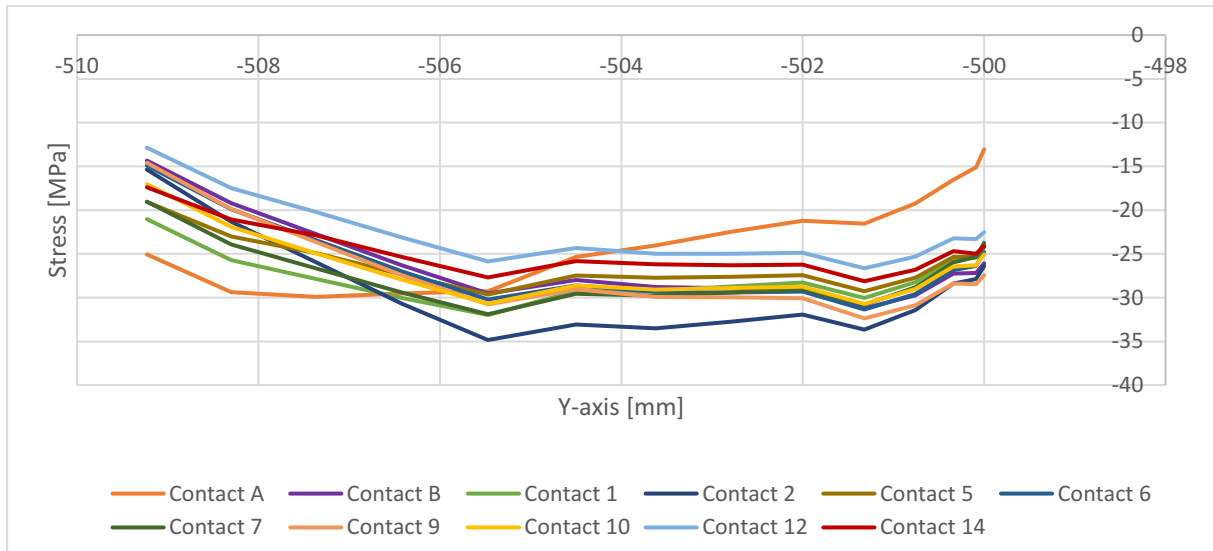
Figure 4-45: Case study of stresses located along the header wall and outer bottom radius.

Therefore, contact 1, 5, 6, 7, 9, 10, 12, and 14 are the only contacts seen as interesting when continuing to study the displacements in Figure 4-46 and Figure 4-47. Here are all contacts found to have a similar displacement as the benchmark of contact B. Contact 6 is even completely overlapping contact B in the displacements at the tank wall, which can be due to the similarity of the two contacts. All the remaining contacts after the sifting, are therefore seen as interesting from the case study in the submodel and will therefore be implemented in the global model.
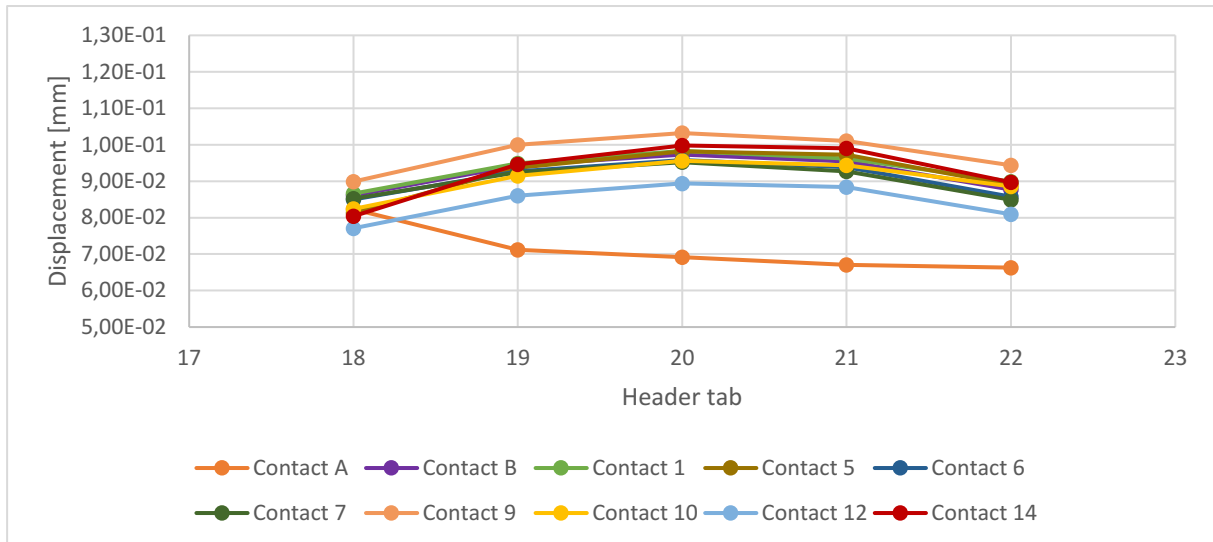
Figure 4-46: Case study of displacements located at the header wall.
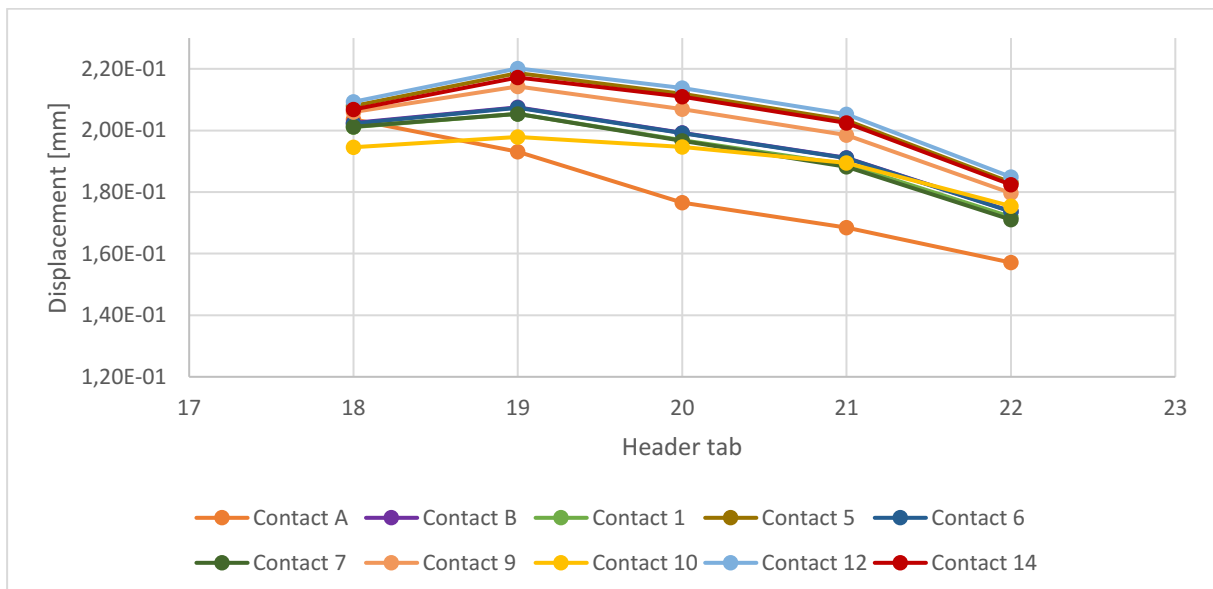
Figure 4-47: Case study of displacements located at the tank wall.

4.4.3   Case study in global model

The outcome of the case study in the global model can be seen in Figure 4-48 to Figure 4-51. Here it can be found that all the tested contacts have a relatively good correlation against the experimental results when studying the outer bottom radius on the engine side of the middle section. It can here be seen that only contacts 1, 5, 9, and 12 were tested in the global model. However, out of the tested methods are contact 1 and 12 found to have the best correlation in this area. When studying the stresses located at the outer bottom radius on the engine side of the outlet section, it can be found that contact 1 and 9 are reading too low stresses. As these are insufficiently representing the crimp joint at low pressure in this area, they are sifted out of the selection.
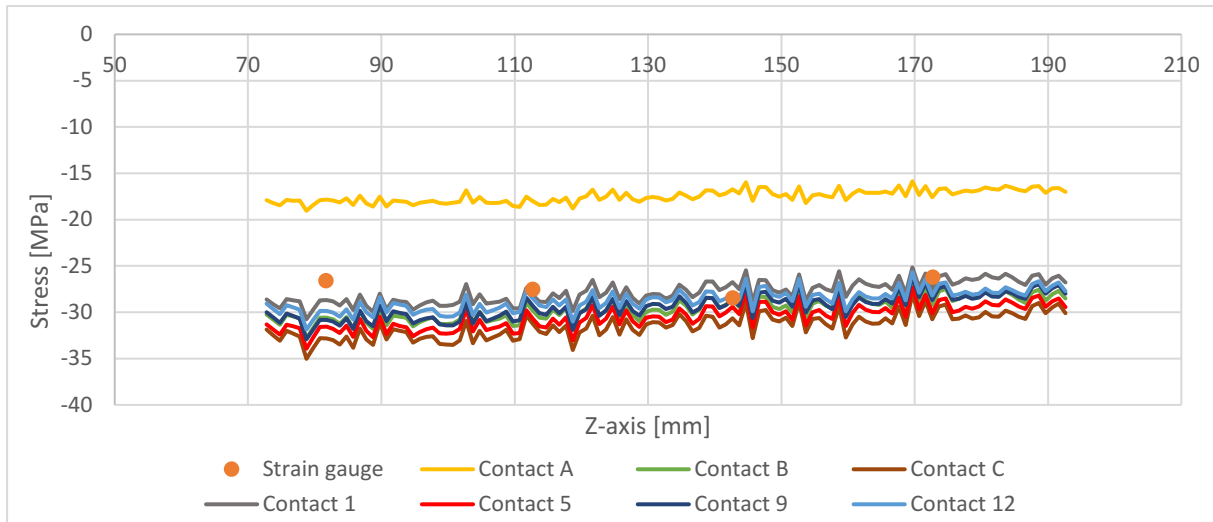
Figure 4-48: Case study of stresses located at the outer bottom radius on the engine side of the middle section.
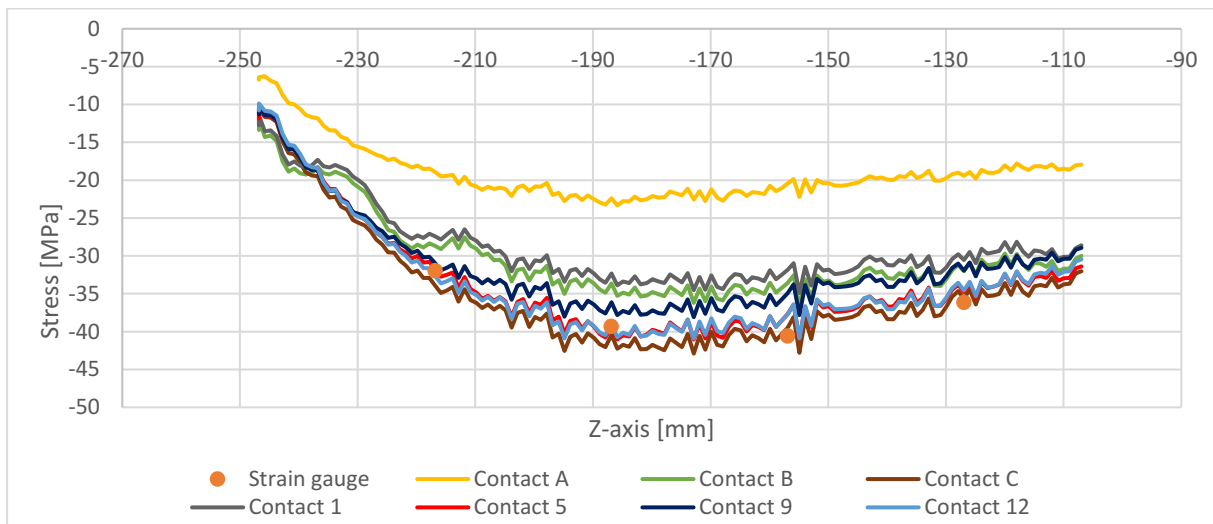
Figure 4-49: Case study of stresses located at the outer bottom radius on the engine side of the outlet section.

When studying the stresses located at the outer top radii on the engine side of both the middle and outlet section, it can be found that both contact 5 and 12 have a relatively good correlation against the experimental results. When studying the stresses located along the header wall and outer bottom radius, it can be found that contact 12 have a significantly better correlation against the experimental results compared to contact 5.
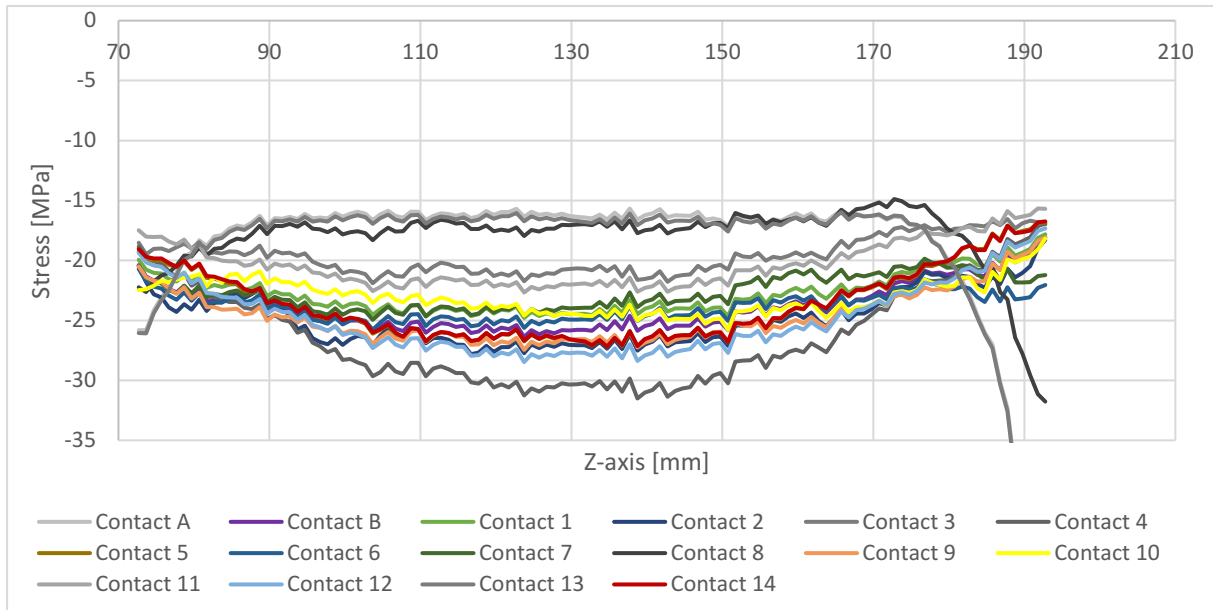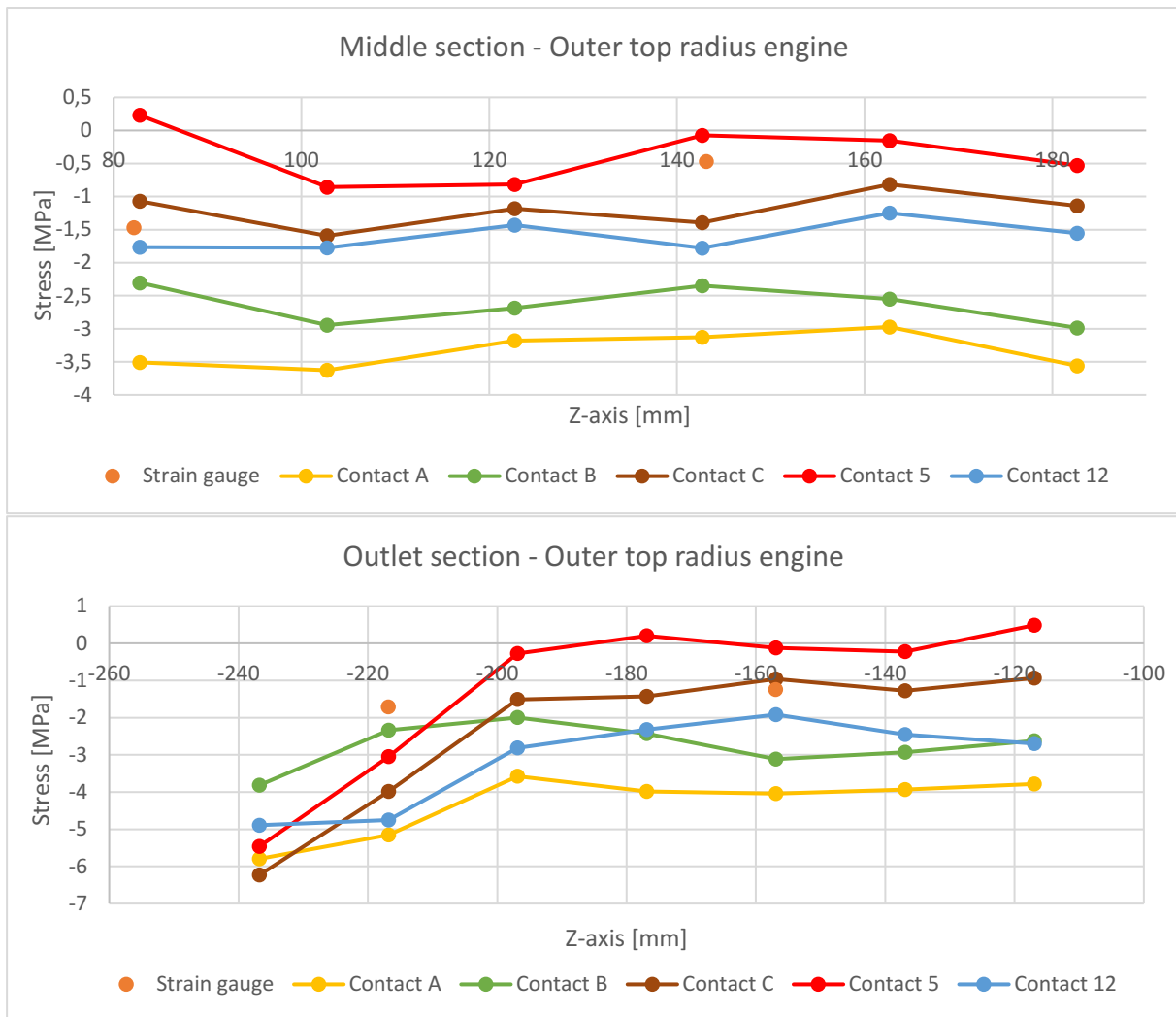
Figure 4-50: Case study of stresses located at the outer top radius on the engine side
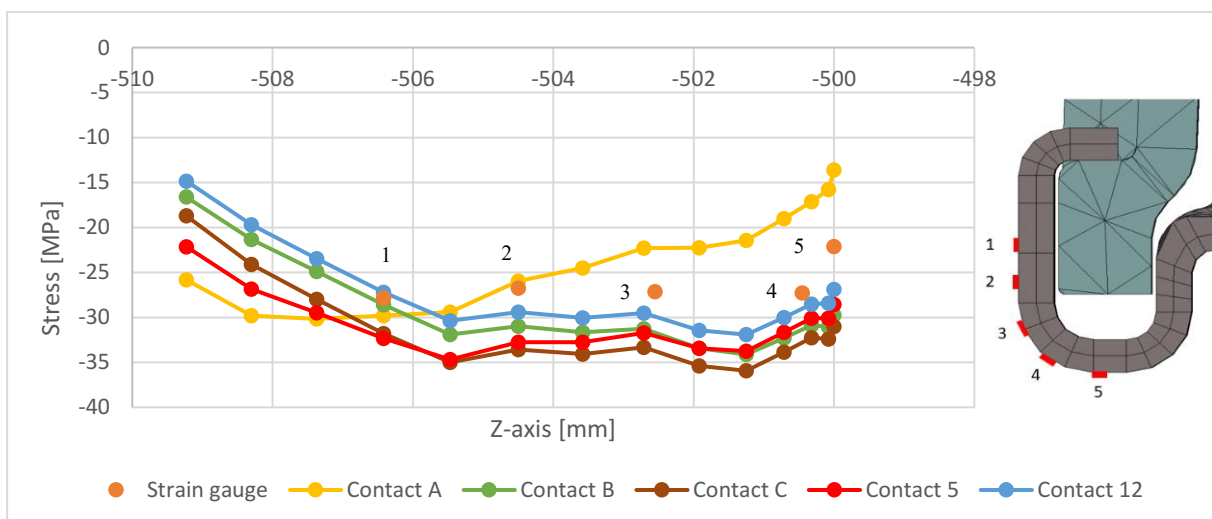
Figure 4-51: Case study of stresses located along the header wall and outer bottom radius.

As contact 12 was found to have a good correlation against all the experimental stress results located on the engine side, it was continued to be compared against the experimental stress results on the grill side as well, where a good correlation was found. These can be seen in Appendix E. The contact was also continued to be compared against the experimental displacement results at the header wall and

tank wall, which can be seen in Figure 4-52 and Figure 4-53. The contact is here found to have a good correlation against the displacements located at the tank wall on both the middle and outlet section. However, the displacements on the header wall do not have a good correlation as the contact results in a significantly lower displacement than the experimentally measured. Even though one of the displacements have been found to have a poor correlation between the numerical and experimental results, contact 12 was implemented in the FE model subjected to increased pressure of 160, 220 and 260 kPa. The testing of the remaining contacts, 6, 7, 10 and 14, was interrupted due to the rare behaviour of contact 12. When studying the stresses at the outer bottom radius of the middle and outlet section, all contacts have either higher stresses than contact B at both sections, or they have lower stresses, except contact 12. It has lower stresses compared to contact B at the middle section, and higher at the outlet, which was the exact behaviour that was sought.
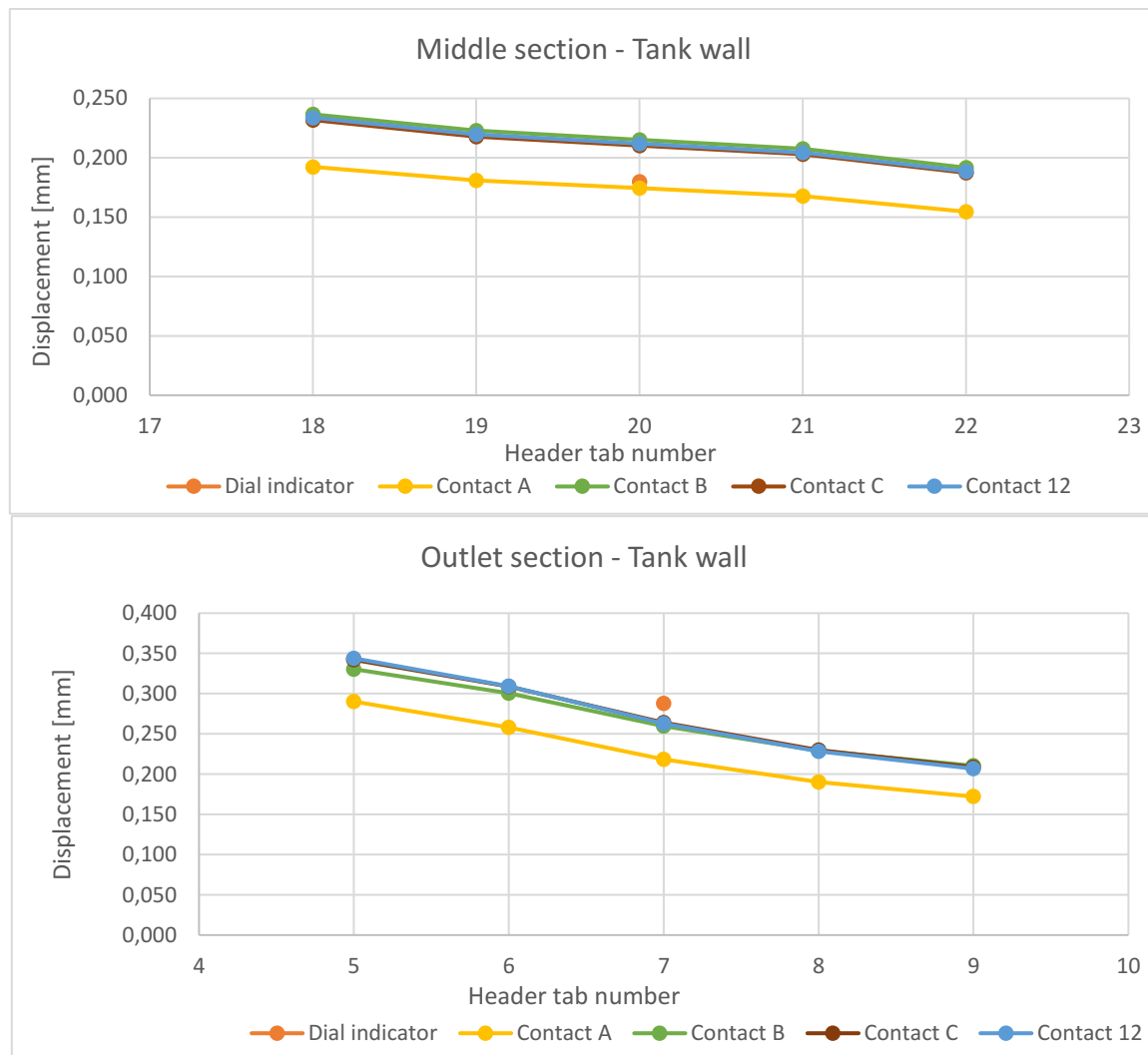
Figure 4-52: Correlation of displacements at tank wall caused by contact 12 in comparison to existing FE simulation methods.
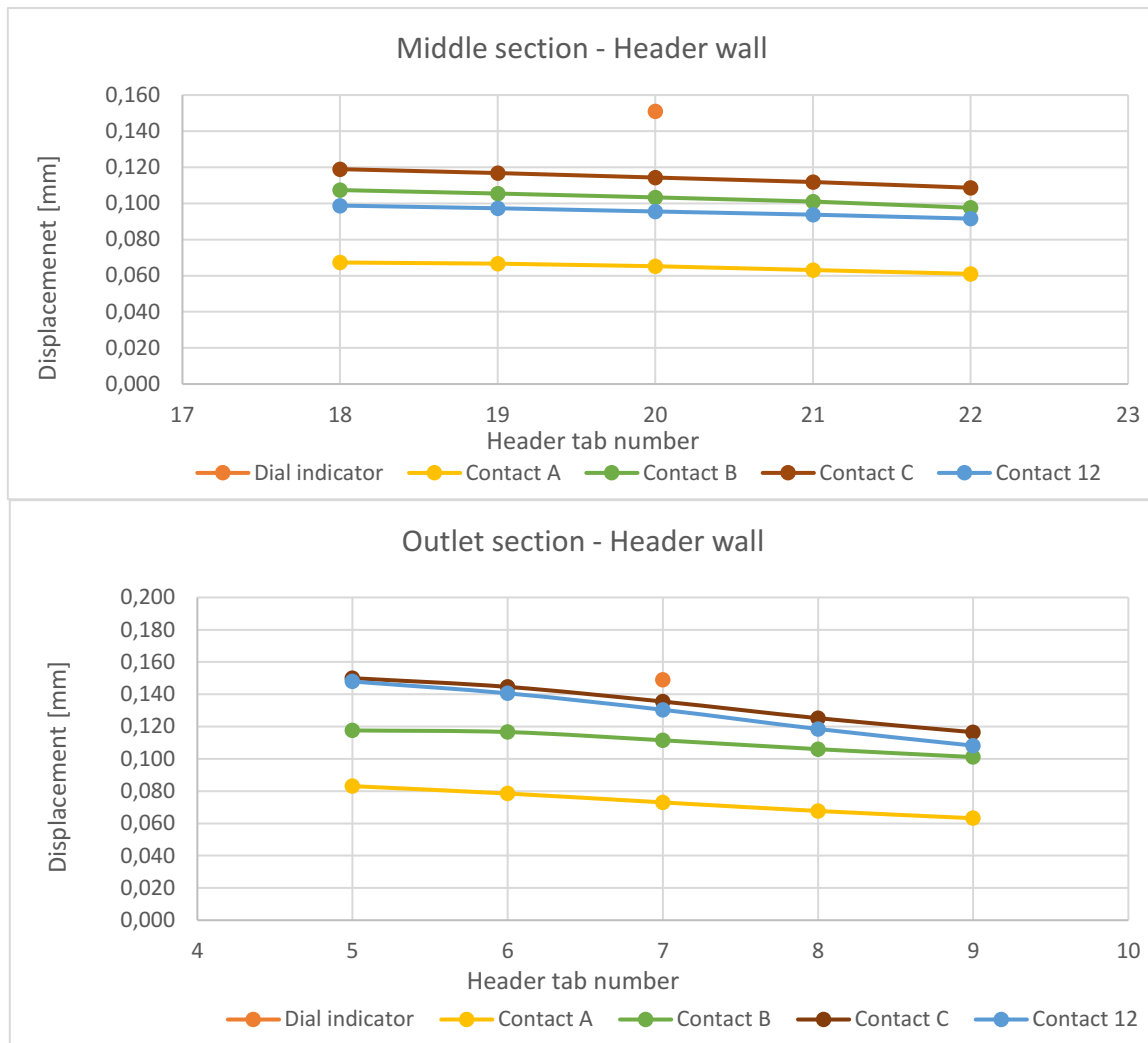
Figure 4-53: Correlation of displacements at header wall caused by contact 12 in comparison to existing FE simulation methods.

4.4.4 Verification of developed FE simulation method at increased pressure

The result of the stress correlation between the numerical results of contact 12 and the experimental results can be found in Figure 4-54 to Figure 4-56. The stress correlation on the grill side can be found in Appendix F. As can be seen on the outer bottom radius, the simulation method has a good correlation against the experimental results at 100 and 160 kPa. However, when the pressure is increased to 220 and 260 kPa, the numerical results are found to read lower stresses than the experimental results. At most, the numerical results are found to read 13 MPa lower stress than the experimental, and the highest margin of error found on the outer bottom radius is 16%.

However, when aluminium is brazed, the yielding limit decreases to around 60-70 MPa, but during manufacturing the header is also deformation hardened, meaning that the yield limit is increased. This can be the reason why the FE simulation method had a good correlation up to the internal pressure of 160 kPa, because at this pressure the material would start to yield if it was not deformation hardened. When the experimental study was conducted, the material was presumed to be operating in its linear region due to linear convergence of the strain measurements in Figure 4-5. As the setup of the FE model is linear elastic it can be the reason why the numerical and experimental results differ at increased load due to the yielding that might be occurring. The material properties of fibreglass-reinforced polyamide are also known to be easily affected by temperature [18]. The Young's modulus was therefore tested to be lowered from 5,3 to 4 GPa to study the sensitivity of the material property, but the change in stress was negligible.

64
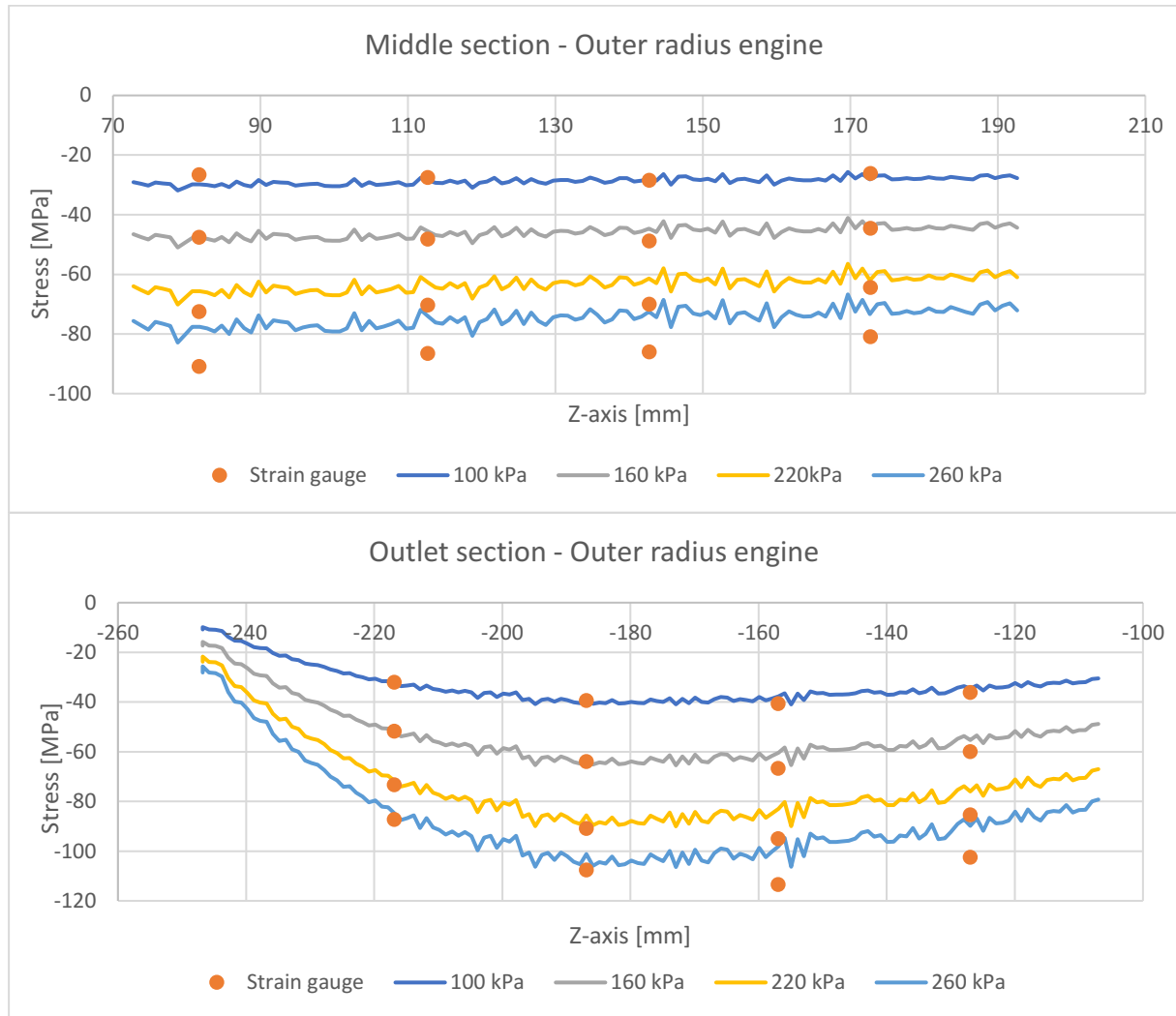
Figure 4-54: Correlation of stresses located at the outer bottom radius on the engine side.

When studying the stresses at the outer top radius, the experimental stresses are found to have a nonlinear increase at the middle section, while the numerical stresses behave linearly. However, when studying the stresses at the outlet section, the increase is still close to non-existent. At the low magnitude of stresses located at the outer top radius, all FE simulation methods have been struggling to read the same stresses as the experimental results. This may be due to the complex behaviour of the contact between the tank foot and the inner top radius where a combination of rolling and sliding are taking place. Having a model that completely mimics the behaviour of the contact may be too complex to implement in this area. However, as the magnitude of the stresses is low, the influence of the incorrect behaviour of the crimp joint is expected to be low, but it is still an indication that the structural mechanics of the crimp joint are incorrect at higher pressure.
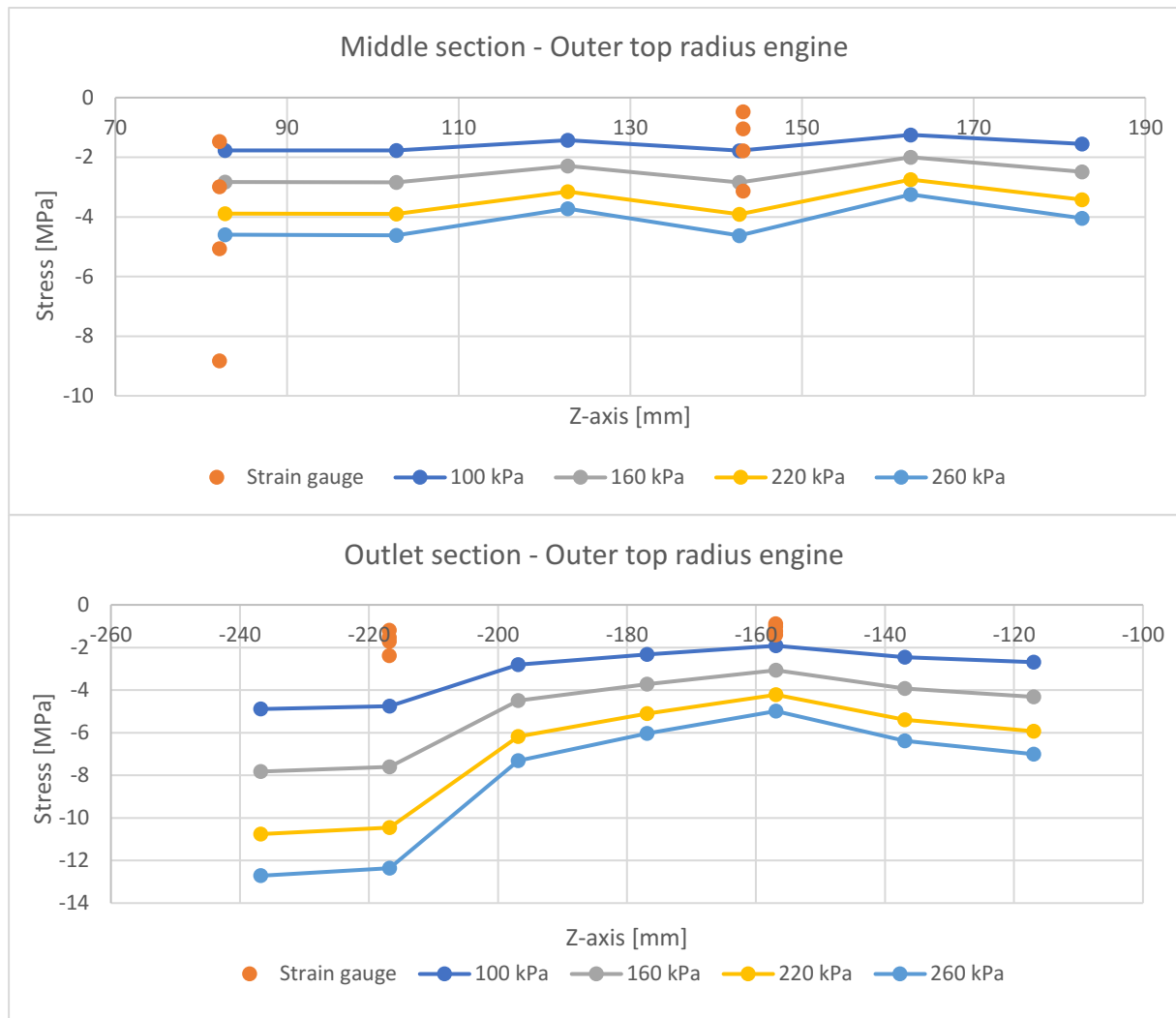
Figure 4-55: Correlation of stress located at the outer top radius on the engine side.

When studying the stresses located along the header wall and outer bottom radius of the crimp joint, the method is found to have a relatively good correlation, even at higher pressures. The method does still read lower stresses at the first and fourth strain gauge, where the fourth is mounted in the centre of the radius. As the method still do a good representation of the other sections according to the stress correlation, there might still be a slight geometry difference between the FE model and the manufactured crimp joint. There is also a slight difference in the geometry of each individual manufactured header, meaning that the radiator that was used to measure and update the crimp joint in 4.3.1, might have had a slight difference in geometry compared to the test specimen in the controlled experiment.
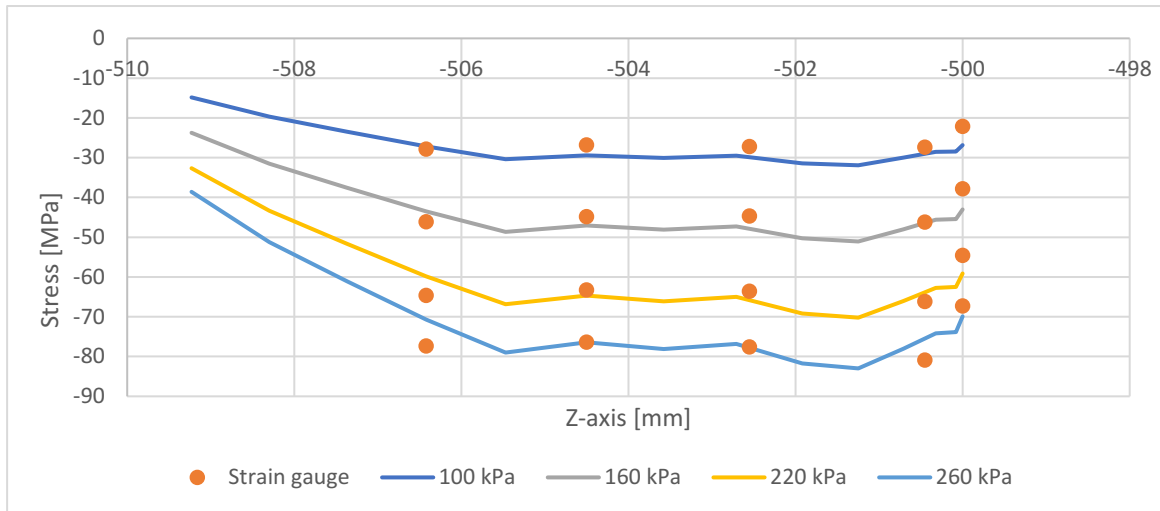
Figure 4-56: Correlation of stresses located along the header wall and outer bottom radius.

To answer the final thesis question regarding to what extent the new FE simulation method has minimized the margin of error, the error is studied at all four pressures. As all FE simulation methods have been struggling to measure the stresses at the outer top radius, and because these stresses are of a low magnitude, they are neglected when studying the margin of error. The margin of error can be found in Table 4-7 and the overview of the instrumentation can be found in Appendix A. The highest margin of error found on the FE model regards SG23 which has a margin of error of 21.6% at the pressure of 100 kPa. The reason why the measurements differ at this position may be because the stresses are very sensitive to small changes in position at the bottom of the header. There are several nodes placed at the bottom of the header, meaning that the exact node to read the stresses from is complicated. Otherwise, the maximum margin of error is 16% at the outer bottom radius at the pressure of 260 kPa. Thus, the FE model has a margin of error of up to 16% at the outer bottom radius of the crimp joint where the highest stresses are located. Compared to the existing FE simulation method with the lowest margin of error at 100 kPa, the average margin of error is lowered by 4,6%, but the margin of error is more even between all comparisons against the strain gauges. This is beneficial when the FEA is used to determine the area of failure.

Table 4-7: Margin of error of contact 12 at the outer bottom radius and header wall.

Name	100 kPa	160 kPa	220 kPa	260 kPa
SG03_ORE_3	2,2%	1,2%	-2,0%	-2,7%
SG04_ORE_4.5	-1,0%	-2,6%	-5,7%	-5,8%
SG05_ORE_6	-7,0%	-9,5%	-12,6%	-13,5%
SG06_ORE_7.5	-7,1%	-10,4%	-13,5%	-14,9%
SG09_ORG_3	7,8%	4,4%	2,4%	0,8%
SG10_ORG_4.5	-1,4%	-4,9%	-6,8%	-8,9%
SG11_ORG_6	0,1%	-3,0%	-5,3%	-6,5%
SG12_ORG_7.5	-2,9%	-6,6%	-9,3%	-10,8%
SG15_ORE_18	12,3%	0,4%	-9,4%	-14,6%
SG16_ORE_19.5	3,6%	-5,4%	-10,8%	-14,4%
SG17_ORE_21	-1,9%	-8,5%	-12,3%	-15,6%
SG18_ORE_22.5	7,6%	1,3%	-3,6%	-9,4%
SG21_ORG_18	-3,0%	-6,8%	-9,3%	-11,4%
SG22_ORG_19.5	-11,0%	-12,7%	-14,4%	-16,0%
SG23_ORG_21.1	21,6%	13,7%	8,4%	3,9%
SG24_ORG_21.2	4,5%	-1,2%	-5,2%	-8,3%
SG25_ORG_21.3	8,9%	5,9%	2,3%	-0,9%
SG26_ORG_21.4	9,9%	4,9%	2,3%	0,1%
SG27_ORG_21.5	-2,3%	-5,6%	-7,4%	-8,5%
SG28_ORG_22.5	1,6%	-1,6%	-3,9%	-6,1%
Average	**5,9%**	**5,5%**	**7,2%**	**8,7%**
Average	**6.9%**			

SGXX_AAB_YY.Y
SG = Strain gauge
XX = strain gauge number
AA = position of strain gauge: OR = outer bottom radius, TR = outer top radius
B = side of radiator: E = engine side, G = grill side
YY.Y = header tab number

The result of the displacement correlation can be found in Figure 4-57 and Figure 4-58. The displacements located at the tank wall are found to have a good correlation between the developed FE simulation method and the experimental results. This is an indication that the used linear simplification of Young's modulus of the anisotropic polyamide tank is a reasonable simplification to be made up to the pressure of 260 kPa. It is also an indication that the Young's modulus discovered during the study of the material in chapter 4.2 is reasonable.
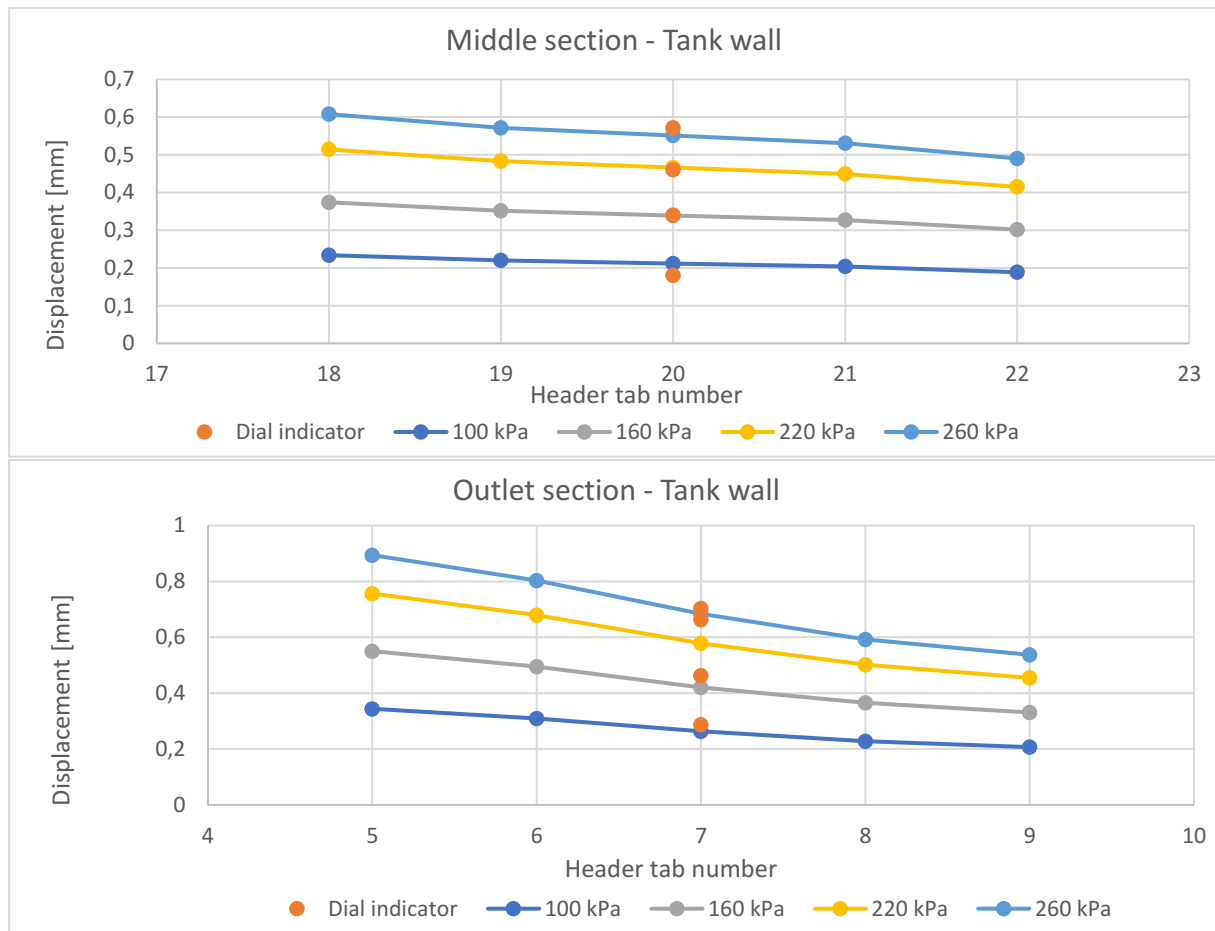
Figure 4-57: Correlation of displacement located at the tank wall

However, when studying the displacements located at the header wall, the correlation between the simulation method and the experimental results is found to be poor, even at low pressure. Even if the experimentally measured displacements are uniform and have an almost linear convergence in Figure 4-15, there is a deviation in the linearity check. It can be an indication that the contact method of the crimp joint is incorrect at higher pressure. If the header tab would in practice slide along the tank foot, it is constrained by the no separation contact defined between the inner top radius and the radius of the tank foot in the FE model. This means that the header can only slide in a spherical motion around the radius of the tank foot.
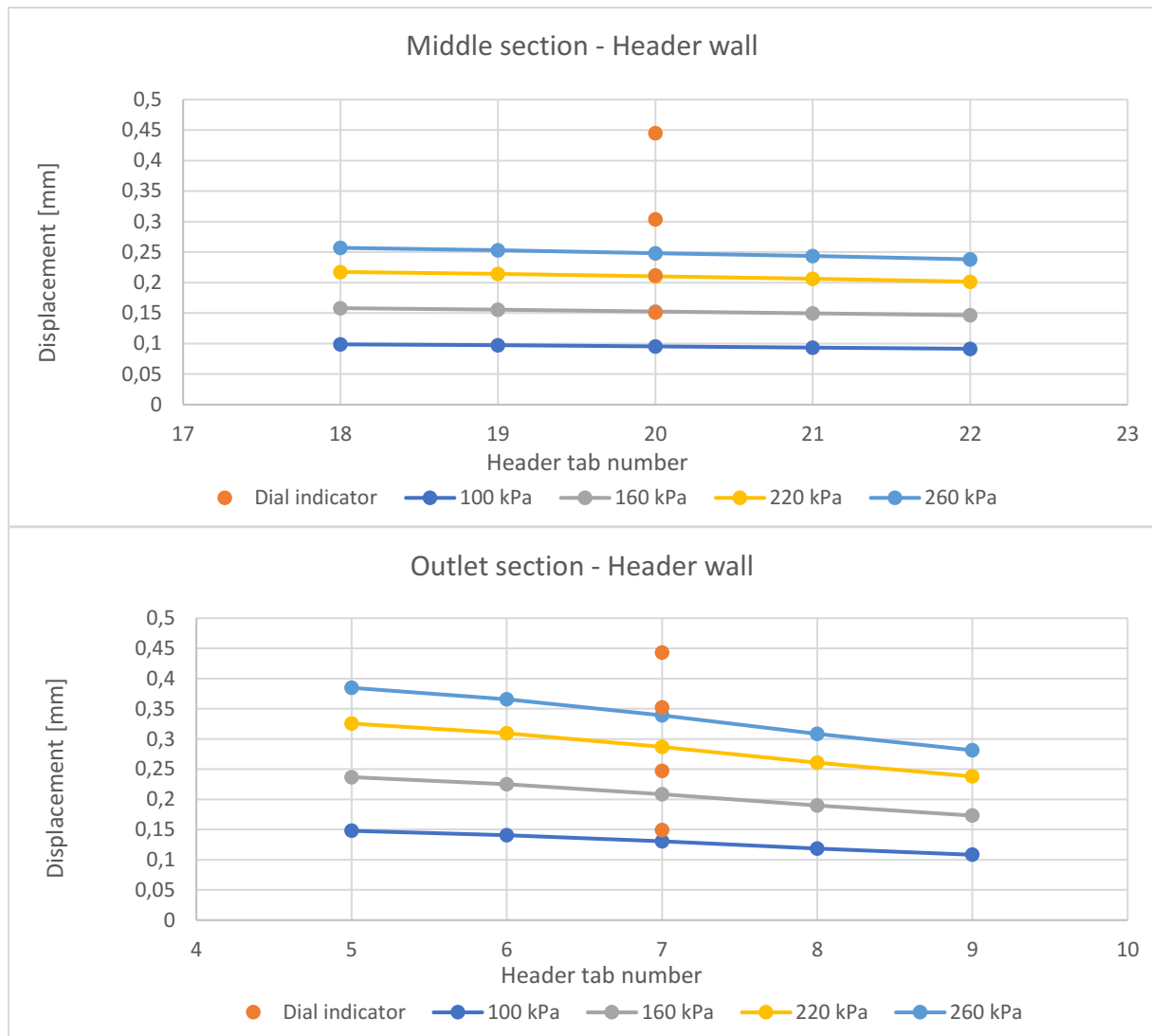
Figure 4-58: Correlation of displacements located at the header wall.

4.4.5 Evaluation of development method

Throughout this thesis, several evaluations have been made of the attained experimental data, the method of calculating the displacements and stresses, and the method of comparing the experimental and numerical results. However, there are three methods that have not been evaluated, the simplification of a uniaxial stress state in the controlled experiment, the usage of linear elements, and the method of analysing the stresses in the nodes of the FE model where it is not certain that the stresses are at the surface.

To evaluate the simplification of a uniaxial stress state, the experimentally measured strains are compared against numerical strains instead of the stresses. When comparing the strain, the method of calculating the stresses through Hooke's law can be avoided. Thus, the strains are analysed in the same nodes as the stresses, but instead of analysing the minimum principal strains like the minimum principal stresses, the normal strains are analysed instead. The normal strains are measured by setting up a local coordinate system that tangents the outer bottom radius of the crimp joint. The top radius is neglected in this evaluation due to strains measured is too low to be seen as interesting. If the simplification is just, the correlation between the numerical and experimental results should be similar to the presented results in chapter 4.4.4.

To evaluate the usage of linear elements, parabolic elements are implemented in the FE model to compare the results against the linear. If the results are the same between the two types of elements, the usage of linear elements is verified. To evaluate the method of comparing the numerical results in the nodes against the experimental, a shell element is implemented in the model by adding a surface coating.

With the shell element, the results analysed are at the surface of the header, which is the position of the highest strains. In Figure 4-59 to Figure 4-61, the evaluation of the three mentioned methods can be seen.

Figure 4-59: Correlation of strains located at the outer bottom radius on the engine side.

Figure 4-60: Correlation of strains at the outer bottom radius on the grill side.

Figure 4-61: Correlation of strains located along the header wall and outer bottom radius

When studying the results of the linear elements it can be found that the correlation between the numerical and experimental results have deteriorated compared to the results presented in chapter 4.4.4. This is due to the simplification of a uniaxial stress state was invalid. However, the representation of the crimp joint is still relatively good, except at the outlet section of the engine side. When studying the

results of the parabolic elements with and without shell elements, it can be found that the results are equal and the method of analysing the stresses and strains in the nodes is verified. However, the method of using linear elements is found to be invalid as there is a significant change in the numerical strains when the parabolic elements are implemented. This error can also be corrected by increasing the number of linear elements, but when the absolute stresses are sought, the usage of parabolic elements are preferred due to the increased precision it entails compared to linear elements. Thus, the methods of comparing the numerical stresses against the calculated stresses according to a presumed uniaxial stress state, and the usage of linear elements in the FE model, are found to be invalid. However, the two errors are counteracting each other where the final result, after adjusting the invalid methods, still is a good representation of the crimp joint. Thus, the developed method of contact 12 to represent the crimp joint needs to be verified at the increased pressures again, but for this verification, the elements of the header are parabolic and the strains are compared instead of the stresses, this can be found in Figure 4-62 to Figure 4-64. As the two methods have been found to be invalid, it also means that the method used during the verification of the existing methods of representing the crimp joint is invalid. However, as the results only have slightly changed, the existing methods are still presumed to be representing the crimp joint insufficiently and the determined margin of error is assumed to be of the same magnitude as earlier.

As can be seen in the figures, the correlation between the numerical strains of contact 12 and the experimental is similar to the results presented in chapter 4.4.4. The magnitude of the numerical results has slightly increased. However, the increase has not affected the contact's ability to represent the crimp joint sufficiently. The margin of error found at all four pressures can be found in Table 4-8. The maximum margin of error has now increased to 19,6% at the outer bottom radius, however, the average margin of error is still equal to the previous of 6,9%.
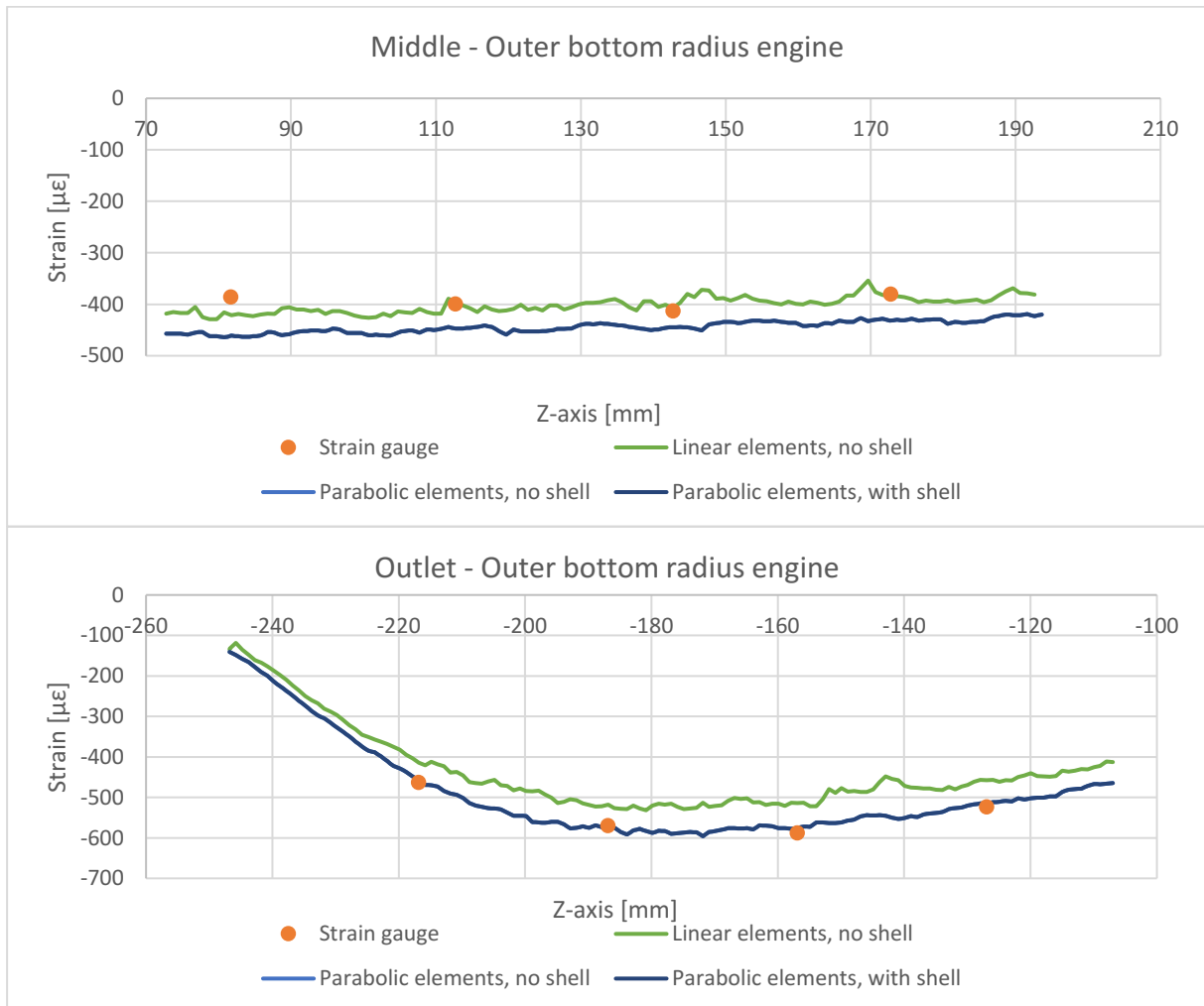

Figure 4-62: Stress correlation of strains at the outer bottom radius of the engine side
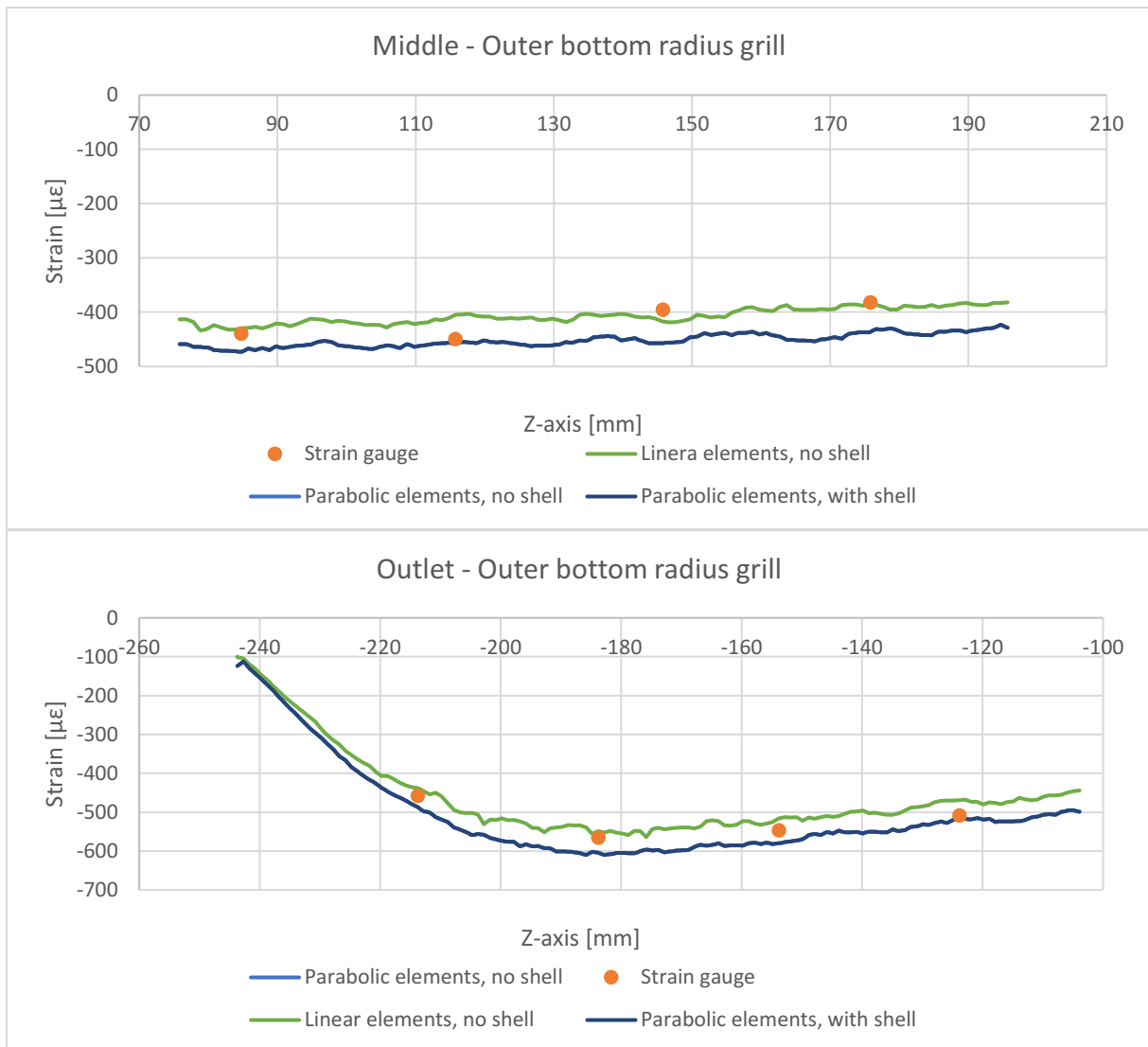
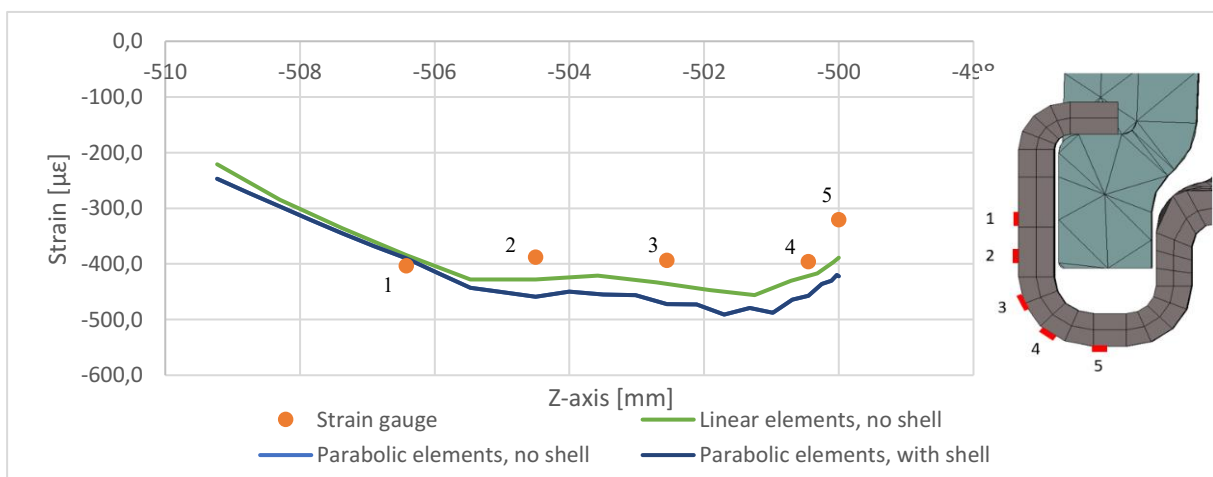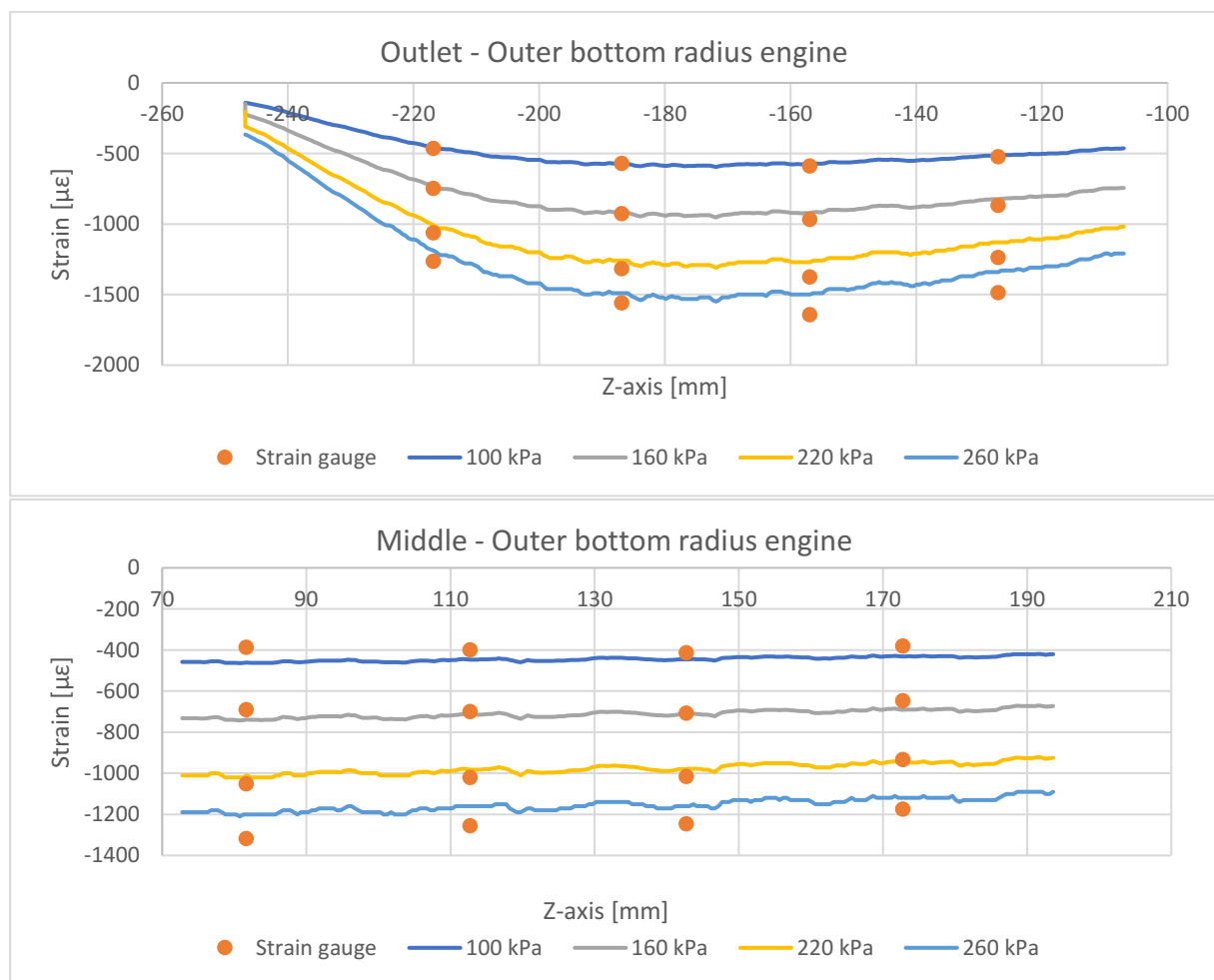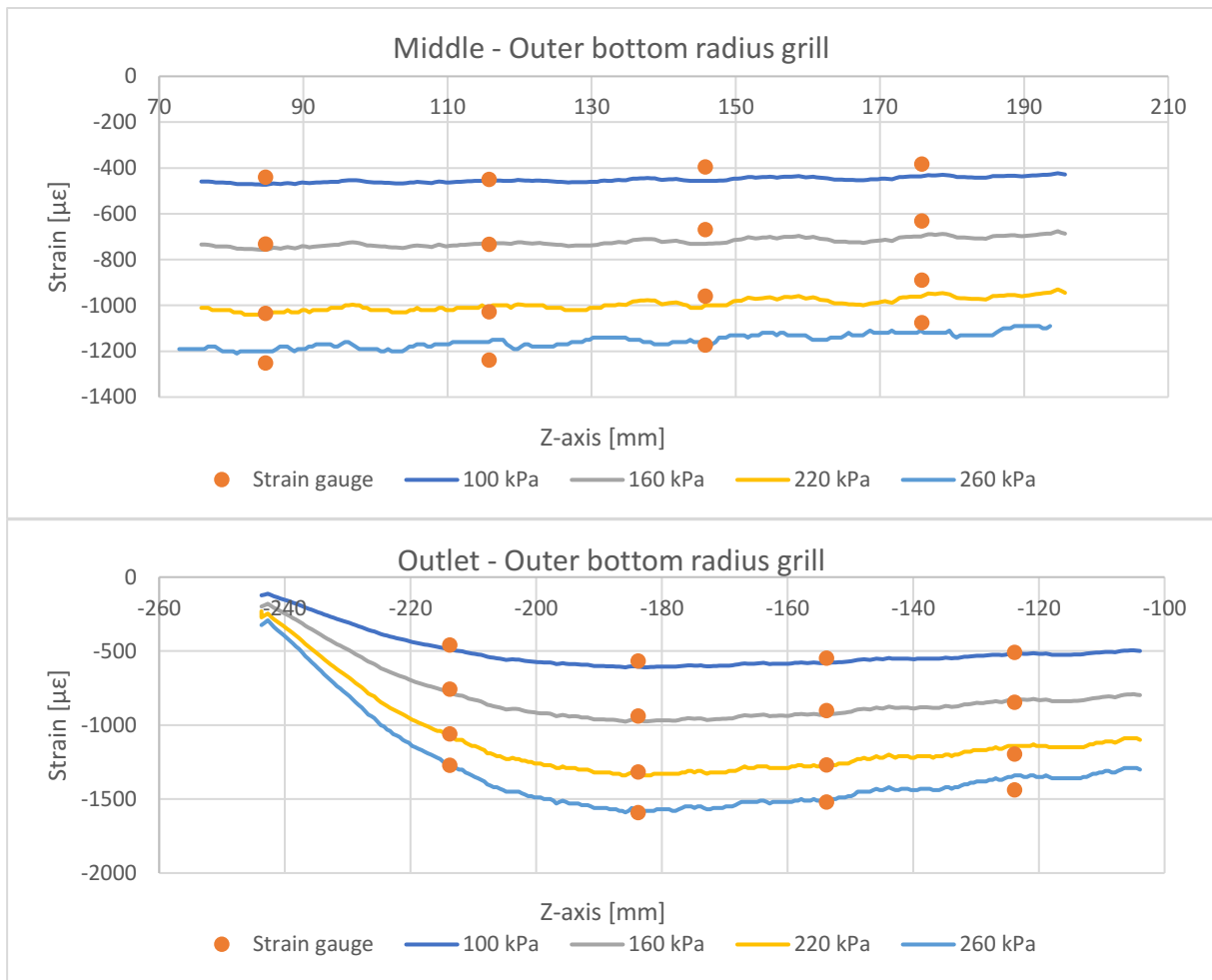Figure 4-63: Correlation of strains at the outer bottom radius of the grill side.
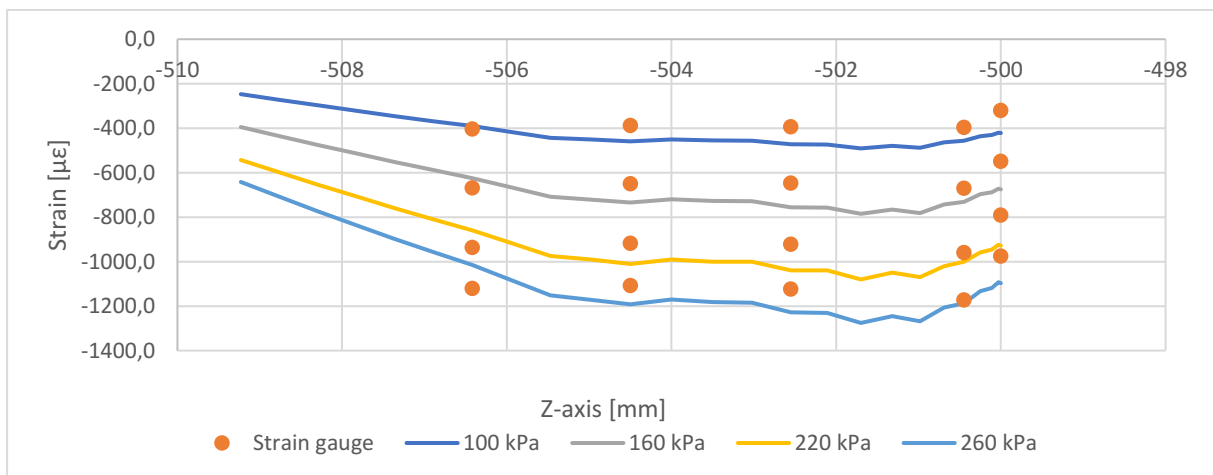
Figure 4-64: Correlation of strains located along the header wall and outer bottom radius.

Table 4-8: Margin of error of contact 12 at the outer bottom radius and the header wall.

Name	100 kPa	160 kPa	220 kPa	260 kPa
SG03_ORE_3	1,2%	3,1%	6,2%	5,9%
SG04_ORE_4.5	0,5%	1,0%	4,2%	4,4%
SG05_ORE_6	2,1%	4,6%	7,6%	8,7%
SG06_ORE_7.5	1,7%	5,1%	8,6%	9,8%
SG09_ORG_3	6,5%	2,3%	0,1%	0,1%
SG10_ORG_4.5	6,9%	3,0%	1,1%	1,3%
SG11_ORG_6	6,2%	3,1%	0,8%	0,6%
SG12_ORG_7.5	1,8%	1,7%	4,6%	6,7%
SG15_ORE_18	19,6%	7,0%	3,8%	14,2%
SG16_ORE_19.5	12,1%	2,4%	3,5%	7,5%
SG17_ORE_21	7,9%	0,8%	3,4%	10,1%
SG18_ORE_22.5	13,8%	7,1%	1,8%	2,0%
SG21_ORG_18	7,7%	3,4%	0,6%	1,6%
SG22_ORG_19.5	1,9%	0,1%	1,7%	3,8%
SG23_ORG_21.1	31,8%	23,2%	17,4%	12,6%
SG24_ORG_21.2	15,5%	9,2%	4,3%	1,3%
SG25_ORG_21.3	20,0%	16,9%	12,9%	9,3%
SG26_ORG_21.4	18,4%	13,0%	10,2%	7,8%
SG27_ORG_21.5	3,3%	6,5%	8,2%	9,4%
SG28_ORG_22.5	14,4%	10,7%	8,1%	6,1%
Average	**9,7%**	**6,2%**	**5,5%**	**6,2%**
Average	**6,9%**			

SGXX_AAB_YY.Y
SG = Strain gauge
XX = strain gauge number
AA = position of strain gauge: OR = outer bottom radius, TR = outer top radius
B = side of radiator: E = engine side, G = grill side
YY.Y = header tab number

5 DISCUSSION

5.1 Controlled experiment

5.1.1 Experimental stress analysis

The first step of finding the margin of error of the existing simulation method was to attain data to compare the numerical results against. The method of using strain gauges to determine the stress of the header came naturally due to the low amount of commercially available methods to determine mechanical stress. FEA is one of the most widely used methods to determine stress in a body, but as the aim of this thesis is to develop a FE simulation method, it cannot be verified against another FEA. The choice of conducting the experiment in a pressure pulsation rig instead of a rig with constant pressure was that the components and materials are presumed to require some pulsations to stabilise the movements. It was also conducted in a pressure pulsation rig as the customers specify pressure pulsation tests during the development of new coolers. In order to verify a method used for simulating pressure pulsation tests, the experiment must be set in a pressure pulsation rig. The air was chosen as media instead of water to simplify the environment and neglect the influence of hygroscopy that affects the elasticity of the tank. Even though the influence of hygroscopy was avoided during the experiment, the elasticity of the tank had to be determined through another study as the material data provided by the manufacturer could not be used due to the difference in thickness and fibre orientation of the anisotropic material compared to the ISO standard specimen. Thus, using water as media would have been equally problematic. However, it would be to prefer to study the crimp joint with water as media as it is the work environment of the joint.

The results of the strain measurements have high reliability according to the shunt calibration where the maximum error was found to be 1.5% due to calibration. Unfortunately, the range of the strain between each pulsation could not be studied as planned as the rig had residual pressure between each pulsation. Thus, the bottom range of the strain had to be extrapolated with a linear assumption. The linear assumption is only valid if the material is working under linear circumstances. The linearity of the material at the four loading conditions was therefore studied, and it was found to have a good linear convergence, which arguments for the linear assumption. The 100% correlation between the calibration of the pressure gauge before and after the experiment argues for the precision of the pressure measurements as well. The p-p amplitude of all strain and pressure measurements are constant, making the extraction of ΔP and $\Delta \varepsilon$ free from assumptions. The calculated stresses at the outer bottom radius are uniform between the strain gauges, meaning that all strain measurements are seen as highly trustworthy for comparison against the results of the numerical analysis. However, the measured strains by the strain gauges are always slightly lower than the actual as the bonding to the surface never is perfect.

5.1.2 Experimental displacement analysis

The results of the measurements with the dial indicators are not as uniform as the results of the strain gauges, making some of the results questionable. The displacements of the header walls and tank walls at both the middle and outlet section of the radiator are uniform with a constant p-p amplitude at all four loading conditions, making them trustworthy. The measured displacements at the header tabs and the tank tops are on the other hand more questionable, but they all are relatively uniform at the pressure pulsation at 100 kPa. The p-p amplitude is still not constant at 100 kPa, but the $\Delta \delta$ is measured at the areas where the measurements are uniform, where the high peaks are explained as vibrations, and the drifting of both maximum and minimum value of each pulsation is explained as the radiator moving or movement in the crimp joint. Some of the results are uniform with a constant p-p amplitude at the higher pressures as well. However, as all measurements of the displacements are most uniform at the pressure pulsation at 100 kPa, this specific load was chosen to be the main work environment when verifying and developing the FE simulation methods. The reason why the measurements at the higher loads are irregular can be caused by the EPDM gasket. The gasket can absorb some of the displacements because of its elastic and damping properties. The displacements at the header tabs and the tank tops are also smaller than the displacements at the tank wall and header wall, making them more sensitive to small changes.

The problem of the pressure pulsation rig, where it does not completely relieve the pressure between the pulsations, proved to be a bigger problem when studying the linearity of the displacement measurements at the four loading conditions. The usage of linear extrapolation to determine the lower range of the displacements becomes a questionable method in the cases of the header tabs and header wall in the middle section as they do not have a linear convergence. The behaviour at the tabs and wall of the different internal pressure can also be caused by the nonlinear material properties of the EPDM gasket as well. The nonlinear convergence can also be caused by measuring errors, or the p-p amplitude not being constant when analysing the data. Even though the tank top measurements have a good linear convergence, the linear extrapolation is not trustworthy either as the displacement measurements are nonuniform and the p-p amplitudes are not constant. The measurements at the tank walls have on the other hand a good linear convergence, making these results the most trustworthy. Still, all results were used during the verification of the simulation method at the pressure of 100 kPa, but the measurements at the tank walls and header walls are seen as the most trustworthy. Thus, these were the only displacements used during the development of the new FE simulation method for the crimp joint.

5.2   Elasticity of PA66GF30

To be able to determine the margin of error of the existing FE simulation method, the material properties must be known. The result of the study shows that the Young's modulus of PA66GF30 was considerably lower than expected, which gave major effects on the displacements and stresses in the FEA. The known difference between the material studied in this thesis, and the material studied by De Monte et al. is the amount of fibreglass-reinforcement in the polyamide [18]. The material studied by De Monte et al. has a 35% reinforcement, compared to the 30% in this thesis, which may be the reason for the difference. Another cause of the difference can be the length of the glass fibres. When a load is applied parallel to the fibre orientation of the reinforcement, the material reaches its maximum tensile strength, whereas when the load is applied perpendicular to the fibre orientation, the material has its lowest tensile strength. If the material is thin, the orientation of fibres can be controlled better, whereas when the material is thicker, the orientation becomes more unstructured as the fibres have more space to rotate [18]. If then the fibres of the reinforcement are shorter, it can have the same effect as if the material was thicker. The length of the fibres is unfortunately not known for any of the studies.

As with all controlled experiments, it can be complicated to draw conclusions from only one experiment. To gain a more trustworthy result, several cut out sections of different tanks should be tested and analysed to gain a wider perspective of the material property. The precision of the load cell is relatively bad at small loads, meaning that the loads measured to reach the displacement of 0,15 and 0,3 mm is unreliable. However, as the loads are studied at a greater displacement as well, this error can be neglected. There is also a small error in the simplification of the loading case in the FE model. In practice, there is not an even load distribution to the tank foot. Instead, one of the edges will be subjected to the applied force from the load cell depending on the displacement. At small displacements, the left edge on the top tank foot in Figure 3-8 will be subjected to the force, when the tank is compressed more, the right corner of the tank foot will be subjected to the force instead. Using a tensile testing machine would increase the precision of the experimental measurement. However, measuring the displacement becomes more complicated as extensometers cannot be used. Even though the precision of the study can be increased, the result is expected to be within an acceptable margin of error as small changes in the Young's modulus was proven to have a negligible effect on the stresses.

5.3   Verification of existing FE simulation methods

Even though the sizing of the mesh was refined, and the geometry was updated to the actual of the manufactured radiator, the results show that the method of representing the crimp joint according to contact A is insufficient due to the average margin of error reaching 37,9% at the outer bottom radius. Even though the method of verifying the existing simulation methods of the crimp joint was found to be invalid, the expected difference of the margin of error is expected to be low. The crimp joint is found to be too constrained from displacing with the contact, which leads to the low numerical stresses compared to the experimental. The reason why the method has identified the hot spot stress locations well in

practice may be due to the coarse mesh in the model where it caused an increased concentration of the stresses in the outer bottom radius that disappeared when the mesh was refined. These stresses have not been considered in this study and might be the reason why it has had good results. The stresses are also known to be heavily influenced by the environment, where the method of simulating the crimp joint may have less effect on the stresses and displacements in a conditioned environment.

The sizing of the mesh in the current simulation method is problematic due to its nonuniform stresses along the measured line of nodes, and due to generally lower minimum principal stresses elsewhere. The updated geometry had small effects on the stresses at the outer bottom radius on the middle section, but had larger effects on the stresses at the outlet section, where the highest minimum principal stresses are located on the radiator. Thus, in order to analyse the absolute stresses of the radiator, the geometry of the radiator must be the actual of the manufactured, and the mesh needs to be refined. The updated geometry also gave a better correlation against the experimental results at the outer top radius. However, the stresses at the outer top radius are not as interesting to analyse as previously thought, due to them being close to non-existent in DAM conditions.

The evaluation of the two other methods, contact A and B, gave on the other hand a better correlation against the experimental results. Contact C had a margin of error of under 7% at the outer section of the radiator, which is seen as a sufficient simulation method in that section, but in the middle section, it has a margin of error of up to 40%, meaning that it is not representing the crimp joint sufficiently in the rest of the radiator. Contact B had the evenest margin of error of the three methods, where the average was 13,4%. For fatigue life assessments, a margin of error of 5-10% is preferred. However, the large variations of the errors compared between the two sections prove that the methods are insufficient at representing the actual behaviour of the crimp joint. The comparison of the displacement against the experimental results are also generally better with contact B and C compared to contact A, but both methods are still too constrained compared to several of the experimental measurements. The experimental results are however not reliable in the cases of the tank tops and header tabs, therefore the comparison against these results have been mostly neglected. However, the displacement and the stresses usually work as a pair, when the displacement increases, it causes an increased strain in the material, resulting in the increased stress in that location. When comparing the experimental and numerical results at the middle section, both contact B and C results in too high stresses, simultaneously as the header wall is displacing less than the experimental, fighting against the general relationship between displacement and stresses. The same pattern can be seen when studying the stresses and displacements at the outlet section with contact C. The stresses have a good correlation against the experimental results, but the header wall and tank wall is still displacing less in the FE model compared to the experimental results.

5.4   Development of FE simulation method

5.4.1   Case study

The usage of a submodel speeded up the process of testing several methods of representing the crimp joint. However, the results of the submodel were at first expected to give a good representation of the crimp joint in the global model when contact B was set as reference contact in the global model. It was soon discovered that the results in the submodel and global model could vary greatly when the methods tested in the submodel later were implemented in the global model. The methodology of conducting the case study had therefore to be changed. Instead, the constraining method of contact A was set in the global model, then the simulated methods in the submodel would have a distinct behaviour if they would lead to higher displacements and stresses as set by the benchmark of contact B. This was exploited as presented in chapter 3.4.1, and the results gave several methods with similar results as contact B in the global model.

Even though only 14 methods have been reported in this report, more methods have been tested. Many of those that have not been reported for, have had small changes compared to those that have been reported, and are therefore seen as superfluous to present as they have had no impact on the stresses and displacement of the crimp joint. There have also been methods that have resulted in a supernatural behaviour of the crimp joint, as well as there have been underconstrained methods, these have also been seen as superfluous to report.

When the case study continued in the global model, the behaviour that was sought of the new method was clear. The results should have lower stresses than contact B at the outer bottom radius in the middle section, but higher at the outlet section. The other methods tested, 1, 5, and 9, all had the same behaviour, if the stresses were increased at the middle section compared to contact B, the stresses were also increased at the outlet section, and vice versa if the stresses were lower. However, when contact 12 was compared against the results of contact B, it had lower stresses at the middle section, and higher at the outlet section. This is an interesting discovery of how the behaviour of the contact is different compared to all other tested methods, including contact A and C if they were compared against B as well. As the sought behaviour was found, the case study was interrupted, this means that several of the tested methods in the submodel, that were to be implemented in the global model, could have had better results than contact 12. However, the case study needed to be interrupted at some point in the study.

In the already existing simulation methods and the developed method, the gasket has not been implemented in the FE model. Implementing the gasket in the FE model would require an iterative solver to cope with the nonlinear material properties of the EPDM gasket. Implementing the gasket would therefore increase the simulation time and the complexity of setting up the FE model. Thus, excluding the gasket in the FE model was favourable. However, there has not been any delimitation of it. As contact 12 were found to represent the crimp joint sufficiently at 100 kPa, there was no reason to further investigate how to implement the gasket in the model as the sought result had been found.

5.4.2   Verification of developed FE simulation method at increased pressure

Unfortunately was the method of comparing the numerical and experimental results found to be invalid late in the thesis. This has affected the presented margin of error of the existing FE simulation methods of the crimp joint and the developed method contact 12. However, the margin of error of contact 12 was corrected after adjusting the method of comparing the results, and was found to still have the same average margin of error of 6,9%. The reason why the average margin of error has not changed is because the method now represents the crimp joint slightly better at the increased pressures at the same time as it represents the crimp joint slightly worse at the lower pressures. On the other hand, the numerical results should read higher strains than the experimentally measured as the strain gauges always measure too low strains compared to the actual as described in chapter 5.1.1. After the method of comparing the numerical and experimental results was adjusted, the margin of error was more evenly distributed between the four pressures. This increases the precision of fatigue life assessments if they are conducted in the higher ranges of pressures. As the requirement specification from customers usually includes the range between 160-260 kPa, this is the range where the fatigue life assessments are conducted.

When the linearity check was conducted on the strain gauge measurements, the strains were found to have a linear convergence at all pressures. This indicates that the material is operating in its linear-elastic region. However, the brazed aluminium is known to yield at 60-70 MPa. If the presented experimental stresses are of the same order of magnitude as if they were calculated with a correct plane stress state, it means that the material is yielding. When the crimp joint is manufactured, the material is deformation hardened, which increases the yield limit. How much the yield limit has increased can be determined by simulating the manufacturing process of the crimp joint. However, the developed method of representing the crimp joint is sufficiently representing the crimp joint both according to the actual behaviour of the crimp joint, and the average margin of error that is in between the preferred 5-10% for fatigue life assessments. Thus, the benefit of implementing an elastic-plastic solver to simulate the yielding that might be occurring, might not be worth the complexity it causes. However, if the margin of error still is found to be too high, further investigations of the yield limit are necessary.

6   CONCLUSION AND FUTURE WORK

In this thesis, the margin of error was determined for the existing FE simulation methods used by the corporate partner for representing the crimp joint. It was determined by using strain gauge measurements in a pressure pulsation rig at DAM conditions as a reference for the numerical analysis. The experimental stresses that were compared against the numerical, were calculated according to a presumed uniaxial stress state after considering the principal direction of the stresses. Thus, the numerical results that were compared against the experimental, were also extracted in the same principal direction. The average margin of error found of the simulation method used in the original FE model, was determined to be 49,2% at an internal pressure of 100 kPa. However, the incorrect geometry found in the FE model resulted in an unjust comparison of the numerical and experimental results. The geometry of the FE model was therefore updated and the mesh was refined to compare the absolute stresses. The update resulted in an average margin of error of 37,9%. The two other methods used by the corporate partner were found to have an average margin of error of 11,5% and 13,4% using the FE model with the updated geometry and mesh. At increased pressure, the existing methods of representing the crimp joint is expected to result in a larger margin of error. However, the method used during the verification of the simulation methods were found to be invalid, but the invalid method is presumed to only have a minor effect on the presented margin of error. The existing methods are still concluded to be insufficiently representing the crimp joint.

As the margin of error was found to be large of the existing simulation methods of the crimp joint, a new method had to be developed. The development of the new simulation method was conducted through a case study where different methods of representing the crimp joint in the FE model was tested. The invalid method used during the verification was corrected and the developed method resulted in an average margin of error of 6,9%.

The aim of this thesis has been partly fulfilled as the margin of error of the existing FE simulation methods has been determined with an invalid method with small errors. However, the new simulation method has been developed with a lower margin of error using a valid method that can replace the existing simulation methods. This thesis could therefore result in minimized quality issues at both development and delivered products, leakage of toxic fluids, and material usage.

6.1   Future work

To continue the development of the FE simulation method of the crimp joint, the manufacturing process of the crimp joint needs to be simulated. If the yield limit of the brazed aluminium is found to be lower than the experimentally measured stresses, an elastic-plastic solver needs to be implemented in the FE software to comprehend the yielding that occurs at each pulsation. If the yielding then is found to have a low effect on the strains located at the outer bottom radius, a further study on the actual behaviour of the crimp joint needs to be conducted.

To strengthen the conclusions of this thesis, pressure pulsation in DAM conditions at lower pressures could be conducted. The results can then be used to verify the expected linear development of the stresses up to the pressure where the yielding occurs, which verifies the usage of the developed simulation method in the materials' elastic regions.

To increase the precision of experimental stress results, the quantity of specimens used to measure strain can be increased. Drawing general conclusions from only one controlled experiment can prove to be insufficient. The specimens should also be tested in a conditioned environment to study the crimp joint in its actual work environment. The method used to measure strain on the material can also be substituted for optical stress analysis. The optical method can be used to study the stresses on the radiator tank, which has been neglected in this thesis.

To generalize the developed method of representing the crimp joint through contact 12, a method with similar results as contact 12 can be developed using connection methods that are shared by different FEA softwares. In ANSYS Mechanical it can be conducted by representing the crimp joint with remote points with rigid or deformable behaviour.

7 REFERENCES

[1] "Strain Measurement Basics," *HBM*, Dec. 16, 2020.
https://www.hbm.com/en/6896/strain-measurement-basics/ (accessed Mar. 15, 2021).

[2] "Hooke's Law Explained," *HBM*, Oct. 07, 2020.
https://www.hbm.com/en/7114/hookes-law/ (accessed Mar. 15, 2021).

[3] "Experimental Stress Analysis (ESA) using Strain Gauges," *HBM*, Dec. 14, 2020.
https://www.hbm.com/en/7226/experimental-stress-analysis-using-strain-gauges/ (accessed Mar. 15, 2021).

[4] "What's a Strain Gage | KYOWA."
https://www.kyowa-ei.com/eng/technical/strainbasic_course/index.html (accessed Mar. 15, 2021).

[5] "Wheatstone Bridge Circuit | Strain Gauge," *HBM*, Dec. 02, 2020.
https://www.hbm.com/en/7163/wheatstone-bridge-circuit/ (accessed Mar. 15, 2021).

[6] "The Working Principle of a Compression Load Cell," *HBM*, Dec. 01, 2020.
https://www.hbm.com/en/7325/the-working-principle-of-a-compression-load-cell/ (accessed Mar. 22, 2021).

[7] "What Is Thermocouple Sensor and How Does It Work | Dewesoft."
https://dewesoft.com/daq/temperature-measurement-thermocouple-sensors (accessed Mar. 15, 2021).

[8] "Pressure Fatigue Tests - Impulse Test - Maximator Test, LLC," *Maximator Test*.
https://maximator-test.com/high-pressure-testing/impulse-test-pressure-fatigue-tests/ (accessed Mar. 22, 2021).

[9] "Nylon and Moisture Absorption | Amco Polymers."
https://www.amcopolymers.com/resources/blog/nylon-and-moisture-absorption (accessed Mar. 23, 2021).

[10] "What Is FEA | Finite Element Analysis? Documentation," *SimScale*.
https://www.simscale.com/docs/simwiki/fea-finite-element-analysis/what-is-fea-finite-element-analysis/ (accessed May 27, 2021).

[11] "Ansys Mechanical | Structural FEA Analysis Software."
https://www.ansys.com/products/structures/ansys-mechanical (accessed May 27, 2021).

[12] "Implicit vs. Explicit FEM: What Is the Difference?," *SimScale*, Jan. 08, 2019.
https://www.simscale.com/blog/2019/01/implicit-vs-explicit-fem/ (accessed May 28, 2021).

[13] P. Robin Roy, V. Hariram, and M. Subramanian, "PROBABILISTIC FINITE ELEMENT ANALYSIS OF A HEAVY DUTY RADIATOR UNDER INTERNAL PRESSURE LOADING," *Journal of engineering science & technology*, vol. 12, no. 9, pp. 2438–2452, Sep. 2017.

[14] S. Mao, C. Cheng, X. Li, and E. E. Michaelides, "Thermal/structural analysis of radiators for heavy-duty trucks," *Applied Thermal Engineering*, vol. 30, no. 11, pp. 1438–1446, Aug. 2010, doi: 10.1016/j.applthermaleng.2010.03.003.

[15] R. Schouwenaars, S. Cerrud, and A Ortiz, "Mechanical analysis of fracture in an automotive radiator head produced from a nylon–glass fibre composite," *Composites Part A: Applied Science*

and Manufacturing, vol. 33, no. 4, pp. 551–558, Apr. 2002, doi: 10.1016/S1359-835X(01)00143-9.

[16] S. Zike and L. P. Mikkelsen, "Correction of Gauge Factor for Strain Gauges Used in Polymer Composite Testing," *Exp Mech*, vol. 54, no. 3, pp. 393–403, Mar. 2014, doi: 10.1007/s11340-013-9813-7.

[17] "Strain gauge installation on fiber-reinforced plastics," *HBM*, Oct. 07, 2020. https://www.hbm.com/en/3180/tips-and-tricks-strain-gage-installation-on-fiber-reinforced-plastics/ (accessed Mar. 16, 2021).

[18] M. De Monte, E. Moosbrugger, and M. Quaresimin, "Influence of temperature and thickness on the off-axis behaviour of short glass fibre reinforced polyamide 6.6 – Quasi-static loading," *Composites Part A: Applied Science and Manufacturing*, vol. 41, no. 7, pp. 859–871, Jul. 2010, doi: 10.1016/j.compositesa.2010.02.018.

Header tab numbering goes from outlet to inlet. Inlet side is positioned on passanger side and outlet side is positioned on driver side.
The radiator has 42 tabs in a row.

| Point	Quantity	Position	Inlet/ outlet	Engine/ Grill side	Header tab no	Name	Glue Supplier	Strain gauge type	Gauge factor	Gauge resistance	Batch	Distance Y (mm)	Distance Z (mm)	Resistance after mounting	Resistance at the connector
1	Strain	Top radius	Outlet	Engine side	3	SG01_TRE_3	HBM	KFGS-1-120-C1-23N15C2	2,11	120	001B	12,6	12,8	120,0	123,3
2	Strain	Top radius	Outlet	Engine side	6	SG02_TRE_6	HBM	KFGS-1-120-C1-23N15C2	2,11	120	001B	12,4	13,3	119,9	122,6
3	Strain	Outer radius	Outlet	Engine side	3	SG03_ORE_3	HBM	KFGS-1-120-C1-23N15C2	2,11	120	001B	12,7	12,8	120,0	123,4
4	Strain	Outer radius	Outlet	Engine side	4.5	SG04_ORE_4.5	HBM	KFGS-1-120-C1-23N15C2	2,11	120	001B	8,9	3,6	119,8	122,5
5	Strain	Outer radius	Outlet	Engine side	6	SG05_ORE_6	HBM	KFGS-1-120-C1-23N15C2	2,11	120	001B	12,6	13,3	119,8	122,1
6	Strain	Outer radius	Outlet	Engine side	7.5	SG06_ORE_7.5	HBM	KFGS-1-120-C1-23N15C2	2,11	120	001B	9,4	3,1	119,7	122,4
7	Strain	Top radius	Outlet	Grill side	3	SG07_TRG_3	Kyowa	KFGS-1-120-C1-23N15C2	2,11	120	001B	12,7	12,5	120,0	123,0
8	Strain	Top radius	Outlet	Grill side	6	SG08_TRG_6	HBM	KFGS-1-120-C1-23N15C2	2,11	120	001B	12,6	11,9	119,8	122,6
9	Strain	Outer radius	Outlet	Grill side	3	SG09_ORG_3	HBM	KFGS-1-120-C1-23N15C2	2,11	120	001B	12,0	12,4	119,8	122,5
10	Strain	Outer radius	Outlet	Grill side	4.5	SG10_ORG_4.5	HBM	KFGS-1-120-C1-23N15C2	2,11	120	001B	8,8	2,9	119,7	122,6
11	Strain	Outer radius	Outlet	Grill side	6	SG11_ORG_6	HBM	KFGS-1-120-C1-23N15C2	2,11	120	001B	12,3	12,0	119,9	122,8
12	Strain	Outer radius	Outlet	Grill side	7.5	SG12_ORG_7.5	HBM	KFGS-1-120-C1-23N15C2	2,11	120	001B	8,8	2,2	119,7	123,2
13	Strain	Top radius	Outlet	Engine side	18	SG13_TRE_18	HBM	KFGS-1-120-C1-23N15C2	2,11	120	001B	11,9	12,4	119,7	123,4
14	Strain	Top radius	Outlet	Engine side	21	SG14_TRE_21	HBM	KFGS-1-120-C1-23N15C2	2,11	120	001B	11,7	12,3	119,9	123,4
15	Strain	Outer radius	Outlet	Engine side	18	SG15_ORE_18	HBM	KFGS-1-120-C1-23N15C2	2,11	120	001B	12,9	12,7	119,9	123,3
16	Strain	Outer radius	Outlet	Engine side	19.5	SG16_ORE_19.5	HBM	KFGS-1-120-C1-23N15C2	2,11	120	001B	9,4	2,8	119,6	123,0
17	Strain	Outer radius	Outlet	Engine side	21	SG17_ORE_21	HBM	KFGS-1-120-C1-23N15C2	2,11	120	001B	12,7	12,5	119,9	123,4
18	Strain	Outer radius	Outlet	Engine side	22.5	SG18_ORE_22.5	HBM	KFGS-1-120-C1-23N15C2	2,11	120	001B	9,5	2,8	119,9	123,4
19	Strain	Top radius	Outlet	Grill side	18	SG19_TRG_18	Kyowa	KFGS-1-120-C1-23N15C2	2,12	120	0,27A	12,3	12,2	119,7	122,9
20	Strain	Top radius	Outlet	Grill side	21	SG20_TRG_21	Kyowa	KFGS-1-120-C1-23N15C2	2,12	120	0,27A	12,2	12,4	119,5	123,6
21	Strain	Outer radius	Outlet	Grill side	18	SG21_ORG_18	Kyowa	KFGS-1-120-C1-23N15C2	2,12	120	0,27A	13,1	11,9	119,5	122,8
22	Strain	Outer radius	Outlet	Grill side	19.5	SG22_ORG_19.5	Kyowa	KFGS-1-120-C1-23N15C2	2,12	120	0,27A	8,6	2,2	119,7	122,8
23	Strain	Outer radius	Outlet	Grill side	21	SG23_ORG_21.1	Kyowa	KFGS-1-120-C1-23N30C2	2,10	120	0,29B	0	12,0	120,0	123,8
24	Strain	Outer radius	Outlet	Grill side	21	SG24_ORG_21.2	Kyowa	KFGS-1-120-C1-23N30C2	2,10	120	0,29B	13,2	12,0	119,8	123,9
25	Strain	Outer radius	Outlet	Grill side	21	SG25_ORG_21.3	Kyowa	KFGS-1-120-C1-23N30C2	2,10	120	0,29B	11,1	12,0	119,7	122,9
26	Strain	Outer radius	Outlet	Grill side	21	SG26_ORG_21.4	Kyowa	KFGS-1-120-C1-23N30C2	2,10	120	0,29B	9,4	12,0	119,9	123,0
27	Strain	Outer radius	Outlet	Grill side	21	SG27_ORG_21.5	Kyowa	KFGS-1-120-C1-23N30C2	2,10	120	0,29B	6,8	12,0	119,9	123,8
28	Strain	Outer radius	Outlet	Grill side	22.5	SG28_ORG_22.5	Kyowa	KFGS-1-120-C1-23N15C2	2,12	120	0,27A	8,2	2,2	119,2	122,5
30	Temp	Header wall	Outlet	Engine side	5	TC01_HE_5								
31	Temp	Header wall	Outlet	Grill side	5	TC02_HG_5								
32	Temp	Header wall	Outlet	Engine side	20	TC03_HE_20								
33	Temp	Header wall	Outlet	Grill side	20	TC04_HG_20								
34	Temp	Tank	Outlet	Engine side	5	TC05_TE_5								
35	Temp	Tank tab	Outlet	Engine side	5.5	TC06_TTE_5.5								
36	Temp	Tank	Outlet	Engine side	20	TC07_TE_20								
37	Temp	Tank tab	Outlet	Engine side	20.5	TC08_TTE_20.5								
38	Temp		Inlet			Inlet_temp								

Figure 8-1: Overview of instrumentation.
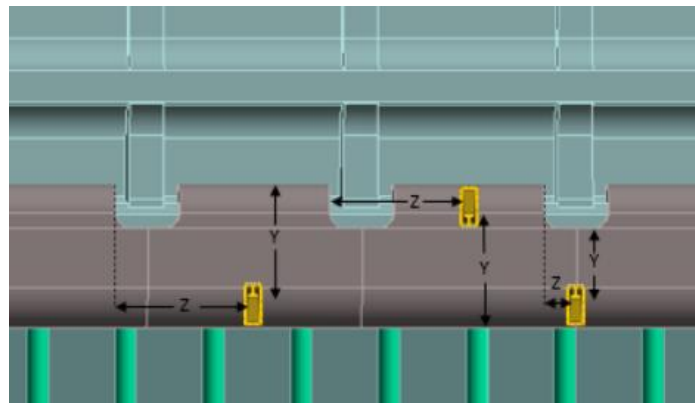
Figure 8-2: How the placement of the strain gauges was measured depending on the mounting position. Header tab number is counted from left to right.
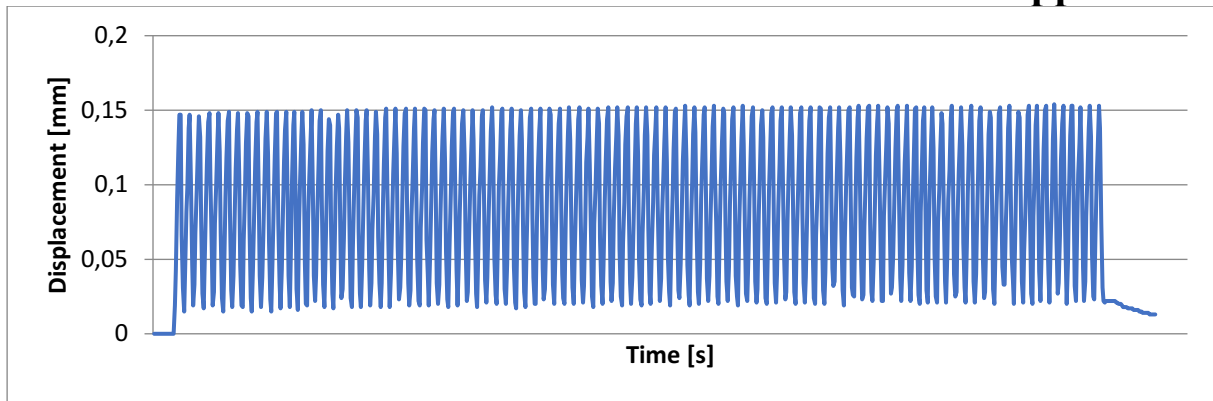
Figure 8-3: Displacement of the header wall positioned at the outlet section, at the load of 100 kPa.
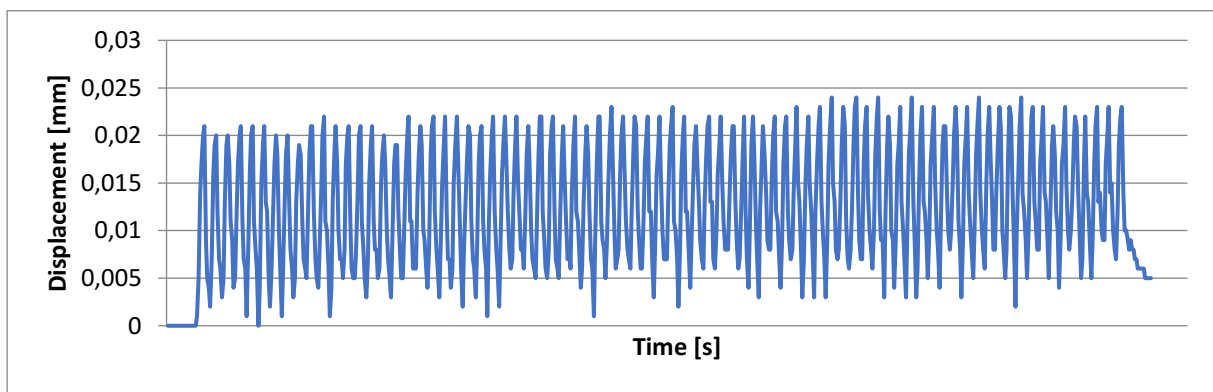

Figure 8-4: Displacement of the header tab positioned at the grill side of the outlet section, at the load of 100 kPa.
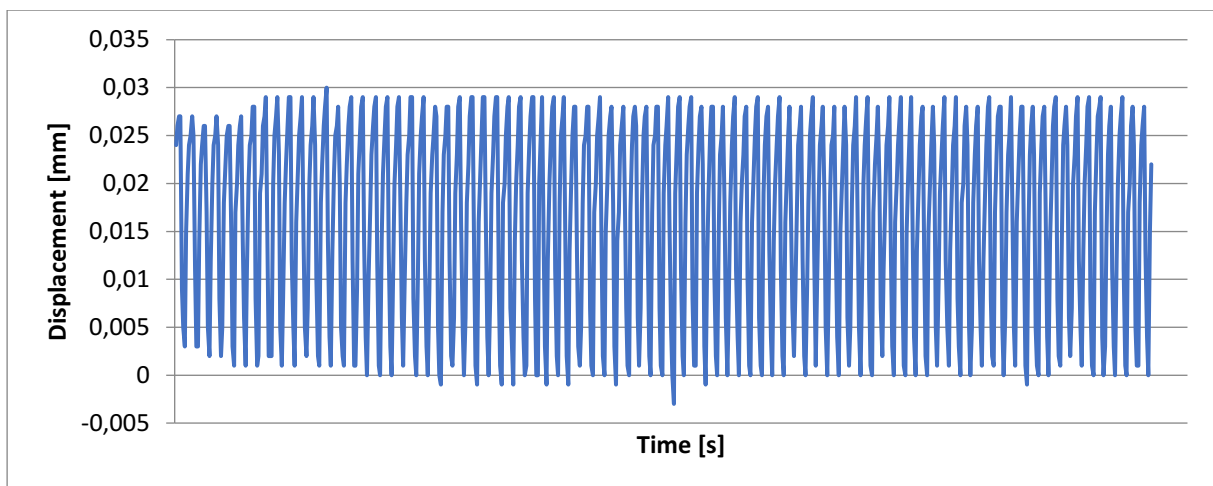

Figure 8-5: Displacement of the header tab positioned at the engine side of the outlet section, at the load of 100 kPa.
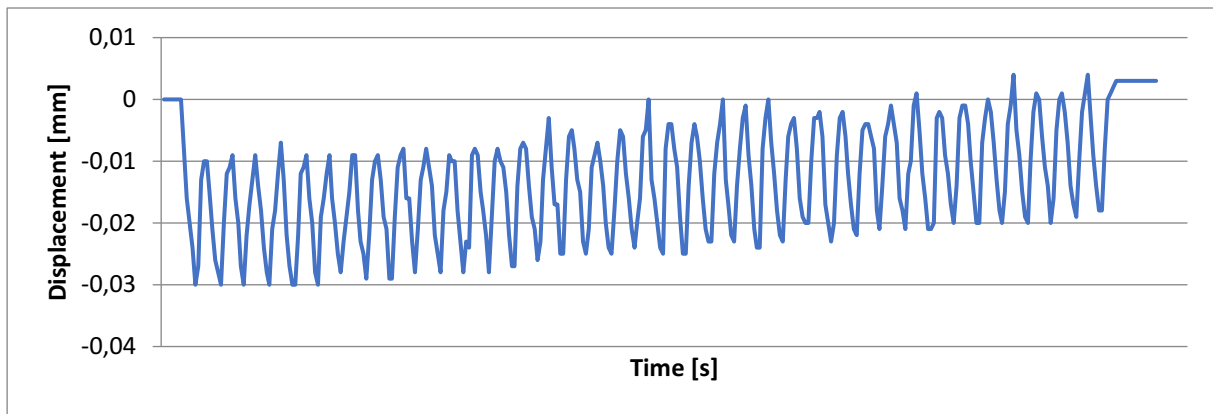
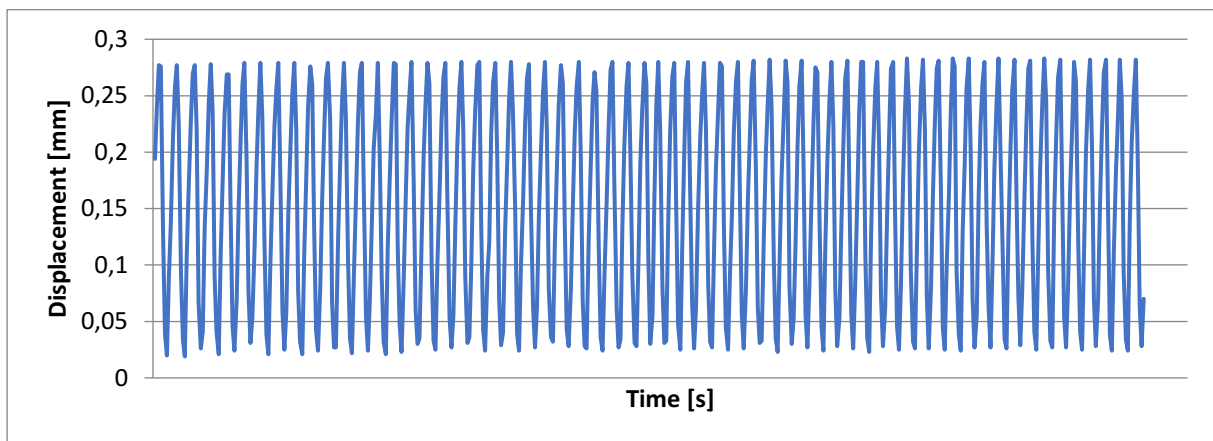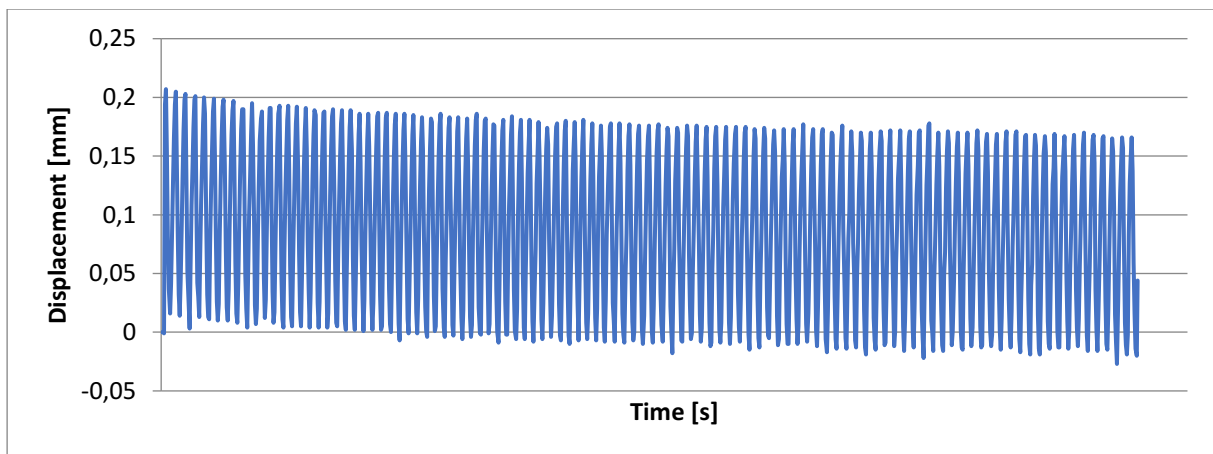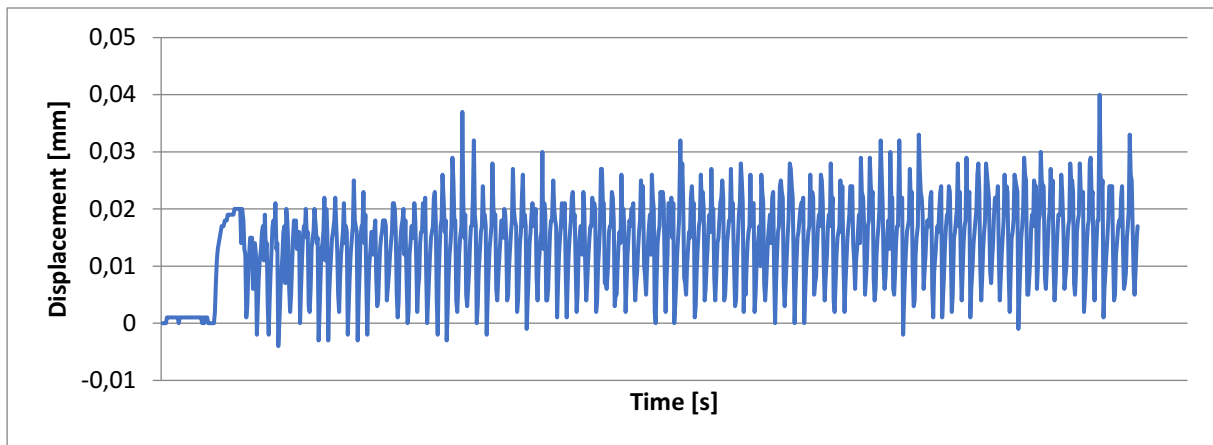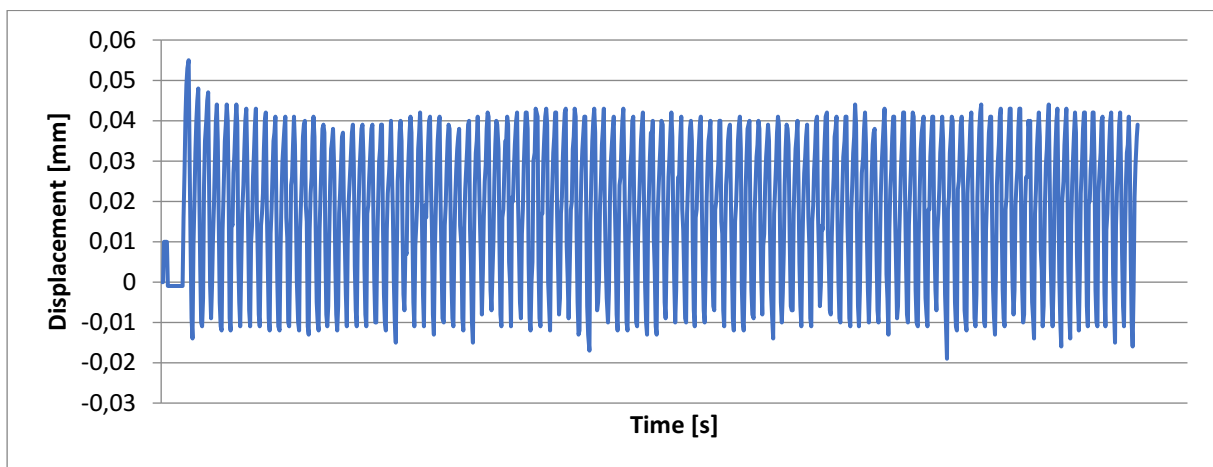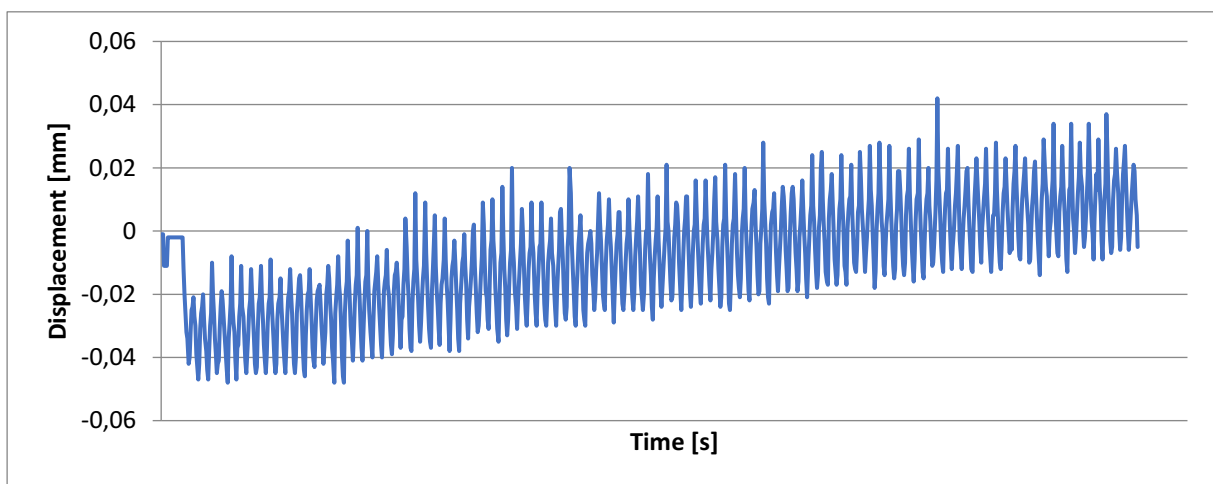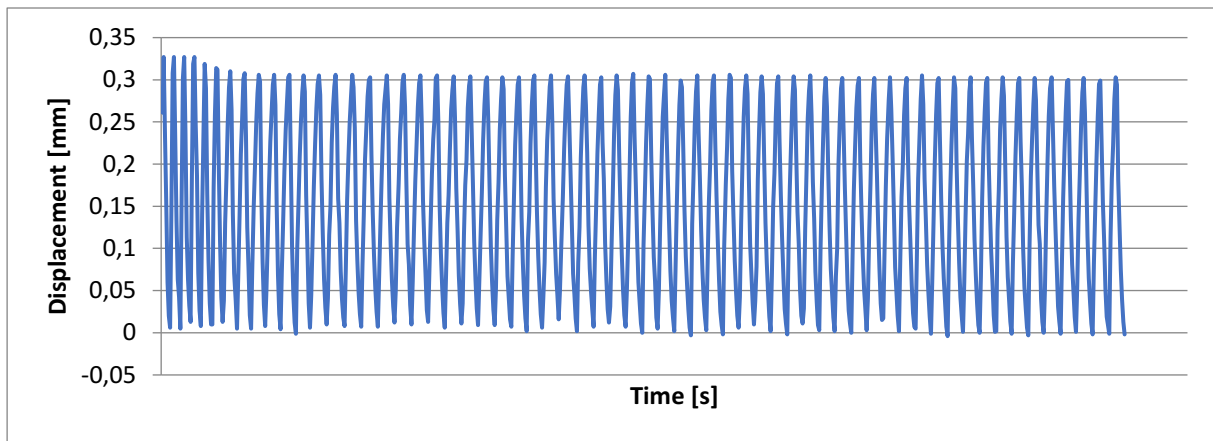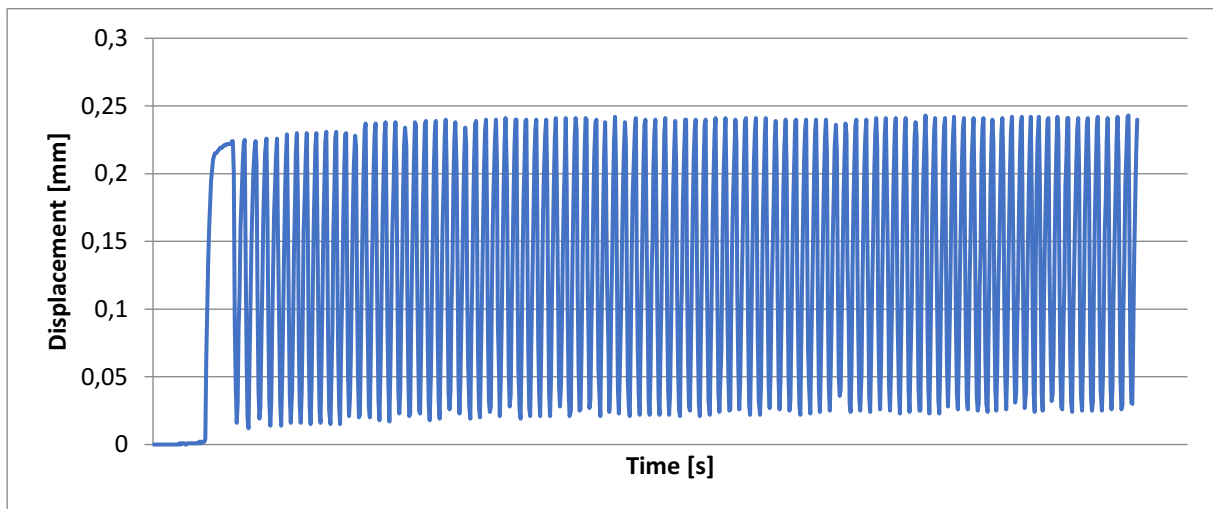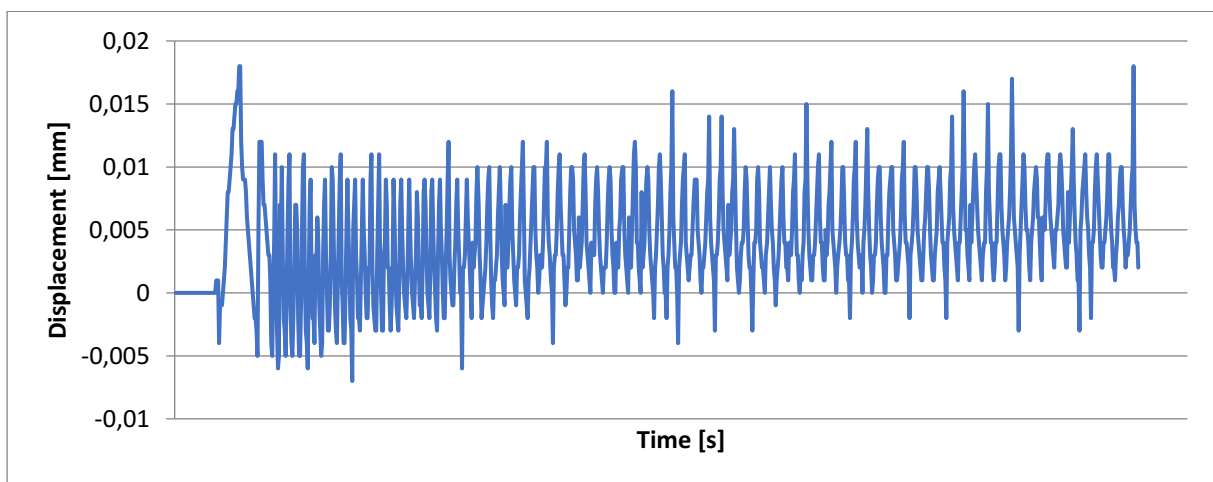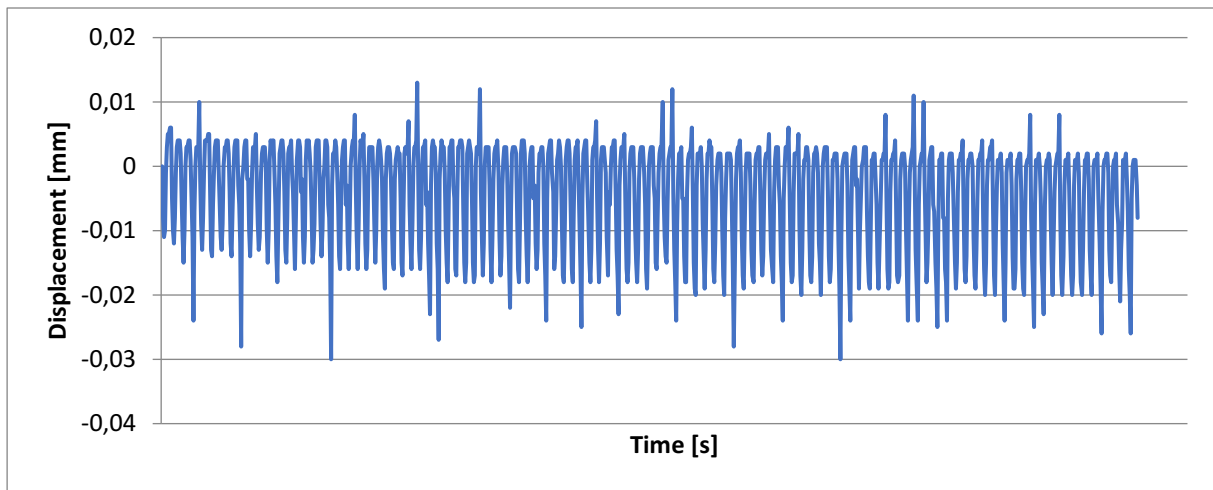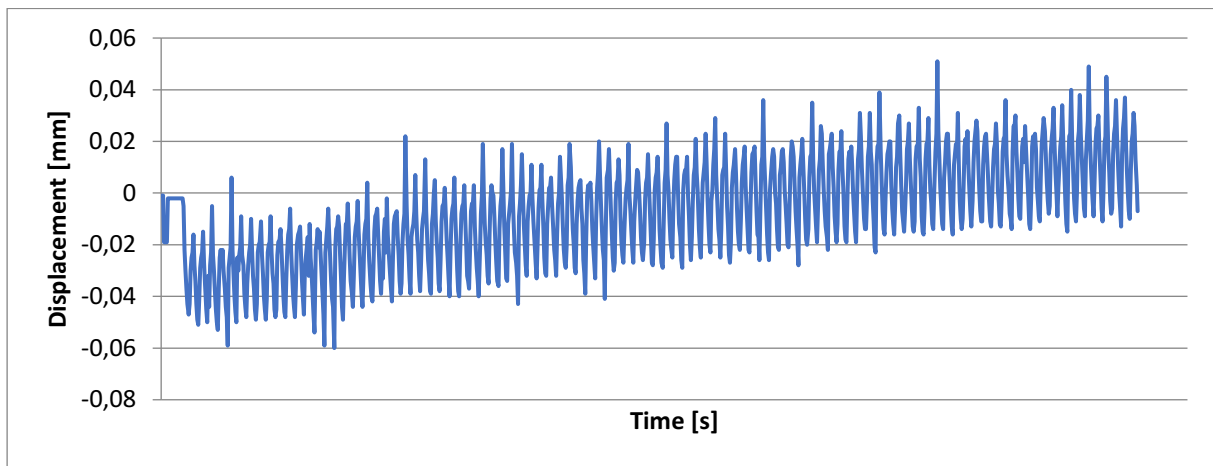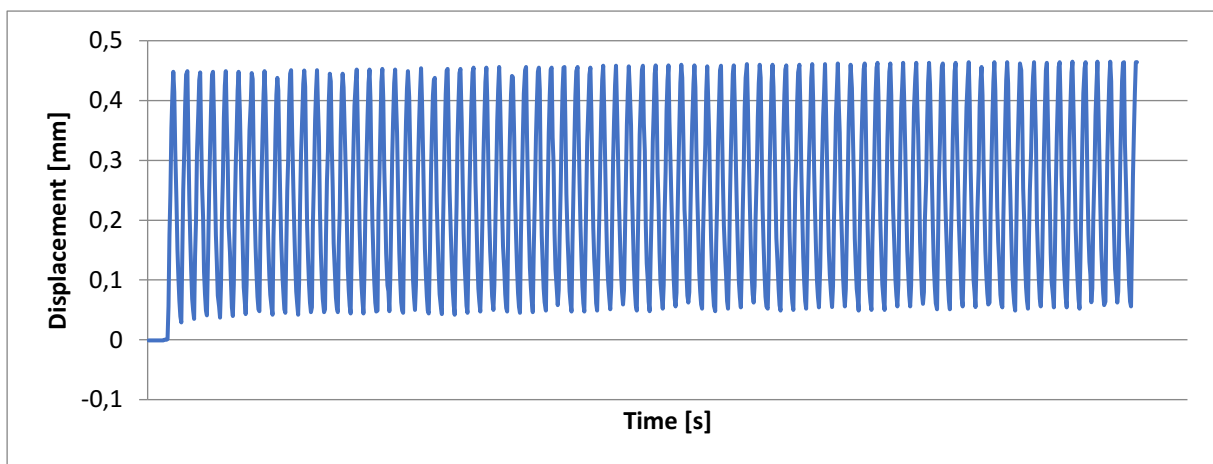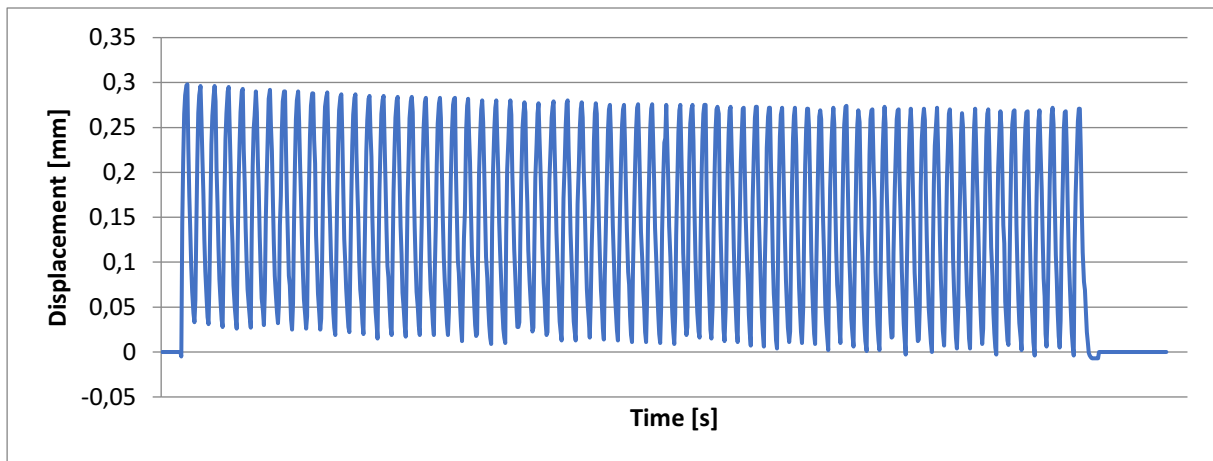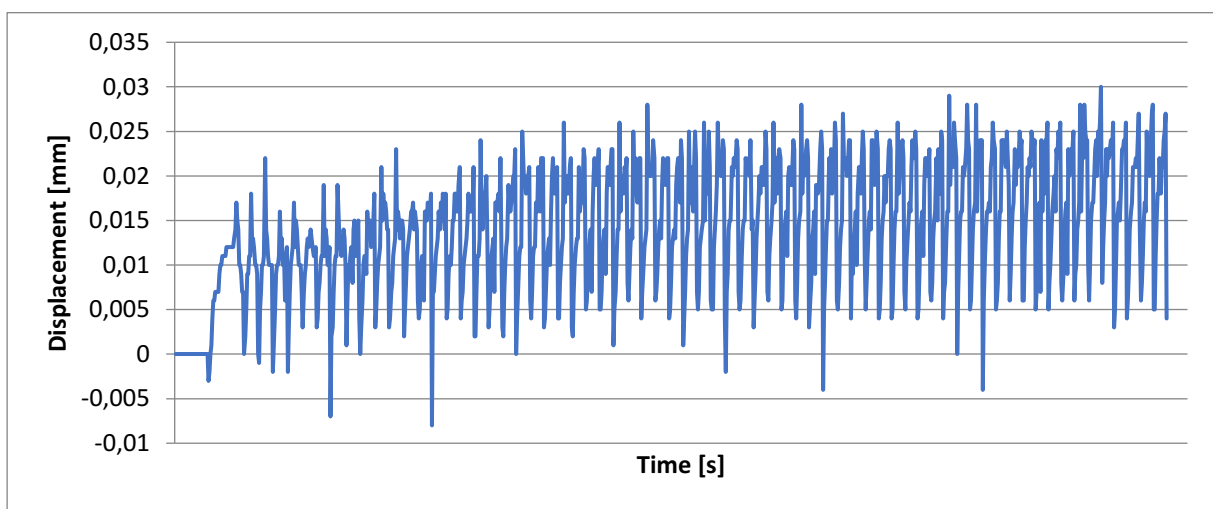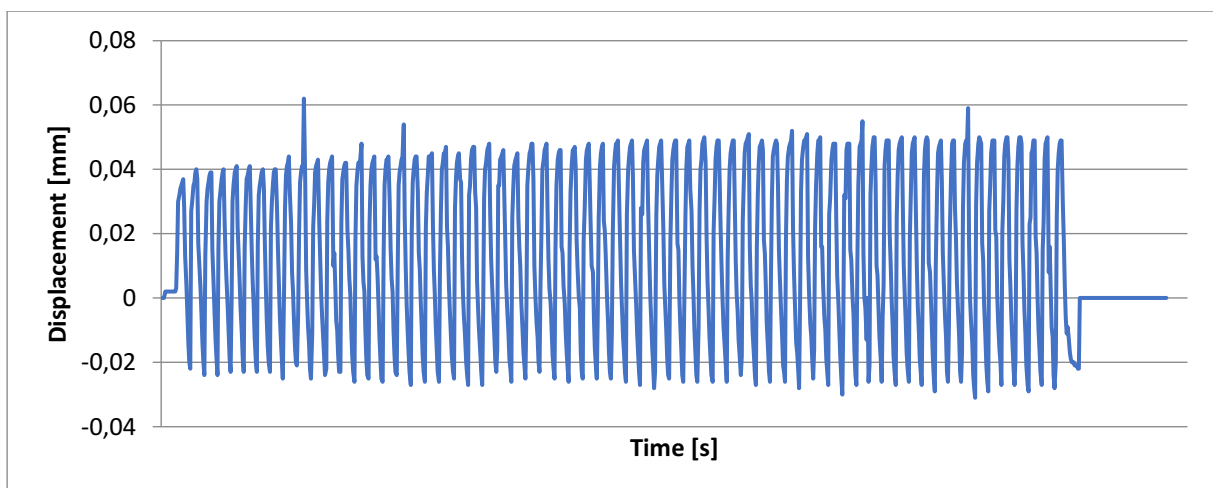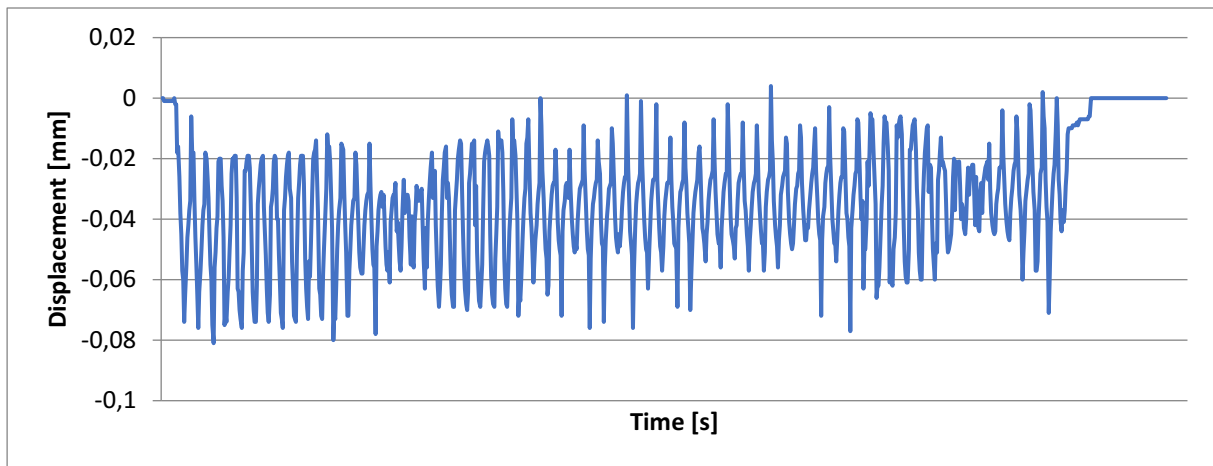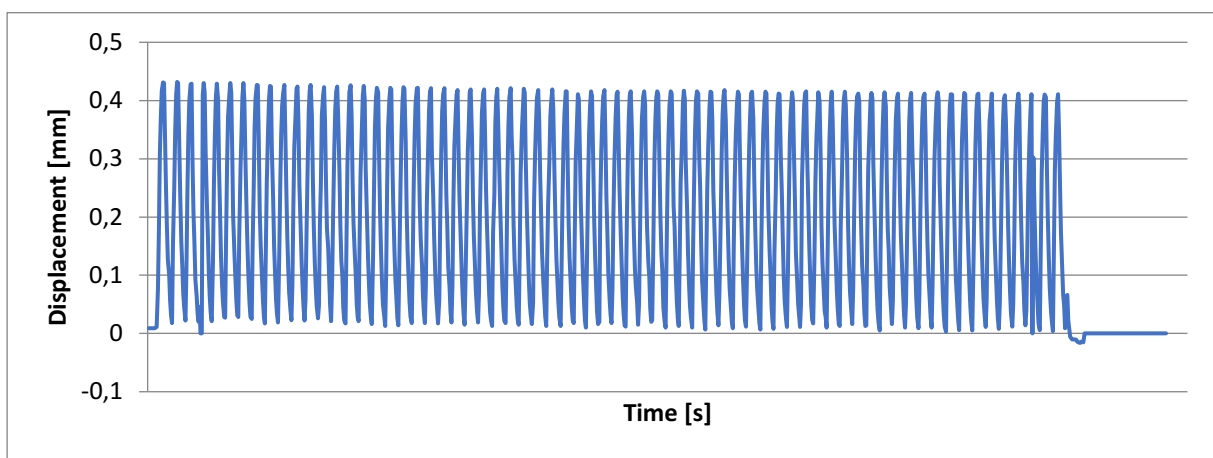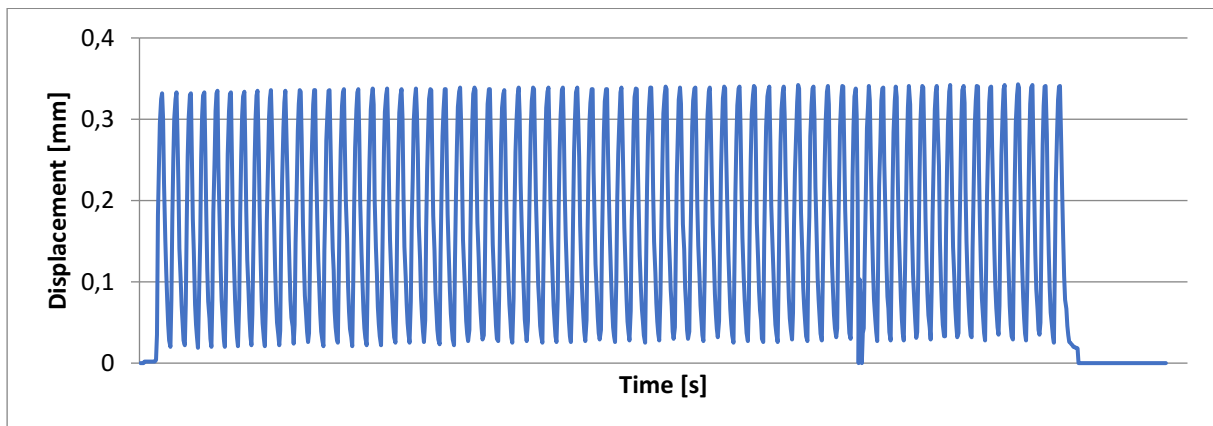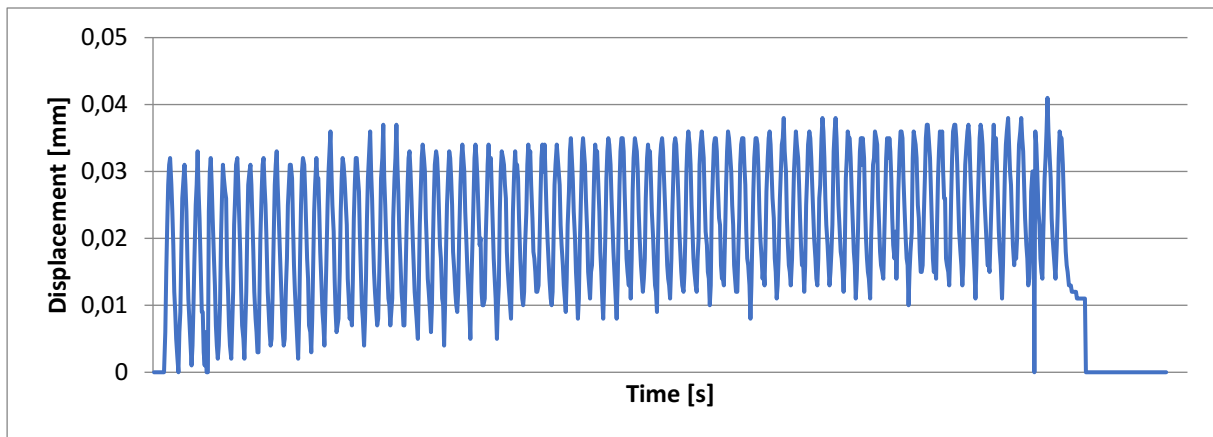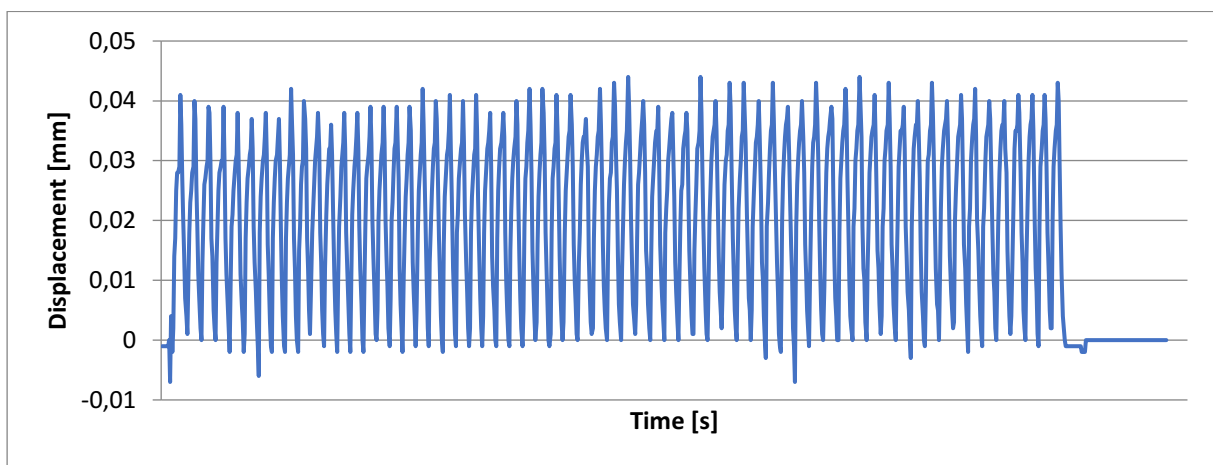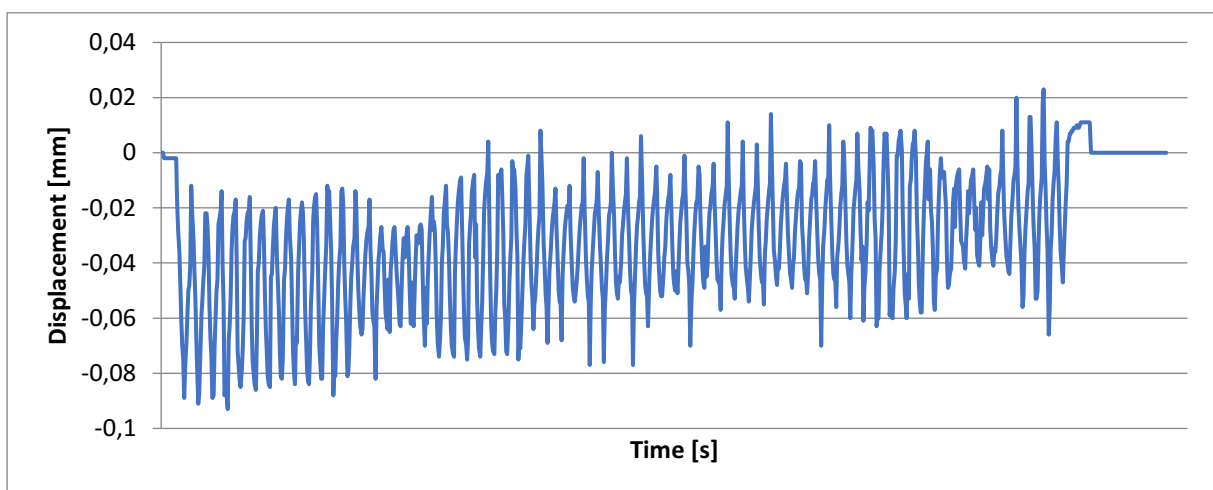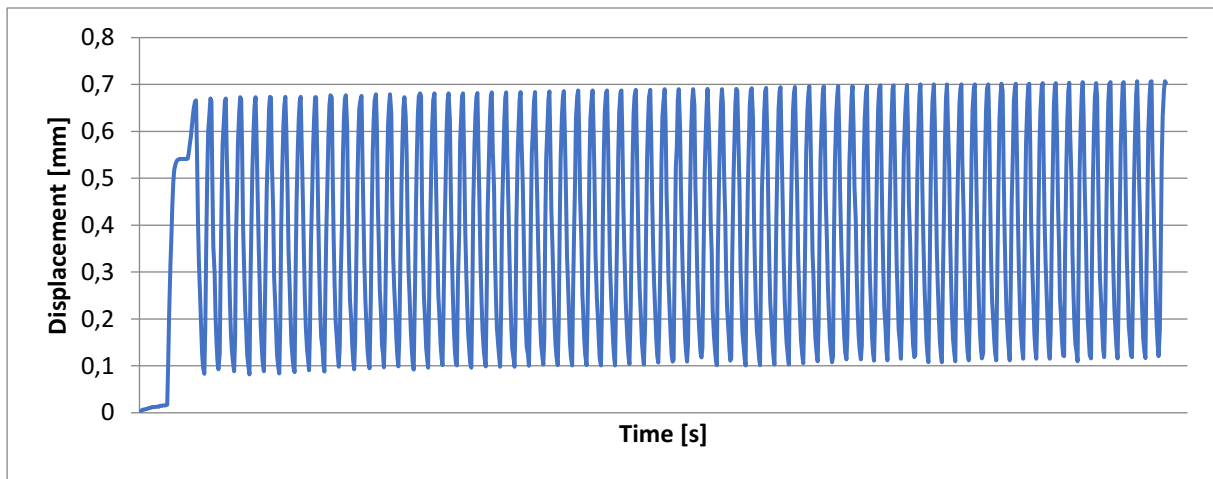Figure 8-6: Displacement of the tank top positioned at the outlet section, at the load of 100 kPa.

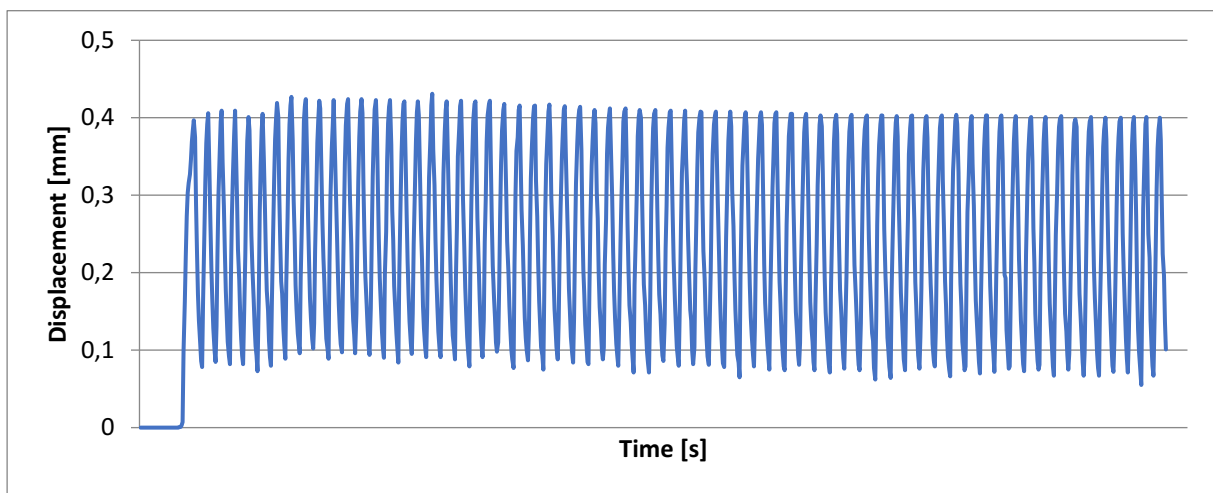Figure 8-7: Displacement of the tank wall positioned at the outlet middle section, at the load of 100 kPa.

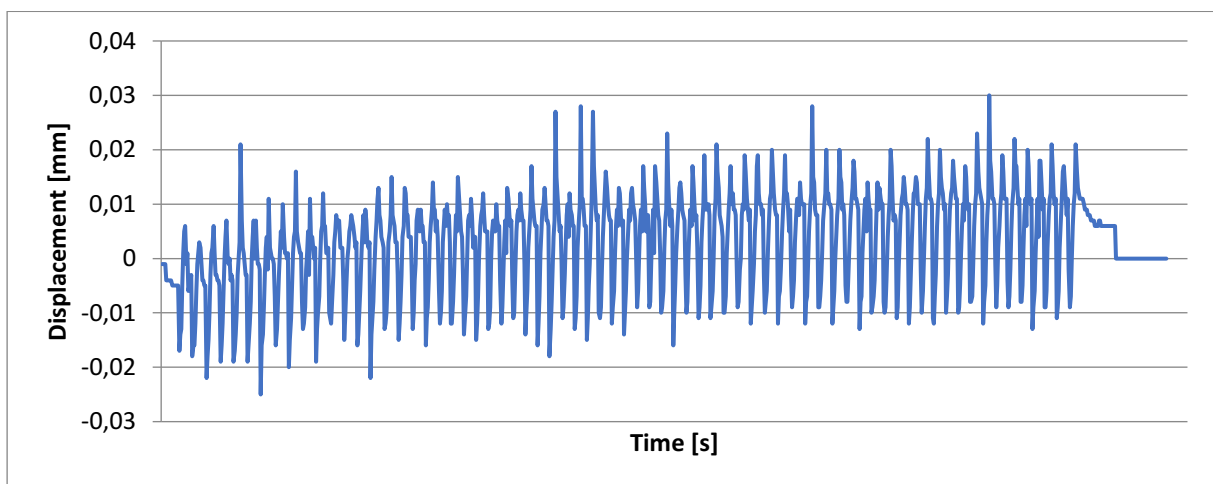Figure 8-8: Displacement of the header wall positioned at the middle section, at the load of 160 kPa.

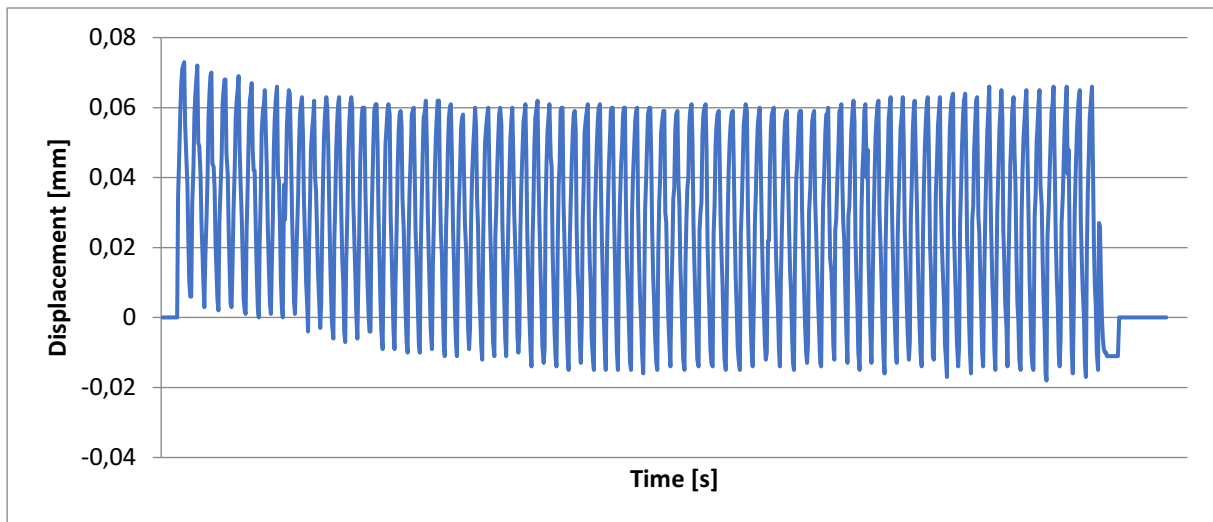Figure 8-9: Displacement of the header tab positioned at the grill side of the middle section, at the load of 160 kPa.

Figure 8-10: Displacement of the header tab positioned at the engine side of the middle section, at the load of 160 kPa.
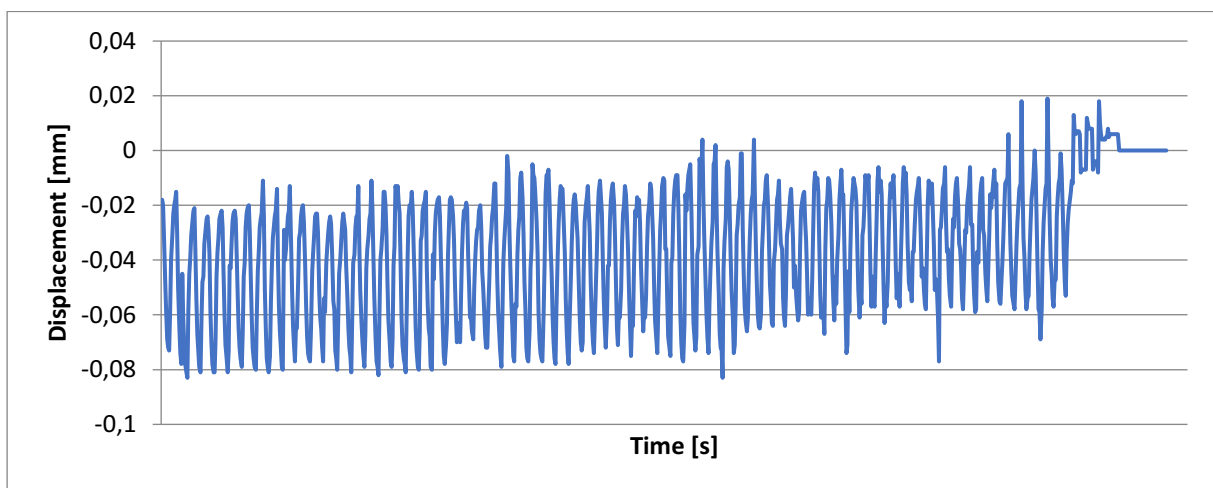

Figure 8-11: Displacement of the tank top positioned at the middle section, at the load of 160 kPa.
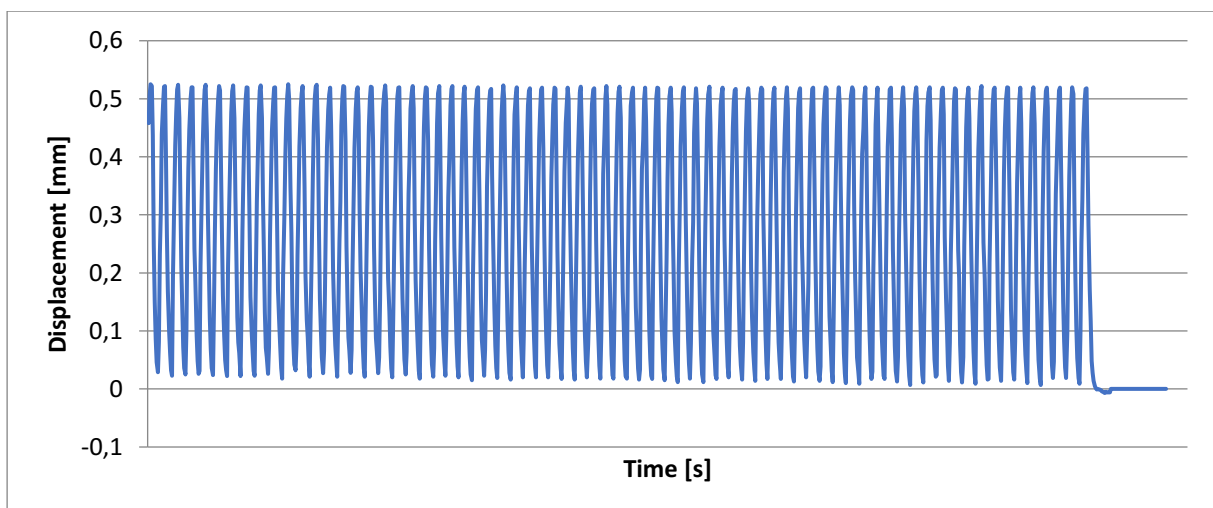
Figure 8-12: Displacement of the tank wall positioned at the middle section, at the load of 160 kPa.
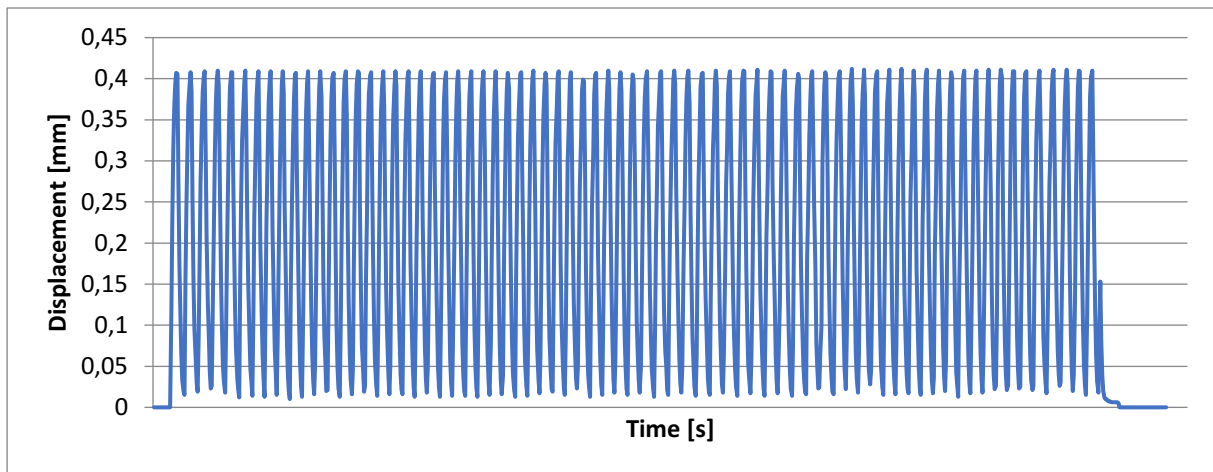

Figure 8-13: Displacement of the header wall positioned at the outlet section, at the load of 160 kPa.

Figure 8-14: Displacement of the header tab positioned at the grill side of the outlet section, at the load of 160 kPa.

Figure 8-15: Displacement of the header tab positioned at the engine side of the outlet section, at the load of 160 kPa.

Figure 8-16: Displacement of the tank top positioned at the outlet section, at the load of 160 kPa.

Figure 8-17: Displacement of the tank wall positioned at the outlet section, at the load of 160 kPa.

Figure 8-18: Displacement of the header wall positioned at the middle section, at the load of 220 kPa.

Figure 8-19: Displacement of the header tab positioned at the grill side of the middle section, at the load of 220 kPa.

Figure 8-20: Displacement of the header tab positioned at the engine side of the middle section, at the load of 220 kPa.

Figure 8-21: Displacement of the tank top positioned at the middle section, at the load of 220 kPa.

Figure 8-22: Displacement of the tank wall positioned at the middle section, at the load of 220 kPa.

Figure 8-23: Displacement of the header wall positioned at the outlet section, at the load of 220 kPa.
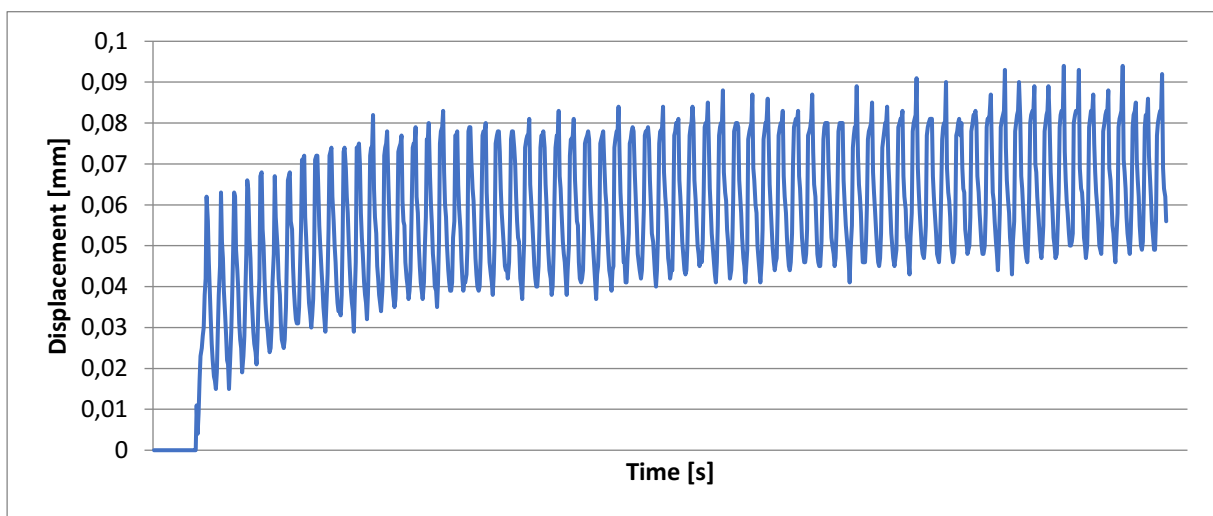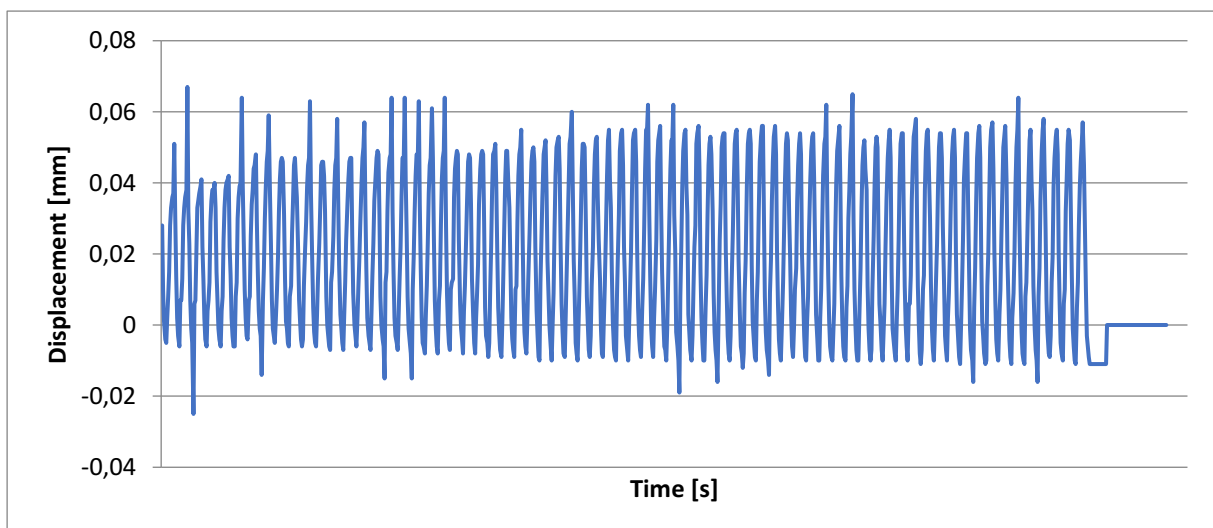
Figure 8-24: Displacement of the header tab positioned at the grill side of the outlet section, at the load of 220 kPa.

Figure 8-25: Displacement of the header tab positioned at the engine side of the outlet section, at the load of 220 kPa.
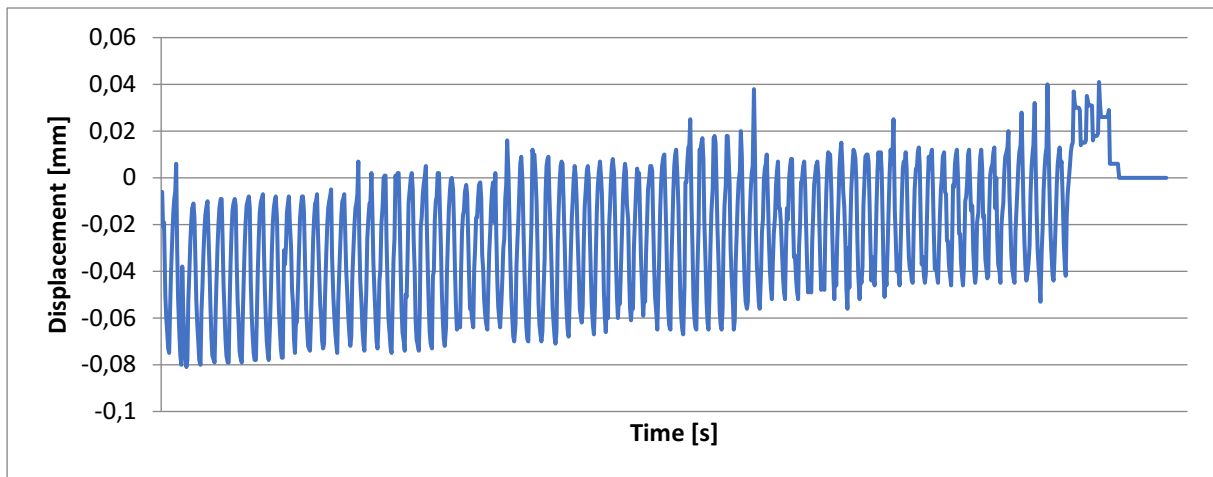

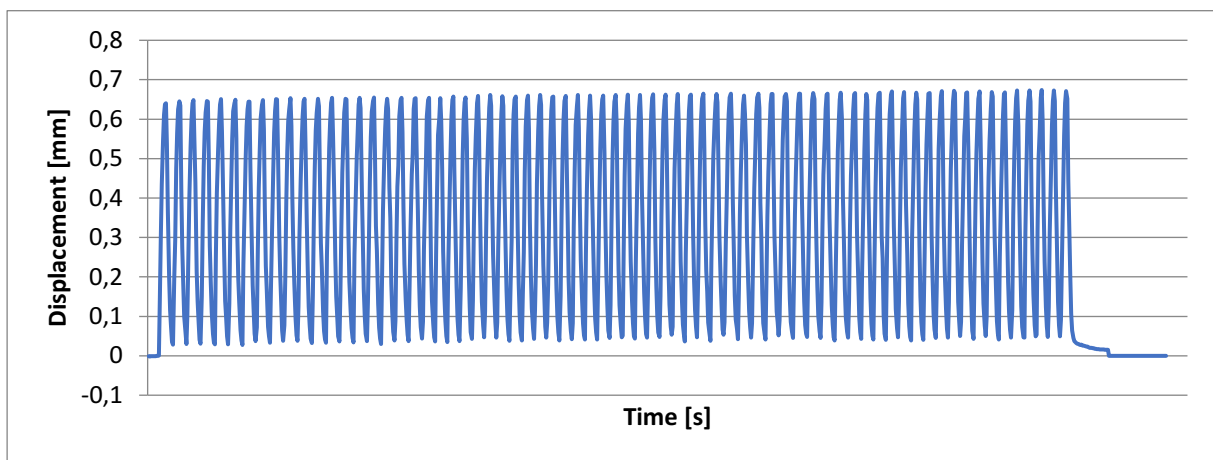Figure 8-26: Displacement of the tank top positioned at the outlet section, at the load of 220 kPa.

Figure 8-27: Displacement of the tank wall positioned at the outlet section, at the load of 220 kPa.


Figure 8-28: Displacement of the header wall positioned at the middle section, at the load of 260 kPa.

Figure 8-29: Displacement of the header tab positioned at the grill side of the middle section, at the load of 260 kPa.

Figure 8-30: Displacement of the header tab positioned at the engine side of the middle section, at the load of 260 kPa.

Figure 8-31: Displacement of the tank top positioned at the middle section, at the load of 260 kPa.

Figure 8-32: Displacement of the tank wall positioned at the middle section, at the load of 260 kPa.

Figure 8-33: Displacement of the header wall positioned at the outlet section, at the load of 260 kPa.

Figure 8-34: Displacement of the header tab positioned at the grill side of the outlet section, at the load of 260 kPa.

Figure 8-35: Displacement of the header tab positioned at the engine side of the outlet section, at the load of 260 kPa.

Figure 8-36: Displacement of the tank top positioned at the outlet section, at the load of 260 kPa.

Figure 8-37: Displacement of the tank wall positioned at the outlet section, at the load of 260 kPa.
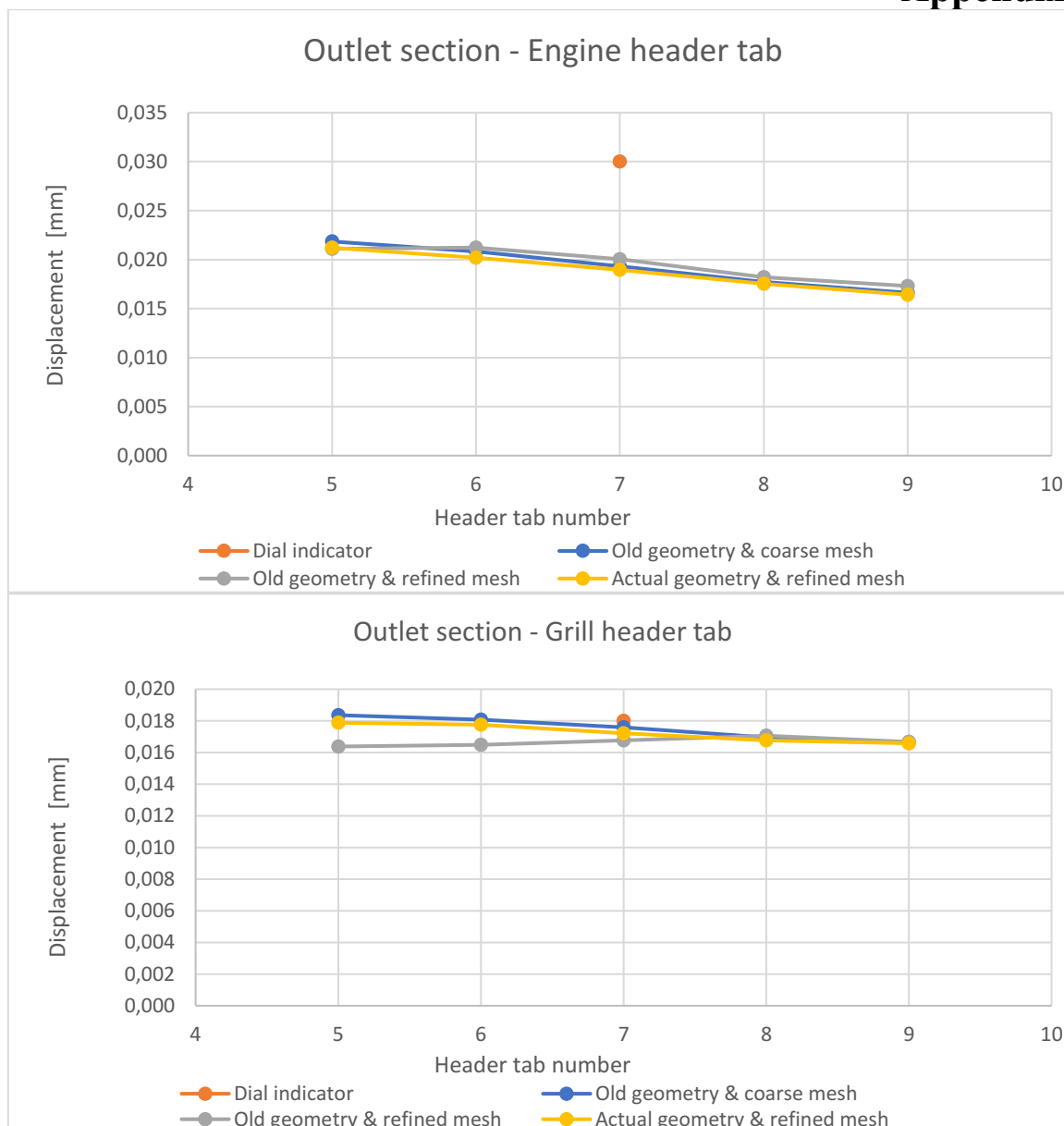
Figure 8-38: Displacement of header tabs at outlet section.
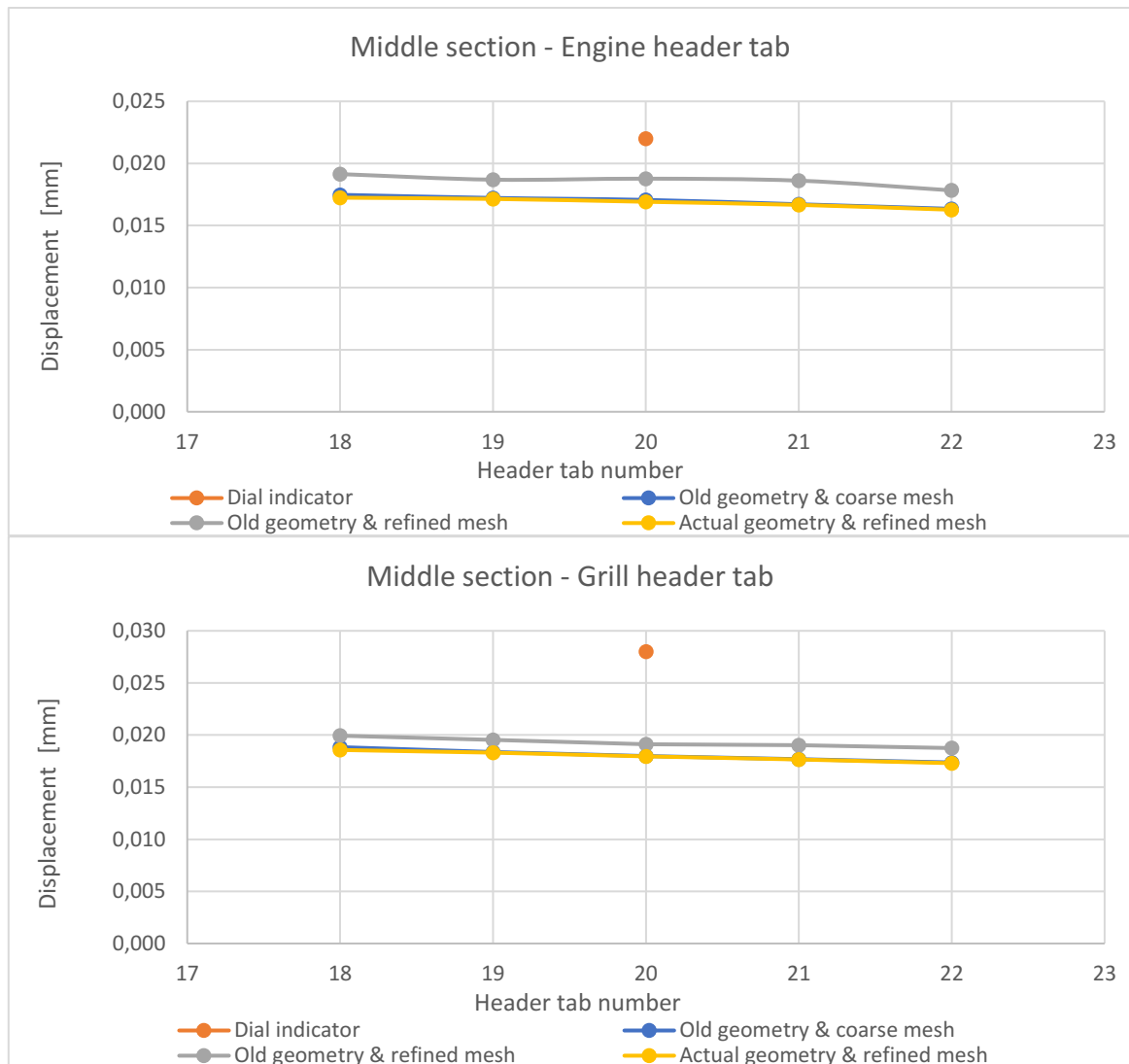
Figure 8-39: Displacement of header tabs at the middle section.
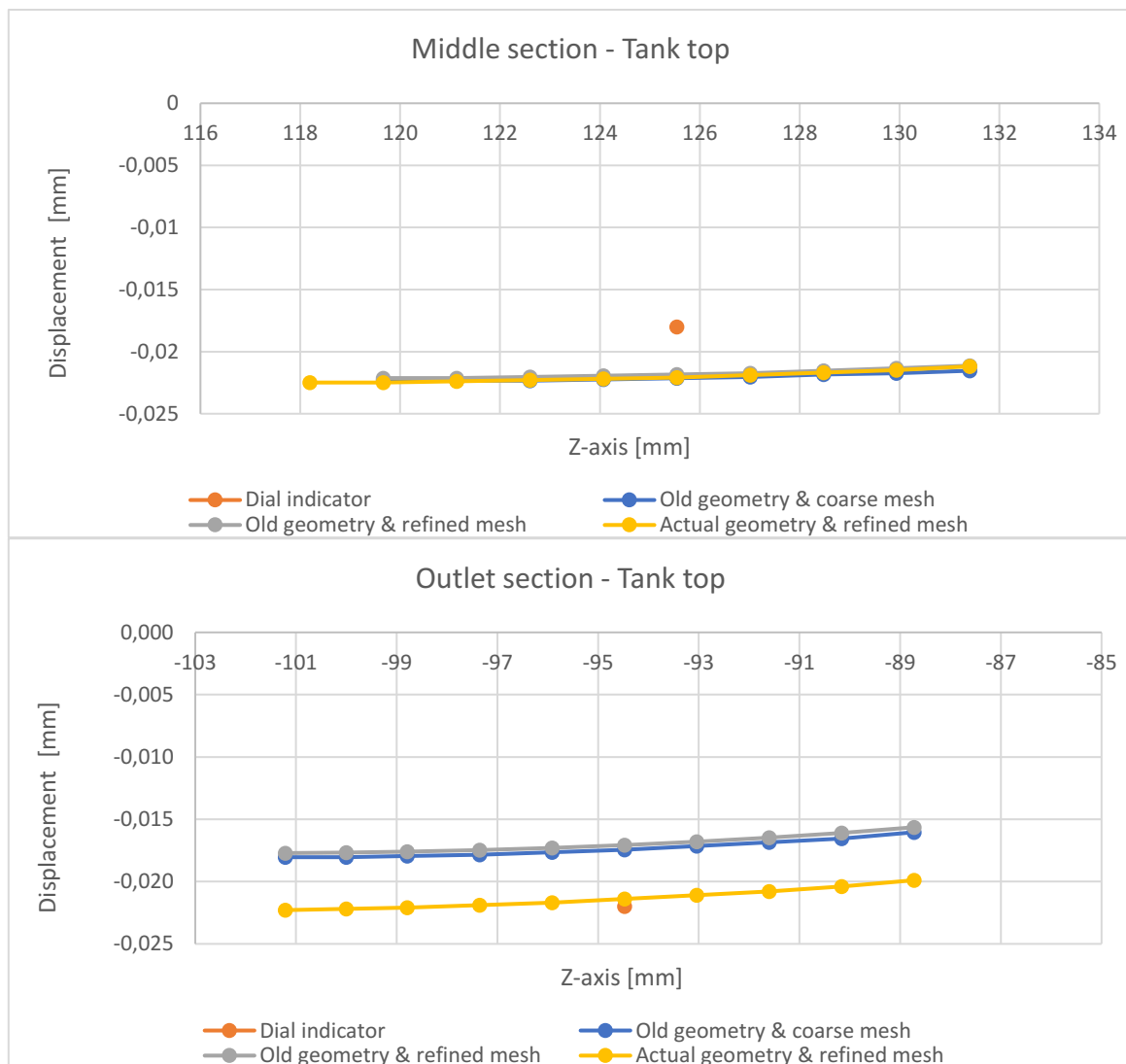
Figure 8-40: Displacement of tank top.
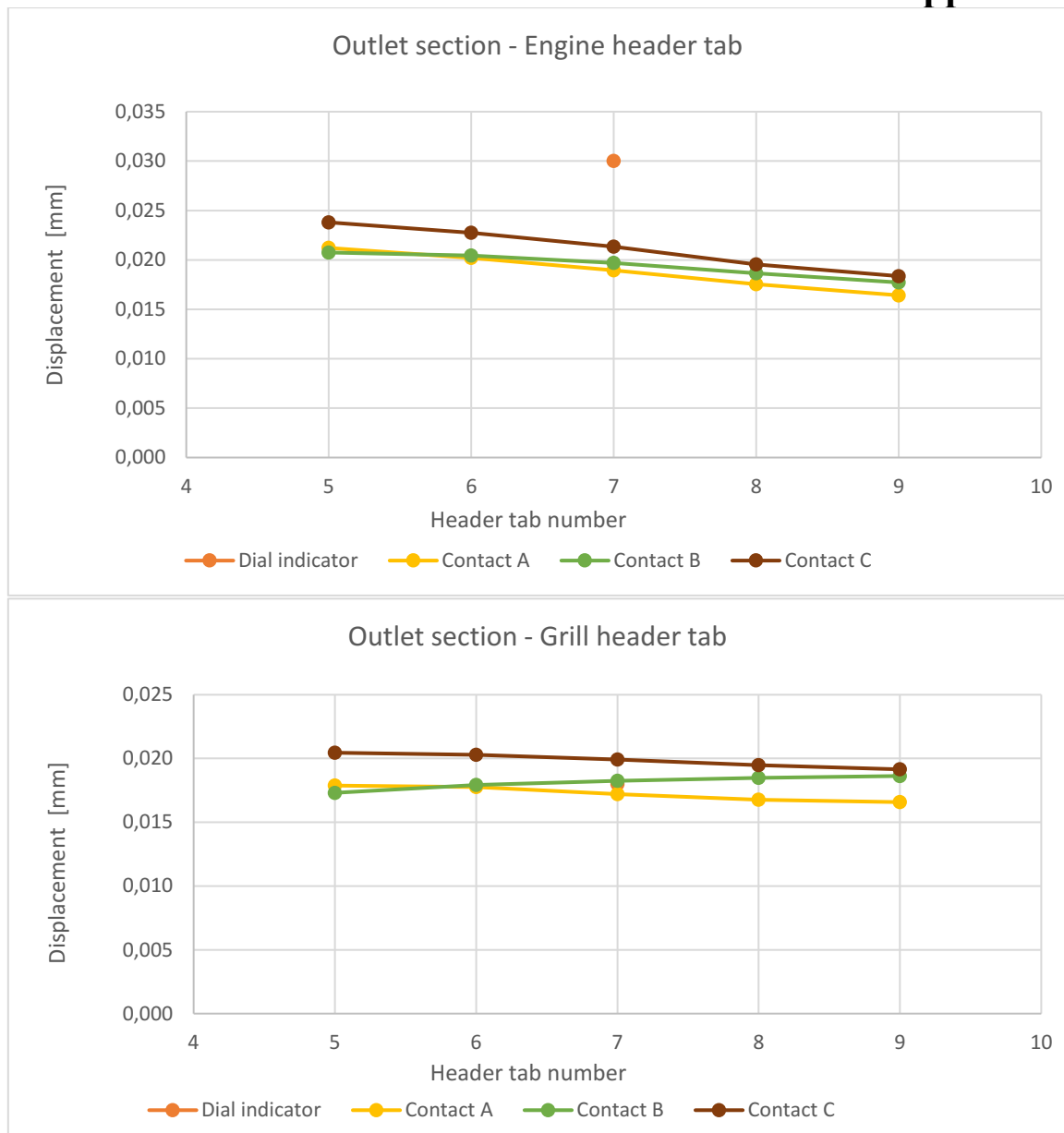
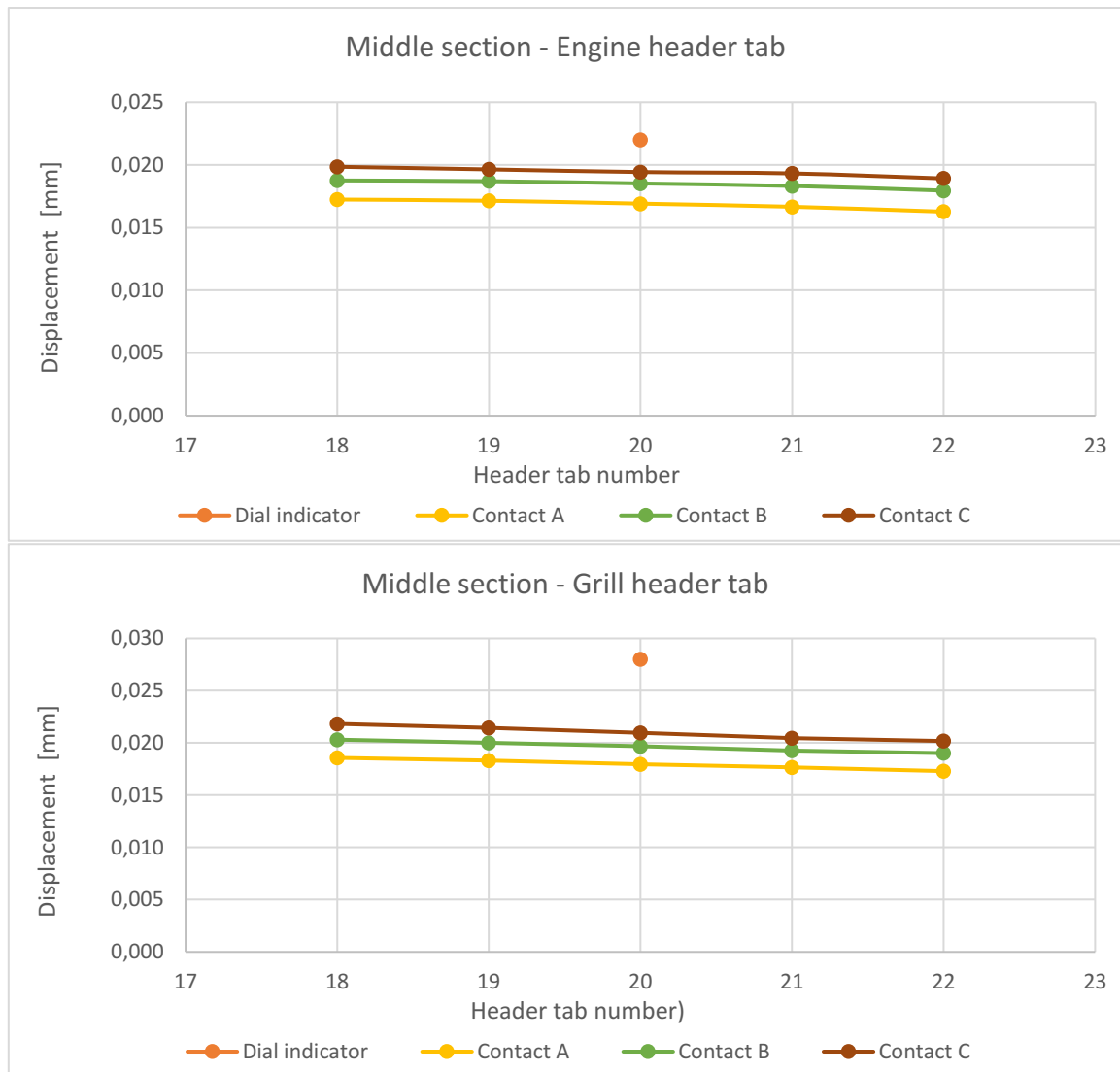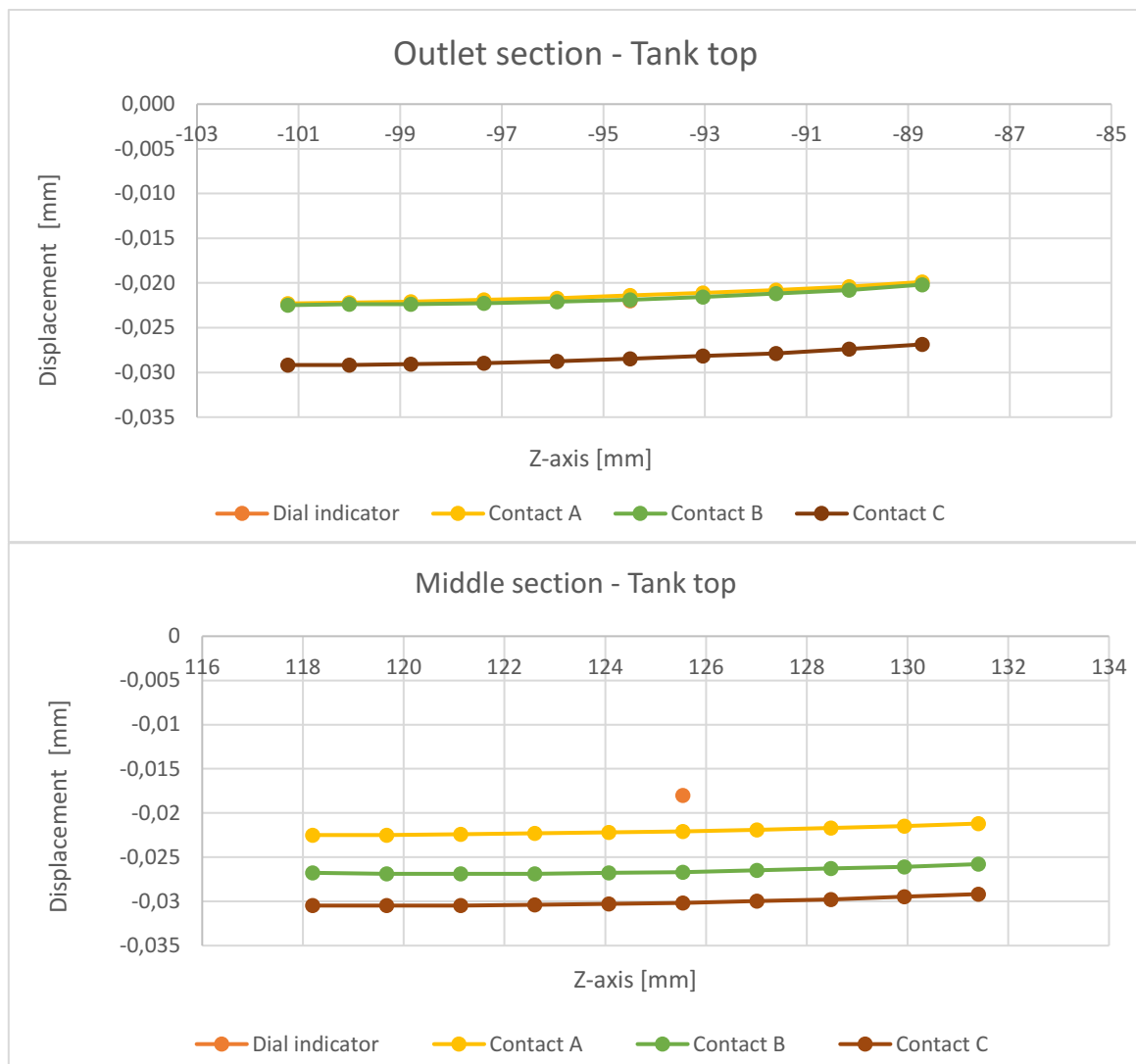Figure 8-41: Displacement of header tabs at outlet section.

Figure 8-42: Displacement of header tabs at the middle section.

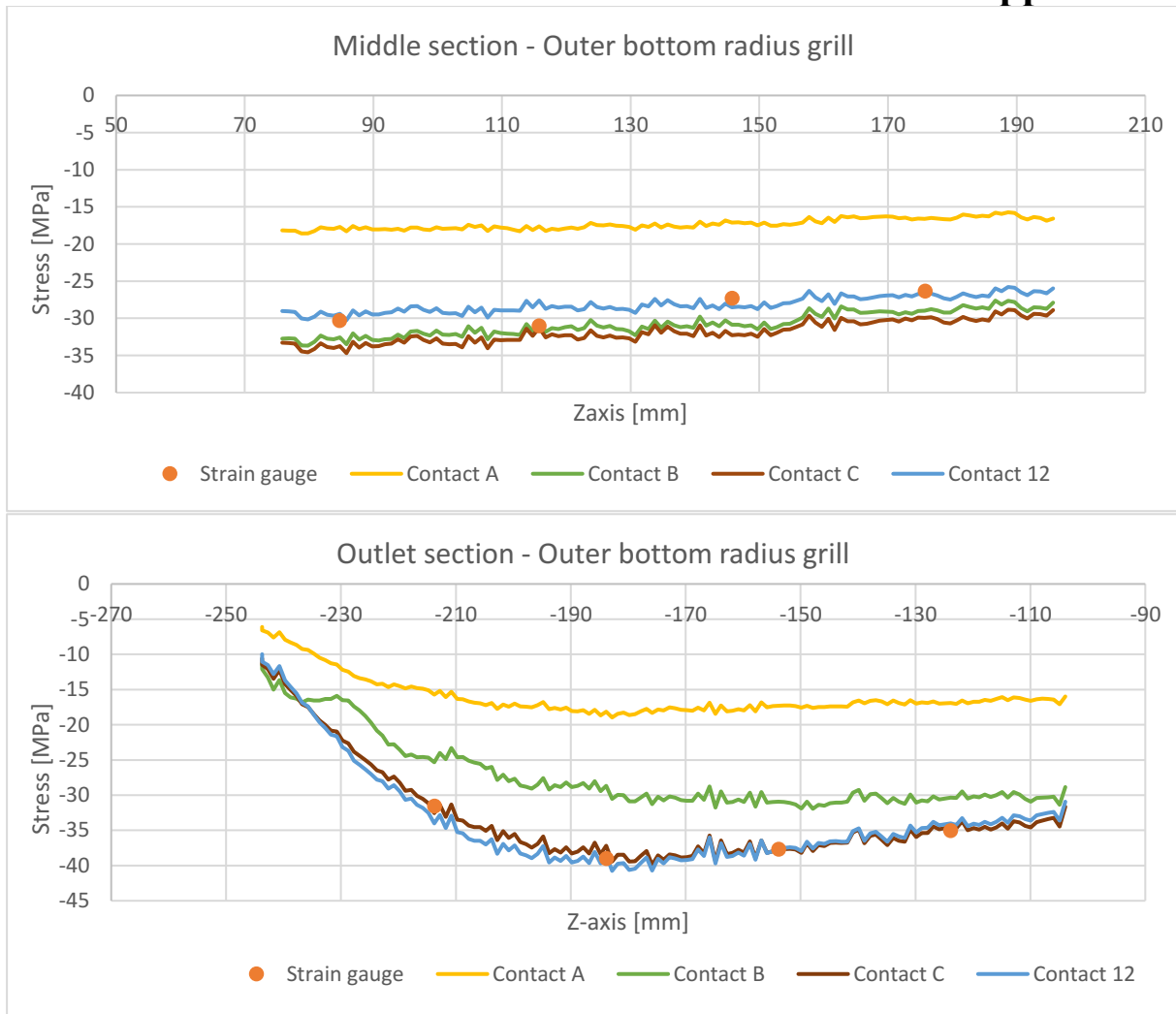Figure 8-43: Displacement at the tank top.

Figure 8-44: Correlation of stresses located at the outer bottom radius at the grill side.
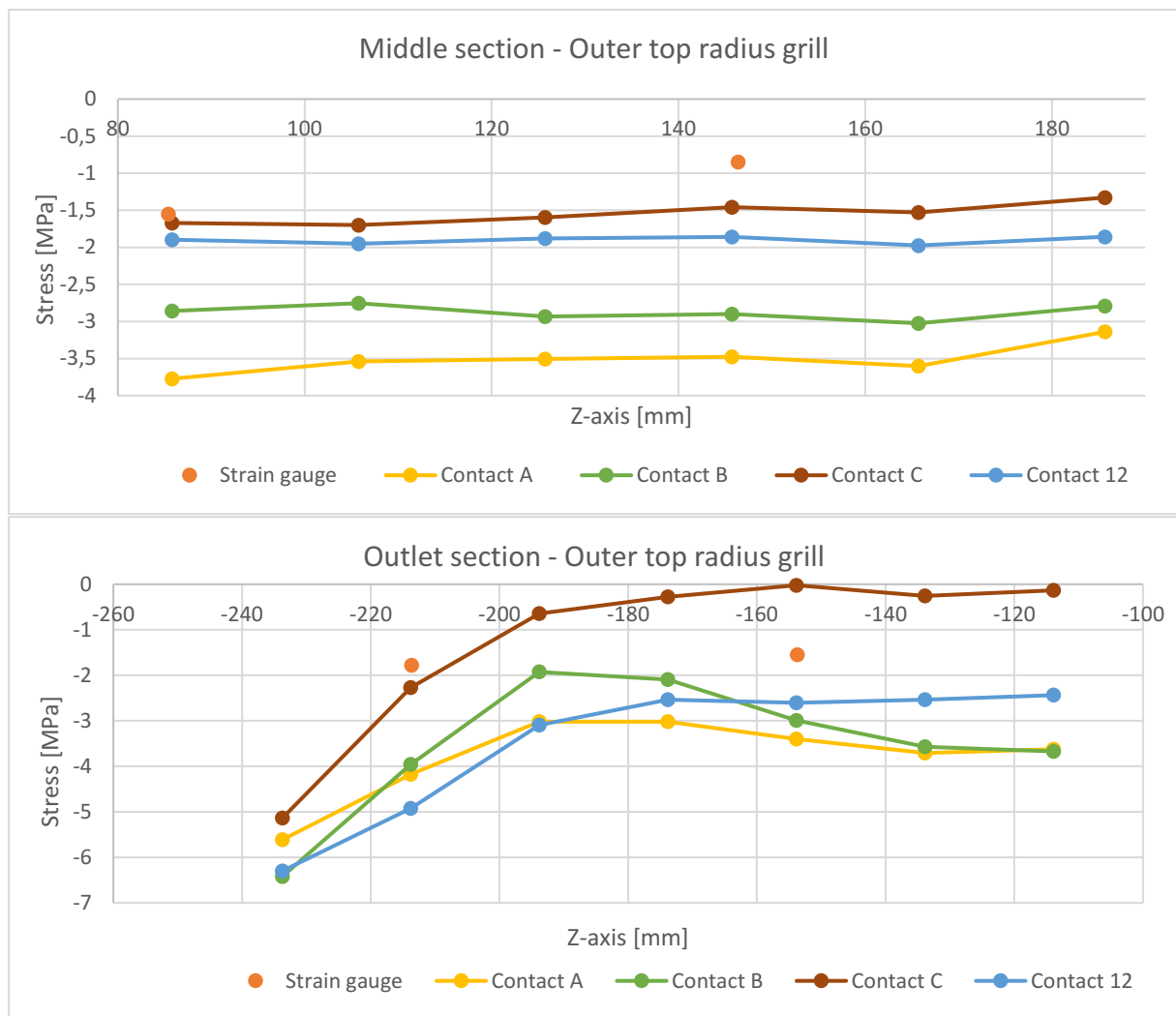
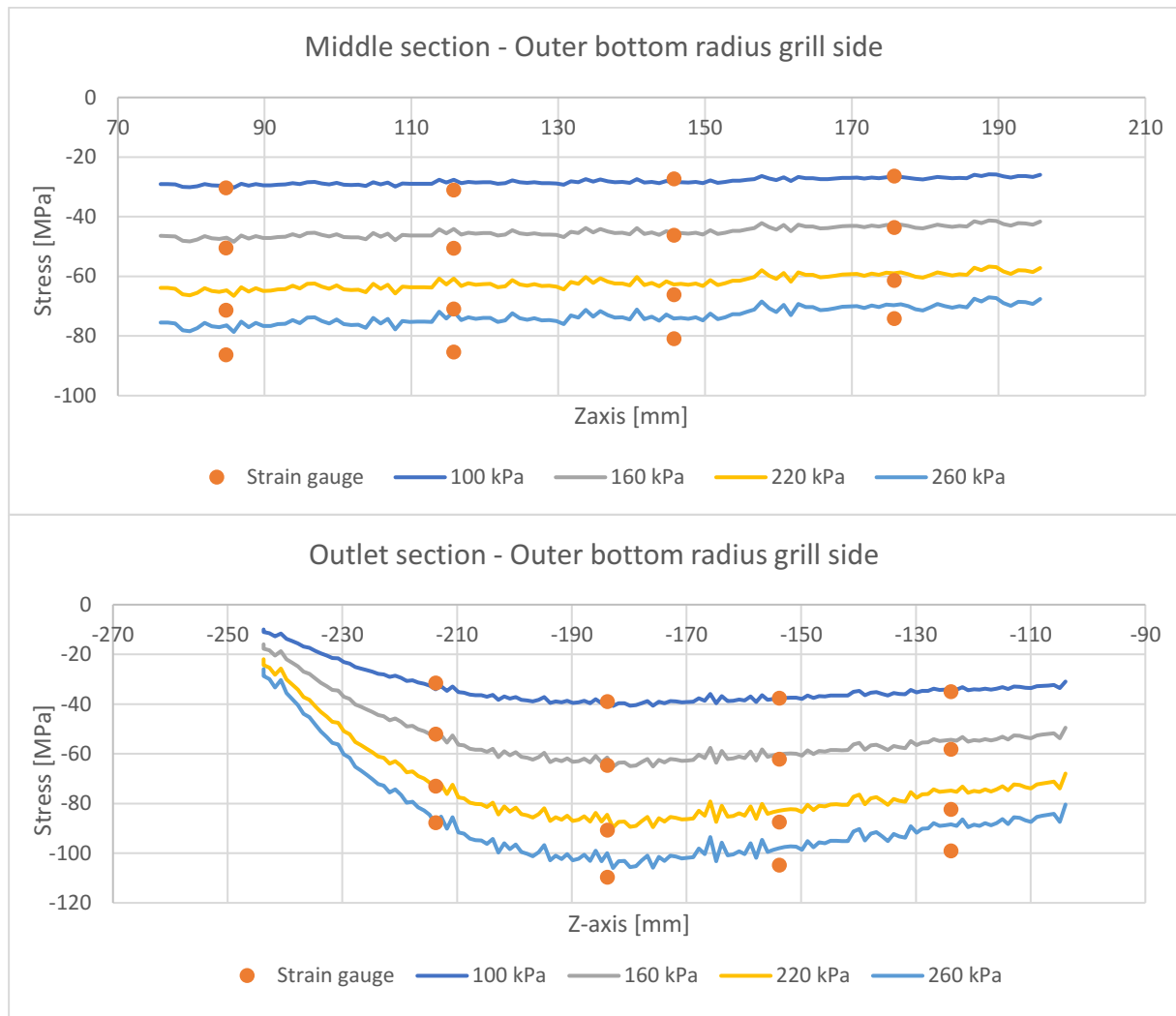Figure 8-45: Correlation of stresses located at the outer top radius on the grill side.

Figure 8-46: Correlation of stresses located at the outer bottom radius on the grill side at increased pressure.
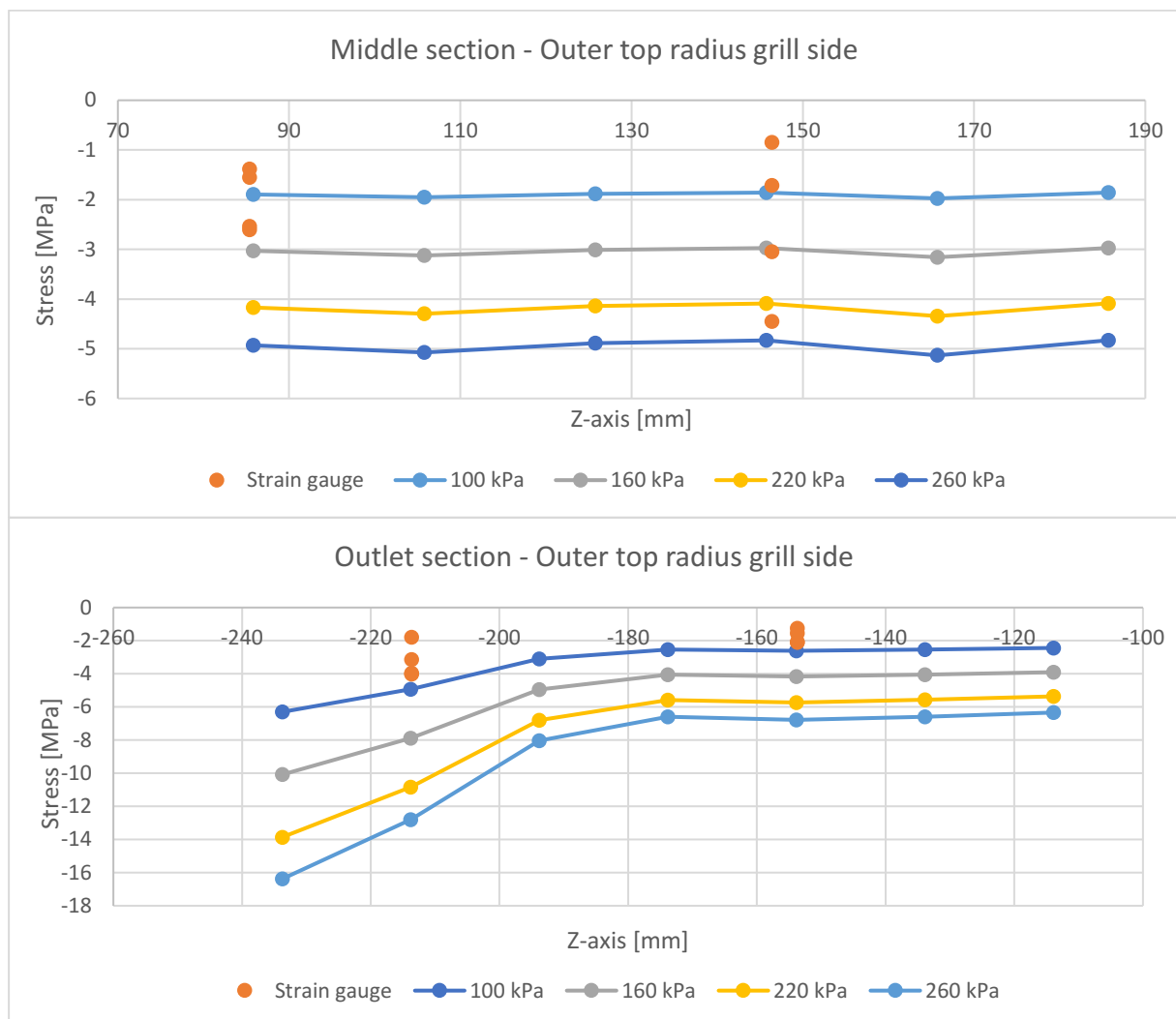
Figure 8-47: Correlation of stresses located at the outer top radius on the grill side.